Search for Scalar Top Quark Pair-production by R-parity Violating Decay Mode in $p\bar{p}$ Collisions at $\sqrt{s} = 1.8$ TeV

Yoshiyuki Miyazaki

Abstract

We search for the scalar top quark pair production ($\tilde{t}_1\bar{\tilde{t}}_1$) in which $\tilde{t}_1$ decays via the R-parity violating ($\not{R}_p$) process, using integrated luminosity 106 pb^{-1} data collected by the CDF detector during 1992–1995 in $p\overline{p}$ collisions at $\sqrt{s} = 1.8$ TeV. The R-parity is a quantum number which distinguishes between the Standard Model particles and the supersymmetric particles. We assume the R-parity is violated in the third generation so that $\tilde{t}_1$ decays into τ lepton and b-quark with the branching ratio (B) via λ'_{333} or ϵ_3 couplings. The final state search topology is for two τ's, an electron from $\tau \rightarrow e\nu_e\nu_\tau$, a decaying hadronically, and two or more jets. The final number of events after the selection is found to be zero, and the number of backgrounds expected from the Standard Model processes is 1.92 $\pm$ 0.11 (stat) $\pm$ 0.15 (sys). We have obtained a lower limit on the $\tilde{t}_1$ mass to be 111 GeV/c^2 at 95 % confidence level for $B = 1$ and also a upper limit of the branching ratio by using with next-to-leading order theoretical cross section.

Acknowledgments

I would like to thank my adviser Prof. Toru Okusawa for his guild line. I would like to thank Prof. Teruki Kamon for his help through my analysis at Fermilab. Furthermore, I would like to be grateful to Dr. Min Jeong Kim, Dr. Masashi Tanaka, Dr. Maxwell Chertok, Dr. James P. Done, Dr. Yukihiro Kato, Dr. Yoshihiro Seiya and Dr. Kazuhiro Yamamoto for supporting my analysis. I thank Dr. Stephan Lammel, Dr. Steve Worm, SUSY group and Exotic group for providing several comments and advises.

I would like also to be thankful to stuff members of the CDF Japan group and the CDF students for two years in Chicago life. I would like to thank the all members for the high energy laboratory in Osaka City University, especially, Associate Prof. Takuo Yoshida, Dr. Takeshi Takano and Dr. Horotoshi Toyoda.

I would like to thank Mrs. Carol Picciolo, Mrs. Kyoko Kunori and Mrs. Kazuko Kumashiro for helping to stay at Fermilab.

I would like to thank the Fermilab staff and the technical staffs of the participating institutions for their vital contributions, too. This work was supported by the Ministry of Education, Science, Sports and Culture of Japan; the U.S. Department of Energy and National Science Foundation; the Italian Istituto Nazionale di Fisica Nucleare; the Natural Sciences and Engineering Research Council of Canada; the National Science Council of the Republic of China; the Swiss National Science Foundation; the A. P. Sloan Foundation; the Bundesministerium fuer Bildung und Forschung, Germany; the Korea Science and Engineering Foundation (KoSEF), the Korea Research Foundation; and the Comision Interministerial de Ciencia y Tecnologia, Spain.

Contents

1 Introduction **1**

1.1 The Standard Model 1

1.2 Supersymmetry 5

1.2.1 The Problems of the Standard Model 5

1.2.2 Lagrangian of Supersymmetry 6

1.2.3 R-parity and the Minimal Supersymmetric Standard Model . . . 12

1.3 The Scalar Top Quarks 17

1.3.1 The Scalar Top Quark Mass 17

1.3.2 The Scalar Top Quark Pair Production 18

1.3.3 The Scalar Top Quark Decay 18

1.4 Physics Motivation 21

2 Experimental Apparatus **24**

2.1 The Tevatron 24

2.2 The Overview of the CDF Detector 26

2.2.1 The Tracking System 29

2.2.2 The Calorimeter System 31

2.2.3 The Muon System 34

2.3 The Data Taking 35

3 Data Process and Analysis **38**

3.1 How to Determine the Cross Section for the Stop Pair Production 38

3.2 Signal Selection 40
3.2.1 Used Dataset Sample 40
3.2.2 Central Electron Selection 40
3.2.3 $Z^0 \to ee$ Removal 43
3.2.4 Electron Isolation 44
3.2.5 Central τ_h Selection 45
3.2.6 Results After e and τ_h Selection 48
3.3 Study of the Constituents in the Signal Sample 48
3.3.1 Monte Carlo Samples 48
3.3.2 QCD Background 50
3.3.3 Comparison with the Signal Sample 52
3.4 Signal Event Section 55
3.4.1 $Z^0 \to \tau\tau$ Event Selection 55
3.4.2 $\tilde{t}_1\bar{\tilde{t}}_1$ Event Selection 63

4 Systematic Uncertainties **76**
4.1 Canceled and Reduced Terms of Systematic Uncertainties 77
4.1.1 Canceled Term of Systematic Uncertainties 77
4.1.2 Systematic uncertainty of Trigger Efficiency 77
4.2 Systematic Uncertainties for $Z^0(\to \tau\tau)$ Events 77
4.2.1 $Z^0(\to \tau\tau)$ Events Candidates Statistics 77
4.2.2 Cross Section of $Z^0(\to \tau\tau)+ \geq n$ Jets Events 77
4.2.3 Parton Distribution 78
4.2.4 Statistical Uncertainty in the MC Samples 78
4.3 Systematic Uncertainties for $\tilde{t}_1\bar{\tilde{t}}_1$ Events 78
4.3.1 Gluon Radiation 79
4.3.2 Q^2 Dependence 79
4.3.3 Jet Energy Scale 79
4.4 Summary of Systematic Uncertainties 79

5 Results and Disscusion **83**

5.1 Calculation of the Limit 83

5.2 The Limit for Cross Section for Stop Pair Production 85

5.3 Discussion 85

6 Conclusion **91**

6.1 Conclusion 91

List of Figures

1.1 The theoretical next-to-leading order cross section for $p\bar{p} \to \tilde{t}_1\bar{\tilde{t}}_1$ at $\sqrt{s} =$ 1.8 TeV with CTEQ4M using PROSPINO 19

1.2 The Feynman diagrams for scalar top quark R-parity λ'_{333} (left) and ϵ_3 (right) coupling violating decay 21

1.3 The Feynman diagrams for scalar top quark pair-production by R-parity λ'_{333} coupling violating decay 23

2.1 The schematic view of the Tevatron. 25

2.2 The schematic view of one quadrant of the CDF detector during RUN I, 1992 - 1996. 28

2.3 The schematic view of the one barrel of Silicon Vertex Detector. 30

2.4 The schematic view of the VTX. 30

2.5 The $x - y$ view of the Central Tracking Chamber. 32

2.6 the segmentation of the CDF calorimeters in the $\eta - \phi$ plane. 33

2.7 The segmentation of the central CDF muon chambers in the $\eta - \phi$ plane. 36

3.1 Distributions of $E_T(e)$, $p_T(\tau_h)$, $\Delta\phi(e, \tau_h)$, $\Delta\phi(e, \not\!\!E_T)$, $\not\!\!E_T$ and $M(e, \tau_h)$ for data and expectation of opposite-sign events after our e and τ_h selection. 54

3.2 Distributions of $M_T(e, \not\!\!E_T)$ (top) and significance (bottom) 57

3.3 Distributions of $p_T(e, \not\!\!E_T)$ (top) and significance (bottom) 58

3.4 Distributions of $E_T(e)$, $p_T(\tau_h)$, $\Delta\phi(e, \tau_h)$, $\Delta\phi(e, \not\!\!E_T)$, $\not\!\!E_T$ and $M(e, \tau_h)$ for data and expectation of opposite-sign events after $Z^0 \to \tau\tau$ with 0-jet selection cuts. 60

3.5 Number of charged tracks in τ cone after $Z^0 \to \tau\tau + 0$ jet selection . . . 62
3.6 Distributions of $M_T(e, \not\!\!E_T)$ (top), and significance (bottom) 64
3.7 Distributions of $H_T(e, \not\!\!E_T)$ (top) and significance (bottom) 65
3.8 Distributions of $E_T(e)$, $p_T(\tau_h)$, $\Delta\phi(e, \tau_h)$, $\Delta\phi(e, \not\!\!E_T)$, $\not\!\!E_T$ and $M(e, \tau_h)$, for data and expectation of opposite-sign events after $\tilde{t}_1\bar{\tilde{t}}_1$ selection cuts before jet requirement. 66
3.9 Distributions of the number of jets (top) and significance (bottom) . . . 67
3.10 The cut efficiency for $\tilde{t}_1\bar{\tilde{t}}_1 \to \tau^+ b\tau\overline{b} \to (\ell\nu\nu b)(\tau_h\nu\overline{b})$ 69
3.11 Inclusive jet distribution in $e + \tau_h$ event after $\tilde{t}_1\bar{\tilde{t}}_1$ selection cuts before jet requirement. 73
3.12 The data selection criteria for the opposite-sign $e\tau_h+ \geq 2$ jets sample . . 74

5.1 95% confidence level on upper limit for cross section for $\tilde{t}_1\bar{\tilde{t}}_1 \to \tau^+ b\tau^-\overline{b}$ along with the theoretical calculation 89
5.2 95% confidence level on upper limit for cross section for $\tilde{t}_1\bar{\tilde{t}}_1 \to \tau^+ b\tau^-\overline{b}$ along with the theoretical calculation in the case of the observed events number = 0, 1, 2 90

List of Tables

1.1 The particle spectrum of the fermion in the Standard Model 2
1.2 The list of boson in the Standard Model 3
1.3 The chiral (top) of the first generation and gauge (down) superfields of the MSSM 14

3.1 Electron trigger dataset for electron+τ_h sample 41
3.2 Electron identification quality cuts 41
3.3 Cuts for $Z^0 \to ee$ removal. 44
3.4 τ_h identification quality cuts 49
3.5 Sources to $e + \tau_h$ events 51
3.6 Summary of Monte Carlo samples 51
3.7 Summary of yields of $e + \tau_h$ pairs in the data and MC events after our e and τ_h selection. The uncertainty is only statistical. 53
3.8 Number of events in data and MC samples after each cut 61
3.9 Summary of yields of $e+\tau_h$ pairs in the data and MC events after $Z^0 \to \tau\tau$ with 0-jet selection cut. 61
3.10 Event selection efficiencies and trigger efficiencies (%) for $\tilde{t}_1\bar{\tilde{t}}_1 \to \tau^+ b\tau^- \overline{b} \to e\tau_h b\overline{b} + X$ events from 70 to 130 GeV/c^2 with each cuts. 71
3.11 Number of events in data and MC samples after each cut 72
3.12 Summary of yields of $e + \tau_h$ pairs in the data and MC events after $\tilde{t}_1\bar{\tilde{t}}_1$ selection cut. 72
3.13 A breakdown of the backgrounds and data as a function of event reduction requirement 75

4.1 Systematic uncertainties for trigger efficiency from 70 to 130 GeV/c^2 . . . 81
4.2 Systematic uncertainties from $Z^0 \to \tau\tau$ events. 81
4.3 Systematic uncertainties for the $\tilde{t}_1\bar{\tilde{t}}_1 \to b\tau^+\overline{b}\tau^- \to e\tau_h b\overline{b} + X$ events from 70 to 130 GeV/c^2 82
4.4 Total systematic uncertainties for from 70 to 130 GeV/c^2 82

5.1 Table of the cross section upper limit for $\tilde{t}_1\bar{\tilde{t}}_1 \to b\tau^+\overline{b}\tau^- \to e\tau_h b\overline{b} + X$ events from 70 to 130 GeV/c^2 87
5.2 Summary of upper limits of the branching ratio $B^{95\%CL}(\tilde{t}_1 \to \tau^+ b)$ for $\tilde{t}_1\bar{\tilde{t}}_1 \to b\tau^+\overline{b}\tau^- \to e\tau_h b\overline{b} + X$ events from 70 to 130 GeV/c^2 87
5.3 Summary of the cross section upper limit for $\tilde{t}_1\bar{\tilde{t}}_1 \to b\tau^+\overline{b}\tau^- \to e\tau_h b\overline{b} + X$ events from 70 to 130 GeV/c^2 in the case of the observed events number = 0, 1, 2 88

Chapter 1

Introduction

This thesis is described as a search for an evidence of new physics in elementary particles. Currently, an existing theory called the Standard Model (SM) could explain various experiments results. However, the SM has several problems which cannot be solved without an introduction of a new physics concept. The supersymmetry (SUSY) is one of the candidates for the new physics concept which introduces a symmetry between fermions and bosons.

In this chapter, an overview of the Standard Model and an introduction to the supersymmetry theory including the physics respect with this analysis will be described.

1.1 The Standard Model

The Standard Model (SM) of the particle physics has survived through many precise tests. The SM consists of two theories of the Quantum Chromodynamics (QCD) and the Glashow-Salam-Weinberg model [1] for the electroweak interaction. Each theory is based on a symmetry group $SU(3)_c$ and $SU(2)_L \times U(1)_Y$, respectively. Interactions are required to be invariant under the local gauge translations described by the group generator. The $SU(3)$ describes the strong interactions, and the $SU(2)_L \times U(1)_Y$ symmetry does the weak and electromagnetic interactions.

The SM particles are composed of the fermions and the bosons. The fermions are

Table 1.1: The particle spectrum of the fermion in the Standard Model

Quarks						
	1st	2nd	3rd	Q	T_3	Y
$\hat{Q}$	$\begin{pmatrix} u \\ d \end{pmatrix}_L$	$\begin{pmatrix} c \\ s \end{pmatrix}_L$	$\begin{pmatrix} t \\ b \end{pmatrix}_L$	$2/3$ $-1/3$	$1/2$ $-1/2$	$1/3$ $1/3$
$\hat{U}$	u_R	c_R	t_R	$2/3$	0	$4/3$
$\hat{D}$	d_R	s_R	b_R	-1/3	0	$-2/3$

Leptons						
	1st	2nd	3rd	Q	T_3	Y
$\hat{L}$	$\begin{pmatrix} \nu_e \\ e \end{pmatrix}_L$	$\begin{pmatrix} \nu_\mu \\ \mu \end{pmatrix}_L$	$\begin{pmatrix} \nu_\tau \\ \tau \end{pmatrix}_L$	0 -1	$1/2$ $-1/2$	-1 -1
$\hat{E}$	e_R	μ_R	τ_R	-1	0	-2

half integer spin particles which are elements for the ordinary matters. They are described by the Dirac spinor fields, ψ. The fermions are classified into three generations according to their masses and consist of the quarks and the leptons. Table 1.1 shows the particle spectrum of the fermion in the SM. Each left-handed (ψ_L) and right-handed (ψ_R) fermion are described by $\frac{1}{2}(1-\gamma_5)\psi$ and $\frac{1}{2}(1+\gamma_5)\psi$, respectively. The $\hat{Q}$ and $\hat{L}$ indicate doublets of the quark and the lepton fields are coupled by the weak interactions, respectively. The $\hat{U}$, $\hat{D}$ and $\hat{E}$ indicate right-handed quark fields of up- and down-type, and right-handed lepton, respectively. Each fermion has a anti-partner which has a opposite sign quantum number of it. The weak isospin T_3 of $SU(2)$ and the weak hyper charge Y of $U(1)_Y$ have a relation with the electric charge Q,and the relation is $Q = T_3 + Y/2$.

The fundamental bosons are the integer spin particles which mediate the strong, weak and electromagnetic interactions. Table 1.2 shows the list of bosons in the SM.

The Lagrangian for the electroweak sector in the SM consists of four terms and is

Table 1.2: The list of boson in the Standard Model

Boson	Interaction
gamma (γ)	Electromagnetic
$W^{\pm}$	Weak
Z^0	Weak
gluon (g)	Strong

written as:

$$\mathcal{L} = \mathcal{L}_{\text{gauge}} + \mathcal{L}_{\text{fermion}} + \mathcal{L}_{\text{scalar}} + \mathcal{L}_{\text{Yukawa}} \tag{1.1}$$

The first term of Eq. (1.1), the $\mathcal{L}_{\text{gauge}}$ has the parts of kinematic energy and self-interaction for $W^{\pm}$, Z^0 and γ. This term is composed by two terms

$$\mathcal{L}_{\text{gauge}} = -\frac{1}{4}\boldsymbol{W}_{\mu\nu} \cdot \boldsymbol{W}^{\mu\nu} - \frac{1}{4}B_{\mu\nu}B^{\mu\nu}. \tag{1.2}$$

where $W_{\mu\nu} \equiv \partial_\mu W_\nu - \partial_\nu W_\mu - g W_\mu \times W_\nu$ is the field strength for the $SU(2)_L$ gauge boson W_μ, and $B_{\mu\nu} = \partial_\mu B_\nu - \partial_\nu B_\mu$ is the field strength for the $U(1)$ gauge boson B_μ. The second term of Eq. (1.1), the $\mathcal{L}_{\text{fermion}}$ is expressed the kinematic energies for fermions and the interactions between gauge bosons ($W^{\pm}$, Z^0 and γ) and fermions. $\mathcal{L}_{\text{fermion}}$ is given by

$$\mathcal{L}_{\text{fermion}} = \bar{\psi}_L \left(i\partial_\mu - g\frac{1}{2}\boldsymbol{\tau} \cdot \boldsymbol{W}_\mu - g^{'}\frac{Y}{2}B_\mu \right) \psi_L + \bar{\psi}_R \left(i\partial_\mu - g^{'}\frac{Y}{2}B_\mu \right) \psi_R. \tag{1.3}$$

The τ is the Pauli matrices (representations of $SU(2)$) and Y is the hypercharge. The g and $g^{'}$ are the $SU(2)_L$ and $U(1)$ gauge coupling constant, respectively.

The third term of Eq. (1.1), the $\mathcal{L}_{\text{scalar}}$ shows a mass term for Higgs boson and coupling term between electroweak gauge boson ($W^{\pm}, Z^0$ and γ) and Higgs.

$$\mathcal{L}_{\text{scalar}} = \frac{1}{2}\left| \left(i\partial_\mu - g\frac{1}{2}\boldsymbol{\tau} \cdot \boldsymbol{W}_\mu - g^{'}\frac{Y}{2}B_\mu \right) \phi \right|^2 - V(\phi). \tag{1.4}$$

where the $V(\phi)$ is the Higgs scalar potential and is described as:

$$V(\phi) = \frac{1}{2}\mu^2\phi^2 + \frac{1}{4}\lambda\phi^4. \tag{1.5}$$

where the ϕ is a single $SU(2)_L$ doublet of the Higgs boson. We consider only the case of $\mu^2 < 0$ and $\lambda > 0$. The last term of Eq. (1.1), the $\mathcal{L}_{\text{Yukawa}}$ shows the mass term for fermion and the coupling term between the fermion and Higgs, and is described as follows:

$$\mathcal{L}_{\text{Yukawa}} = -\left(G_1 \bar{\psi}_L \phi \psi_R + G_2 \bar{\psi}_R \phi \psi_L + h.c.\right). \tag{1.6}$$

where G_1 and G_2 are Yukawa coupling constants which is proportional to fermion's mass.

When the neutral components of the Higgs boson get the vacuum expectation value v, the $SU(2)_L \times U(1)_Y$ gauge symmetry is broken and the $W^{\pm}$ and Z^0 obtain their masses. In a mass eigenstate basis, the charged W-bosons receive masses

$$M_W = \frac{1}{\sqrt{2}} g v. \tag{1.7}$$

The fields of neutral gauge bosons are defined as

$$Z_\mu = \frac{g W_\mu^3 - g' B_\mu}{\sqrt{g^2 + g'^2}}. \tag{1.8}$$

$$A_\mu = \frac{g W_\mu^3 + g' B_\mu}{\sqrt{g^2 + g'^2}}. \tag{1.9}$$

with masses

$$M_Z = \frac{1}{\sqrt{2}} \sqrt{g^2 + g'^2}\, v = M_W / \cos\theta_W. \tag{1.10}$$

$$m_\gamma = 0. \tag{1.11}$$

where the weak mixing angle θ_W is defined as

$$\sin\theta_W = g' / \sqrt{g^2 + g'^2}. \tag{1.12}$$

Fermion masses are

$$m_f = G_f v. \tag{1.13}$$

The Standard Model for Glashow-Salam-Weinberg theory agrees with experimental measurements.

1.2 Supersymmetry

1.2.1 The Problems of the Standard Model

Shown in Section 1.1, there is a direct relationship between particle masses and the Higgs mass expectation value, $v \sim M_W \sim O(100)$ GeV. However the Planck scale $M_P \sim O(10^{19})$ GeV is much greater than M_W. The ratio M_P/M_W is a powerful clue to the character of physics beyond the SM, because of the famous "hierarchy problem". This mass hierarchy problem stems from the fact that Higgs mass are not stable under the radiative correction[2]. The hierarchy problem are written as below.

If the Higgs fields couples to fermions with the mass m_f on the Lagrangian of the Yukawa coupling $-\lambda_f \phi \bar{\psi} \psi$ with the coupling constant λ_f, the contribution of one-loop correction to the Higgs mass (δm_H) is written as follows:

$$\delta m_H^2 = \frac{|\lambda_f|^2}{16\pi^2}[-2\Lambda^2 + 6m_f \ln(\Lambda^2/m_f) + \cdots] \tag{1.14}$$

where Λ is an ultraviolet cutoff value, where we expect a new physics to play an important role. The problem is that if Λ is of order of the Planck scale, this correction is some 30 orders of the magnitude larger than the Higgs mass. This is only one direct problem for the corrections to the Higgs mass, because the quantum corrections to fermions and gauge bosons do not have the quadratic sensitivity to the Λ. However, the leptons, quarks and the electroweak gauge boson of the SM all owe their masses to the Higgs mechanism, so the entire mass spectrum of the SM is directly or indirectly sensitive to the cutoff value Λ.

In contrast, the scalar masses affect to the Higgs mass from quadratically divergent. The contributions of one-loop correction by the scalar field S with the mass m_S coupling to the Higgs boson with the Lagrangian $-\lambda_S \phi^2 S^2$ are computed

$$\delta m_H^2 = \frac{\lambda_S}{16\pi^2}[\Lambda^2 - 2m_S \ln(\Lambda^2/m_S) + \cdots] \tag{1.15}$$

If we rejects a physical interpretation of λ_S and uses dimensional regularization on the loop integral instead of a momentum cutoff, Λ^2 term could be canceled. However, even so the term proportional to the m_S cannot be eliminated without the physically unjustifiable

tuning of a correction term. So the m_H is sensitive to the masses of the heaviest particles. If the m_S is very large, its effects in the SM do not decouple, but instead make it very difficult to understand why m_H is so small.

Total contribution of one-loop correction is sum over Eqs. (1.14) and (1.15). Total systematic cancellation of this dangerous contributions to δm_H^2 can only be brought about the conspiracy which is better known to physicists as a symmetry. It is apparent from comparing Eqs.(1.14) and (1.15) that the new symmetry ought to relate between fermions and bosons, because of the relative minus sign between fermion loop and boson loop contributions to δm_H^2. If each of the quarks and leptons of the SM is accompanied by two complex scalars with $\lambda_S = |\lambda_f|^2$, then the Λ^2 term will neatly cancel. Such a symmetry is called as a supersymmetry (SUSY) [3], which is a symmetry between fermions and bosons, offers just framework for including the necessary new particles and the absence of these dangerous radiative correction.

If in addition, the bosons and fermions all have the same masses, then radiative corrections vanish identically. The stability of the hierarchy only requires that the weak scale is preserved so that we need only to require that

$$|m_S^2 - m_f^2| \leq 1 \text{ TeV}^2 \tag{1.16}$$

1.2.2 Lagrangian of Supersymmetry

The SUSY introduces the supersymmetric particles, each of which is a superpartner of the SM particles. The spin of supersymmetric particles is half integer different from that of the SM particles. The particles are combined into the supermultiplets, which contains fields differing a half unit of spin each other. The next step is to discuss the Lagrangian for the supersymmtery [4].

Interaction of Chiral Supermultiplets

At first, we start to discuss the Lagrangian for a single chiral supermultiplet. The chiral supermultiplet contains a complex scalar ϕ_i and a left-handed Weyl fermion ψ_i as physical degree of freedom, plus a complex auxiliary field F_i which does not propagates physically.

The Lagrangian for a free kinetic energies is written as follows,

$$\mathcal{L}_{chiral(KE)} = -(\partial_\mu \phi^{*i})(\partial^\mu \phi_i) - i\psi^{\dagger i}\bar{\sigma_\mu}\partial^\mu \psi_i + F^* F. \tag{1.17}$$

where we sum over repeated indices i with the convention that field ϕ_i and ψ_i always carry lowered indices, while their conjugates always carry upper indices. The σ_i is the Pauli matrix. It is invariant under the supersymmtery translation defined below;

$$\delta\phi_i = \xi\psi_i. \qquad \delta\phi^{*i} = \xi^\dagger \psi^{\dagger i}. \tag{1.18}$$

$$\delta(\psi_i)_\alpha = i(\sigma^\mu \xi^\dagger)_\alpha \partial_\mu \phi_i + \xi_\alpha F_i. \qquad \delta(\psi^{\dagger i})_{\dot{\alpha}} = -i(\xi\sigma^\mu)_{\dot{\alpha}} \partial_\mu \phi^{*i} + \xi^\dagger_{\dot{\alpha}} F^{*i}. \tag{1.19}$$

$$\delta F_i = i\xi^\dagger \bar{\sigma}^\mu \partial_\mu \psi_i. \qquad \delta F^{*i} = -i\partial_\mu \psi^{\dagger i}\bar{\sigma}^\mu \xi. \tag{1.20}$$

where ξ is an infinitesimal anticommutator of two-component Weyl fermion objects which are parameterized by the supersymmetry transformation.

The next task is to include interactions in the chiral supermultiplets which are also consistent with the supersymmetry. We will therefore consider a set of chiral supermultiplets (ϕ_i, ψ_i, F_i) and renormalizable Lagrangian $\mathcal{L}_{chiral(int)}$. Renormalizability limits the mass dimensions of any terms in the Lagrangian to be less than or equal to 4. Since the interaction Lagrangian must be invariant under supersymmetry translations, we do not expect any terms which cubic or quartic in the scalar field ϕ_i. Clearly no term can be linear in the fermion fields either. This leaves us with only the following possibilities;

$$\mathcal{L}_{chiral(int)} = -\frac{1}{2}W^{ij}\psi_i\psi_j + W^i F_i + h.c.. \tag{1.21}$$

where W^{ij} and W^i are functions of scalar fields with dimension of [mass] and [mass]^2, respectively. Here, and in all that follows, it will be assumed that repeated indices such as ii are summed. Furthermore, since $\psi_i\psi_j = \psi_j\psi_i$, the function W^{ij} must be symmetric ij. The function W^{ij} and W^i will be related by insisting on the invariance of Eq. (1.21). We begin with the variation of $\mathcal{L}_{chiral(int)}$,

$$\begin{aligned}
\delta\mathcal{L}_{chiral(int),} \;=\; & \frac{1}{2}\frac{\partial W^{ij}}{\partial \phi_k}(\xi\psi_k)(\psi_i\psi_j) + \frac{1}{2}\frac{\partial W^{ij}}{\partial \phi^{k*}}(\xi^\dagger\psi^{k\dagger})(\psi_i\psi_j) \\
& + \frac{1}{2}W^{ij}(\xi F_i + i\sigma^\mu \xi^\dagger \partial\phi_i)\psi_j \\
& + \frac{1}{2}W^{ij}\psi_i(\xi F_j + i\sigma^\mu \xi^\dagger \partial\phi_j)
\end{aligned}$$

$$+\frac{\partial W^i}{\partial \phi_j}(\xi\psi_j)F_i + \frac{\partial W^i}{\partial \phi^{j*}}(\xi^\dagger\psi^{j\dagger})F_i$$
$$+W^i i\xi^\dagger\bar{\sigma}^\mu\partial_\mu\psi_i + h.c.. \tag{1.22}$$

From supersymmetric translations and Fierz identity $(\xi\psi_k)(\psi_i\psi_j)+(\xi\psi_i)(\psi_j\psi_k)+(\xi\psi_j)(\psi_k\psi_i)=0$, the W^{ij} is expected to be analytic (or holomorphic) function in the complex field ϕ_k since the derivative of the W^{ij} with respect to ϕ_k must be symmetric in ijk. Therefore given these constraints, we can write

$$W^{ij} = -M^{ij} - y^{ijk}\phi_k \tag{1.23}$$

where M^{ij} as a symmetric fermion mass matrix, and y^{ijk} as a set of symmetric Yukawa couplings. In fact, it will be convenient to write,

$$W^{ij} = -\frac{\partial^2 W}{\partial\phi_i\partial\phi_j}. \tag{1.24}$$

where

$$W = \frac{1}{2}M^{ij}\phi_i\phi_j + \frac{1}{6}y^{ijk}\phi_i\phi_j\phi_k. \tag{1.25}$$

and is called as *Superpotential*.

Noting that 2nd and 3rd lines of Eq.(1.22) are equal due to the symmetry of W^{ij}, we can rewrite the remaining terms as,

$$\begin{aligned}\delta\mathcal{L}_{chiral(int)} &= W^{ij}(\xi F_i + i\sigma^\mu\xi^\dagger\partial\phi_i)\psi_j \\ &\quad +\frac{\partial W^i}{\partial\phi_j}(\xi\psi_j)F_i + \frac{\partial W^i}{\partial\phi^{j*}}(\xi^\dagger\psi^{j\dagger})F_i \\ &\quad -W^i i\partial_\mu\psi_i\sigma^\mu\xi^\dagger + h.c..\end{aligned} \tag{1.26}$$

in addition using spinor identities on the last term. Furthermore, noting that because of definition of the superpotential in the term of W^{ij}, we can write $W^{ij}\partial_\mu\phi_j = -\partial_\mu(\partial W/\partial\phi_i)$. Then the 2nd and last term of Eq.(1.26) can be combined as a total derivative if

$$W^i = \frac{\partial W}{\partial\phi_i}. \tag{1.27}$$

and thus is also related to the superpotential W. The 4th term of Eq.(1.26) is proportional to $\partial W^i/\partial\phi^{j*}$ so that this term is absent and the definition of W^i allows for trivial

cancellation of the 1st and 3rd term in Eq. (1.26). Thus interaction Lagrangian for chiral multiplets is supersymmetric with the imposed relationships between the function, W^{ij}, W^i and the superpotential W.

Finally, the auxiliary field F_i and F^{i*} can be eliminated using their classical equation of motion. The variation of the Lagrangian with respect to F is

$$\frac{\delta\mathcal{L}}{\delta F_i} = F^{i*} + W^i. \tag{1.28}$$

$$\frac{\delta\mathcal{L}}{\delta F^{i*}} = F_i + W_i^*. \tag{1.29}$$

Namely,

$$F_i = -W_i^*. \tag{1.30}$$

$$F^{i*} = -W^i. \tag{1.31}$$

Putting everything together, we can get the Lagrangian for the chiral supermultiplets as follows,

$$\mathcal{L}_{chiral} = -(\partial_\mu\phi^{*i})(\partial^\mu\phi_i) - i\psi^{\dagger i}\bar{\sigma}_\mu\partial^\mu\psi_i - \frac{1}{2}(W^{ij}\psi_i\psi_j + W^*_{ij}\psi^{i\dagger}\psi^{j\dagger}) - W^iW_i^* \tag{1.32}$$

As one can see, the last term plays the role of scalar potential as follows,

$$V(\phi_i, \phi^{i*}) = W^iW_i^*. \tag{1.33}$$

Interaction of Gauge Supermultiplets

.

Next, we discuss the Lagrangian for the vector (or gauge) supermultiplets. The fields in the gauge supermultiplets are massless gauge boson fields A^a_μ, and two-component Weyl fermion gauginos λ^a. The index a here runs over the adjoint representation of the gauge group. The gauge transformations of the gauge supermultiplet fields are written as follows,

$$\delta_{gauge}A^a_\mu = -\partial_\mu\Lambda^a + gf^{abc}A^b_\mu\Lambda^c. \tag{1.34}$$

$$\delta_{gauge}\lambda^a = gf^{abc}\lambda^b\Lambda^c. \tag{1.35}$$

where the Λ^a is an infinitesimal gauge transformation parameter, the g is the gauge coupling constant and the f^{abc} are the totally antisymmetric structure constants which define the gauge group.

The on-shell degrees of freedom for A^a_μ and λ^a_α amount to two bosonic and two fermionic helicity states (for each a), as required by the supersymmetry. However, off-shell λ^a_α consists of four real, fermionic degrees of freedom, while A^a_μ only has three real bosonic degrees of freedom; one is removed by the homogeneous gauge transformation in Eq. (1.34). So, we need one real bosonic auxiliary field D^a like the chiral auxiliary field F_i. This field also transforms as an adjoint of the gauge field and satisfies $(D^a)^* = D^a$.

Therefore, the Lagrangian density for a gauge field supermultiplet is written as

$$\mathcal{L}_{gauge(KE)} = -\frac{1}{4}F^a_{\mu\nu}F^{\mu\nu a} - i\lambda^{a\dagger}\bar{\sigma_\mu}D^\mu\lambda^a + \frac{1}{2}D^aD^a \tag{1.36}$$

where

$$F^a_{\mu\nu} = \partial_\mu A^a_\nu - \partial_\nu A^a_\mu - gf^{abc}A^b_\mu A^c_\nu \tag{1.37}$$

and D^μ is the $SU(3) \times SU(2) \times U(1)$ gauge invariant derivative.

From the analogy of the chiral supermultiplets, the gauge supermultiplets under the supersymmetry translation are written as follows;

$$\delta A^a_\alpha = -\frac{1}{\sqrt{2}}[\xi^\dagger\bar{\sigma}_\mu\lambda^a + \lambda^{a\dagger}\bar{\sigma}_\mu\xi] \tag{1.38}$$

$$\delta\lambda^a_\alpha = \frac{i}{2\sqrt{2}}(\sigma^\mu\bar{\sigma}^\nu\xi)_\alpha + \frac{1}{\sqrt{2}}\xi_\alpha D^a \tag{1.39}$$

$$\delta D^a = \frac{i}{\sqrt{2}}[\xi^\dagger\bar{\sigma}^\mu D_\mu\lambda^a - D_\mu\lambda^{a\dagger}\bar{\sigma}^\mu\xi] \tag{1.40}$$

If we have both chiral and gauge supermultiplets in the theory, we must make simple modifications to the supersymmetry transformations discussed in the previous section and add new gauge invariant interactions between the chiral and gauge supermultiplets which also respect the supersymmetry. For this purpose, we only replace from ∂_μ to D_μ. By changing it, the supersymmetry transformations for chiral supermultiplets to include gauge-covariant are changed from Eqs.(1.18) (1.19) and (1.20) to

$$\delta\phi_i = \xi\psi_i \tag{1.41}$$

$$\delta(\psi_i)_\alpha = i(\sigma^\mu \xi^\dagger)_\alpha D_\mu \phi_i + \xi_\alpha F_i \tag{1.42}$$

$$\delta F_i = i\xi^\dagger \bar{\sigma}^\mu D_\mu \psi_i + \sqrt{2} g (T^a \phi)_i \xi^\dagger \lambda^{\dagger a} \tag{1.43}$$

where T^a is the relevant representation of the gauge group. The new interaction terms take the form:

$$\mathcal{L}_{newint} = -\sqrt{2} g[(\phi^* T^a \psi)\lambda^a + \lambda^{\dagger a}(\psi^\dagger T^a \phi)] + g(\phi^* T^a \phi) D^a \tag{1.44}$$

Furthermore, invariance under the supersymmetry requires the condition

$$W^i (T^a)_i^j \phi_j = 0 \tag{1.45}$$

Finally, we must eliminate the auxiliary field D^a using the equation of motion which yields

$$D^a = -g(\phi^* T^a \phi) \tag{1.46}$$

Like the auxiliary fields $F^i(F^{*i})$, the D^a are expressible purely algebraically in the term of the scalar fields. The full scalar potential is

$$\begin{aligned} V(\phi, \phi^*) &= |F_i|^2 + \frac{1}{2}\sum_a |D^a|^2 \\ &= |\frac{\partial W}{\partial \phi_i}|^2 + \frac{1}{2}\sum_a g^2 (\phi^* T^a \phi)^2 \end{aligned} \tag{1.47}$$

The two terms in Eq. (1.47) are called "F-term" and "D-term" contributions, respectively. Since the $V(\phi, \phi^*)$ is a sum of square, it is always greater than or equal zero for every field configuration. It is very interesting and a unique feature of supersymmetric theories that the scalar potential is completely determined by the other interaction in the theory. The F-terms are fixed by Yukawa couplings and the fermion mass terms, and the D-terms are fixed by the gauge interactions.

Soft supersymmetric breaking interaction

If supersymmetry were unbroken, the supersymmetric particles would have the same masses as their SM partners. Since we don't observe them, supersymmetry must be broken. However, the mechanism of supersymmetry breaking is not well understood. At

this point we have constructed a SUSY theory containing all of the SM but the supersymmetry remains to be broken and the particles of their SUSY partner are massless. This is clearly unacceptable. In order to preserve the hierarchy between the electroweak and GUT or Planck scales, it is necessary that explicit breaking of supersymmetry be done softly, i.e. by insertion of weak scale mass terms in the Lagrangian. This ensures that the theory remains to be free from quadratic divergence. In context of the general renormalizable theory, the possible soft mass terms are written as follows,

$$\begin{aligned}\mathcal{L}_{soft} &= -\frac{1}{2}M_\lambda^a\lambda^a\lambda^a - (m^2)_j^i\phi_i\phi^{j*} \\ &\quad -\frac{1}{2}B^{ij}\phi_i\phi_j - \frac{1}{2}A^{ijk}\phi_i\phi_j\phi_k \end{aligned} \tag{1.48}$$

where the M_λ^a are gaugino masses, $(m^2)_j^i$ are soft scaler masses, B^{ij} is a bilinear mass term, and A^{ijk} is a trilinear mass term.

1.2.3 R-parity and the Minimal Supersymmetric Standard Model

The Minimal Supersymmetric Extension of the Standard Model

Most of the works in the SUSY searches are being performed within the Minimal Supersymmetric extension of the Standard Model (MSSM) [5]. The MSSM is defined as the minimal field contents which account for the SM fields and the minimal superpotential necessary to account for the known Yukawa mass terms. Table 1.3 shows the chiral and gauge supermultiplets of the MSSM. There are quark and lepton supermultiplets for all three generations while we listed in Tables 1.3 only the members of the first generation. The supermultiplet $\hat{Q}$ consists of an $SU(2)_L$ doublet of quarks and their scalar partners which are also in an $SU(2)_L$ doublet. Similarly, the $\hat{U}^c$ ($\hat{D}^c$) contains the right-handed up (down) quarks and its scalar partners. The scalar partners of quarks are called as squarks. The leptons are contained in the $SU(2)_L$ doublet supermultiplet $\hat{L}$ which includes the left-handed fermion and their scalar partners. Finally, the right-handed electrons contained in the supermultiplets $\hat{E}^c$ and a scalar partner. The scalar partners of leptons are called as sleptons.

The $SU(3) \times SU(2) \times U(1)$ gauge fields obtain Majorana fermion partners in a

SUSY model. The $\hat{G}^a$ supermultiplets contain the gluon, g^a, and their fermion partners the gluinos, $\tilde{g}^a$. The $\hat{W}^i$ contains the $SU(2)_L$ gauge bosons, W_i, and their fermion partners, $\tilde{w}_i$ (wino). Finally, $\hat{B}$ contains the $U(1)$ gauge field B and its fermion partner, $\tilde{b}$ (bino).

The SM contains a single Higgs doublet including a scalar particle. In the SUSY, the Higgs doublet requires a SUSY partner which is Majorana fermion fields, $\tilde{h}$ called the Higgsinos. The Higgsino contributes to the $SU(2)$ and $U(1)$ gauge anomalies. While the fermions from the SM are exactly canceled anomalies with right-handed quantum numbers, the term of the Higgsino remains uncanceled. Therefore, the SUSY adds the second Higgs doublet which have an opposite $U(1)$ quantum number from the first doublet. The second Higgs doublet has fermionic partners and the contributions of the fermions from the two Higgs doublets to gauge anomalies will cancel each others. The two Higgs doublets are also required in order to give both the up and down quarks mass in the SUSY theory. The requirement of at least two Higgs doublets is a feature of all models with weak scale supersymmetry.

As such we define the MSSM by the superpotential W_{MSSM} is given by

$$W_{MSSM} = \varepsilon_{ij}\mu\hat{H}_u^i\hat{H}_d^j + \epsilon_{ij}\left[y_L\hat{H}_u^i\hat{L}^j\hat{E}^c + y_D\hat{H}_u^i\hat{Q}^j\hat{D}^c + y_U\hat{H}_d^i\hat{Q}^j\hat{U}^c\right], \tag{1.49}$$

where i and j are the SU(2) indices. The $\mu\hat{H}_u^i\hat{H}_d^j$ term in the superpotential gives mass terms for Higgs boson by applying $|W^i|^2$. The μ is the Higgs mass parameter and the sign of μ is sensitive to the physics. The y_L, y_D and y_U give the usual Yukawa interactions of fermions with Higgs bosons from the term $W^{ij}\psi_i\psi_j$ (and $W^*_{ij}\psi^{i\dagger}\psi^{j\dagger}$). The all y could be matrices which mix the interaction of the three generations. Hence these coefficients are determined in the fermion masses. The vacuum expectation value of the neutral members of the scalar components of Higgs doublets are not free parameters at all.

$R-$parity

In defining the supersymmetric standard model, in particular, the MSSM, we have limited the model to contain a minimal fields content. That is, the only new fields are those which are required by supersymmetry. However, we have a minimal choice regarding

Table 1.3: The chiral (top) of the first generation and gauge (down) superfields of the MSSM

chiral superfield				
Supermultiplets	$SU(3)$	$SU(2)_L$	$U(1)$	Particle contents
$\hat{Q}$	3	2	1/6	(u_L, d_L), $(\tilde{u}_L, \tilde{d}_L)$
$\hat{U}^c$	$\bar{3}$	1	2/3	$\bar{u}_R, \tilde{u}_R^*$
$\hat{D}^c$	$\bar{3}$	1	$-1/3$	$\bar{d}_R, \tilde{d}_R^*$
$\hat{L}$	1	2	$-1/2$	(ν_L, e_L), $(\tilde{\nu}_L, \tilde{e}_L)$
$\hat{E}^c$	1	1	1	$\bar{e}_R, \tilde{e}_R^*$
$\hat{H}_u$	1	2	1/2	$(H_u, \tilde{h}_u)$
$\hat{H}_d$	1	2	$-1/2$	$(H_d, \tilde{h}_d)$

gauge superfield				
Supermultiplets	$SU(3)$	$SU(2)_L$	$U(1)$	Particle contents
$\hat{G}^a$	8	1	0	g, $\tilde{g}$
$\hat{W}^i$	1	3	0	W_i, $\tilde{w}_i$
$\hat{B}$	1	1	0	B, $\tilde{b}$

the interactions in the superpotential. We have limited the types of the interactions to include only those required in the SM and SUSY generation. However, even if we stick to the minimal fields content, there are several other superpotential terms which are consistent with all of the gauge symmetries and the renormalization of the theory. Such a superpotential is written as follows,

$$W_{\Delta L=1} = \varepsilon_{ij}\left[\lambda_{ijk}\hat{L}_i\hat{L}_j\hat{E}^c_k + \lambda^{'}_{ijk}\hat{L}_i\hat{Q}_j\hat{D}^c_k+\right] + \varepsilon_i\epsilon_i\hat{L}_i\hat{H}_u. \tag{1.50}$$

$$W_{\Delta B=1} = \lambda^{''}_{ijk}\hat{U}^c_i\hat{D}^c_j\hat{D}^c_k \tag{1.51}$$

Here, λ_{ijk}, $\lambda^{'}_{ijk}$ and $\lambda^{''}_{ijk}$ are Yukawa coupling constants. The ε_i is a dimensionful mass parameter. The $ijk = 1, 2, 3$ are generation indices. The Eq. (1.50) is produced to be the lepton number violation, while Eq. (1.51) is produced to be the baryon number violation. For the convenience, we introduce a new quantum number called as R-parity (R_p). The R_p is defined as

$$R_p = (-1)^{3B+L+2S}, \tag{1.52}$$

where B is the baryon number, L is the lepton number, and S refers to the spin of the particle. R_p distinguishes SM particles ($R_p = 1$) form SUSY particles ($R_p = -1$). Eq. (1.50) and (1.51) are called as R-parity violation ($\not{R}_p$) terms. If the R-parity is conserved in the MSSM, supersymmetric particles are always produced in pairs and decay into the SM particles and the lightest supersymmetric particles (LSP). This process involves large missing energy as its signature because of the existing of the LSP. However, the R-parity conservation is not ensured by the gauge invariance and there is no reason to forbid the R-parity violation.

Eq. (1.50) and (1.51) can be separated into two-types of R-parity violating terms. First two terms in Eq. (1.50) and one term in Eq. (1.51) are the explicit R-parity violation resulting from the trilinear $\not{R}_p$ (TRPV) couplings. Last term in Eq. (1.50) is the spontaneous R-parity violation resulting from the bilinear $\not{R}_p$ (BRPV) couplings.

In the TRPV framework, the lepton number violation is induced in the λ_{ijk} and $\lambda^{'}_{ijk}$ terms, while the baryon number violation is induced in the $\lambda^{''}_{ijk}$ terms [6]. The λ_{ijk} is antisymmetric under the interchange of the first two indices, while $\lambda^{''}_{ijk}$ is antisymmetric

under the interchange of the last two. Thus, there are 27 free parameters for $\lambda^{'}$ and 9 for λ_{ijk} and $\lambda^{''}$. Namely, the TRPV involves 45 free parameters in total.

On the other hand, the ϵ_i is the coupling of the lepton number violation in the i-th generation. The R-parity in the BRPV framework is spontaneously broken through the vacuum expectation values (VEV) of the right-handed sneutrino $< \tilde{\nu} >= v_R \neq 0$ [7]. The ϵ_3 parameter induces a non-zero VEV of the left-handed tau neutrinos $< \tilde{\nu} >= v_3/\sqrt{2}$. The v_3 contributes to the W mass according to $m_W^2 = \frac{1}{4}g^2(v_u^2 + v_d^2 + v_3^2)$, where v_u and v_d are the VEV's of the Higgs doublets. In introducing the BRPV, charginos mix with charged leptons, neutralinos mix with neutrinos, and charged sleptons mix with charged Higgs bosons.

1.3 The Scalar Top Quarks

In this Section, we will describe an overview of the scalar top quark properties concerning to mass, production and decay mode which we are interested in.

1.3.1 The Scalar Top Quark Mass

In sfermion mass matrix, there are three types of contributions from F- and D-terms in the scalar potential and soft mass SUSY breaking.

The F-term contribution gives rise to diagonal gauge eigenstate $\tilde{t}_L$ and $\tilde{t}_R$ mass from $(\partial W/\partial \tilde{t}_L)^2$ and $(\partial W/\partial \tilde{t}_R)^2$, respectively. These contributions are equal to the square of the top quark mass, m_t^2. The F-term also gives an off-diagonal contribution from $\partial W/\partial H_d$ which is proportional to $y_t v\mu = m_t \mu \cos\beta$, where $\tan\beta = v_u/v_d$ is the ratio of vacuum expectation value from the two Higgs doublets. The D-term only gives rise to the diagonal mass terms, but these differ from $\tilde{t}_L$ and $\tilde{t}_R$ since these fields are transformed differently under $SU(2) \times U(1)_Y$. Finally, the soft mass SUSY breaking terms give contributions to the diagonal $\tilde{t}_L$ and $\tilde{t}_R$ mass terms ($m^2_{\tilde{t}_L}$ and $m^2_{\tilde{t}_R}$), as well as an off-diagonal contribution $A_t m_t$. Therefore the mass matrix for $\tilde{t}_L$ and $\tilde{t}_R$ is given by

$$M^2_{\tilde{t}} = \begin{pmatrix} m^2_{\tilde{t}_L} + m_t^2 + M_Z^2(\frac{1}{2} - \frac{2}{3}\sin\theta_W)\cos 2\beta & m_t(A_t + \mu\cot\beta) \\ m_t(A_t + \mu\cot\beta) & m^2_{\tilde{t}_R} + m_t^2 + \frac{2}{3}M_Z^2 \sin\theta_W \cos 2\beta \end{pmatrix} \tag{1.53}$$

Note that the off-diagonal entries are proportional to the mass of the top quark. Eq. (1.53) also describes the scharm ($\tilde{c}$) and sup ($\tilde{u}$) matrices, with the obvious replacement $t \to c$ or u. Since the mass of the u and c is much less than that of $\tilde{c}$ and $\tilde{u}$, the $(\tilde{c}_L - \tilde{c}_R)$ and $(\tilde{u}_L - \tilde{u}_R)$ mixing are usually negligible. However, since the top mass is comparable to the other masses that appear in Eq. (1.53), the $(\tilde{t}_L - \tilde{t}_R)$ mixing is generally important. Eq. (1.53) can be diagonalized to give mass eigenstate as follows;

$$\begin{pmatrix} \tilde{t}_2 \\ \tilde{t}_1 \end{pmatrix} = \begin{pmatrix} \cos\theta_{\tilde{t}} & \sin\theta_{\tilde{t}} \\ -\sin\theta_{\tilde{t}} & \cos\theta_{\tilde{t}} \end{pmatrix} \begin{pmatrix} \tilde{t}_L \\ \tilde{t}_R \end{pmatrix} \tag{1.54}$$

with $m_{\tilde{t}_1} < m_{\tilde{t}_2}$ being the mass eigenvalues of Eq. (1.54) and $0 \le \theta_{\tilde{t}} \le \pi$. The off-diagonal entries for m_t^2 in Eq. (1.53) tend to mitigate that this effect typically induces a significant

mixing which reduces the square of the lightest scalar top eigenvalue. Therefore we focus on the lightest stop ($\tilde{t}_1$) since the stop could be the lightest squark of all.

1.3.2 The Scalar Top Quark Pair Production

Next, we discuss the pair production cross section of the lightest stop quark described in subsection 1.3.1. The pair production cross section of the lightest stop quark ($\tilde{t}_1$) is obtained by folding the partonic cross section with $q\bar{q}$ and gg luminosities. The dominant mechanism for the lightest stop quark production is the gg fusion at the Tevatron described in Section 2.1, later. Figure 1.1 shows the theoretical next-to-leading order (NLO) calculation for the scalar top pair production cross section ($p\bar{p} \to \tilde{t}_1\bar{\tilde{t}}_1$) at $\sqrt{s} = 1.8$ TeV. The QCD renormalization μ is applied as the stop mass, here. While the $\tilde{t}_1\bar{\tilde{t}}_1$ production cross section is affected by the other SUSY parameter such as gluino mass, the effect is only in high order correction. The $\tilde{t}_1\bar{\tilde{t}}_1$ production cross section is calculated using PROSPINO [9]. The pair production cross section is large enough to be detected using the Tevatron.

1.3.3 The Scalar Top Quark Decay

Having already shown that the lightest scalar top quark could be lighter than the top quark and that the pair production cross section is large enough in previous two subsections. Next, we discuss the $\tilde{t}_1$ decay in the both case of R-parity conservation and violation.

If the R-parity is conserved, the SUSY particles are always produced in pairs and decay through a cascade to SM particles and the the lightest supersymmetric particles, discussed in subsection 1.2.3 already. This implies that there is a lightest stable supersymmetric particles (LSP). The candidates for the LSP is $\tilde{\chi}_1^0$, where $\tilde{\chi}_1^0$ is the lightest neutralino mixed between the neutral fermionic partners of γ/Z^0 and neutral Higgs. If the lightest scalar top quark mass is less than the top quark's mass, the scalar top quark decays in R-parity conservation is either,

$$\tilde{t}_1 \to b\tilde{\chi}_1^+, \quad \text{if } m_{\tilde{t}_1} > m_b + m_{\tilde{\chi}_1^+},$$

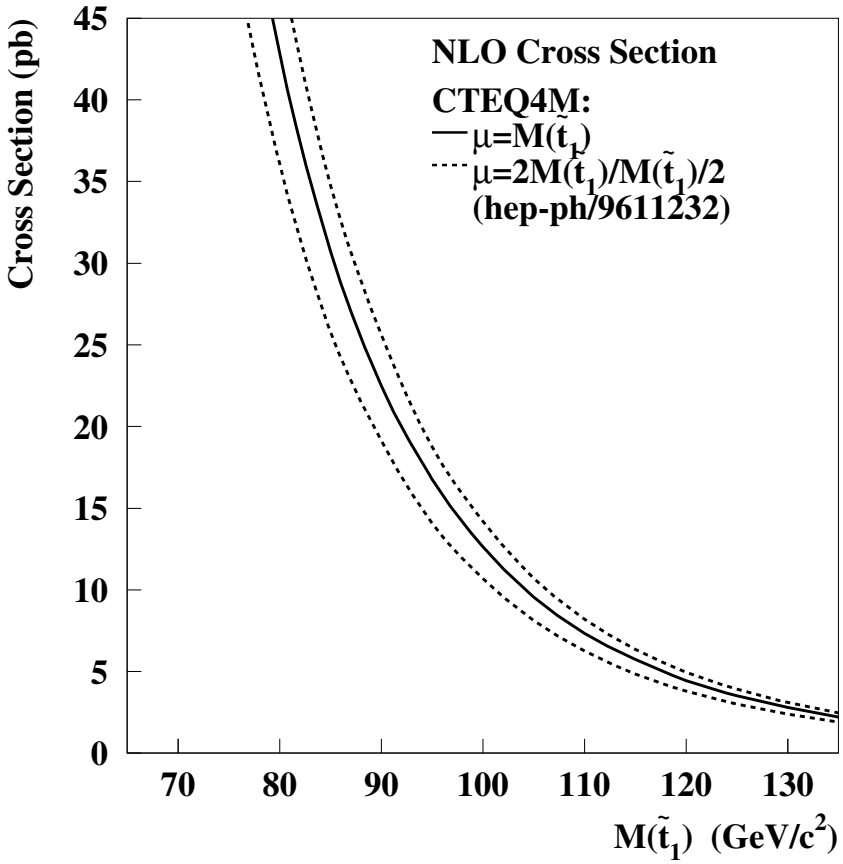

Figure 1.1: The theoretical next-to-leading order cross section for $p\bar{p} \to \tilde{t}_1\bar{\tilde{t}}_1$ at $\sqrt{s} = 1.8$ TeV with CTEQ4M using PROSPINO

or,

$$\tilde{t}_1 \to c\tilde{\chi}_1^0, \quad \text{if } m_{\tilde{t}_1} > m_c + m_{\tilde{\chi}_1^0}$$

The studies for these processes are shown in [10] for $\tilde{t}_1 \to b\tilde{\chi}_1^+$ and in [11] for $\tilde{t}_1 \to c\tilde{\chi}_1^0$, respectively.

Next, we discuss the case of R-parity violation which we are interested in. Of the four kinds of the Yukawa coupling terms for R-parity violation, the baryon violating λ'' are difficult to study at the Tevatron as they lead to events with multijets that would be overwhelmed by large backgrounds from QCD production of jets. Furthermore, the most obvious experimental constraint for the baryon violation comes from the non-observation of the proton decay. However, the lepton violating λ, λ' and ϵ give rise to multilepton and associated multijet final states, which would be excellent signatures at the Tevatron.

In the lepton violating terms, only λ' and ϵ survive in the stop decay. Furthermore we assume that the R-parity violation only happens in the third generation since we have large Yukawa coupling constants in the third generation in the SM. If the $\not{R}_p$ interactions involving the third generation is sizable for the case where either λ'_{333} or ϵ_3 is non-zero, the Lagrangian of interactions with R-parity violating terms is written as:

$$\begin{aligned}
\mathcal{L}_{RPV_{333}} &= \lambda'_{333}(\tilde{\tau}_L t_L b_R + \tilde{t}_L \tau_L b_R + \tilde{b}_R t_L \tau_L \\
&\quad + \tilde{\nu}_{\tau L} b_L b_R + \tilde{b}_L b_R \nu_L + \tilde{b}_R b_L \nu_L) \\
&\quad + \epsilon_3 \text{Ł}_3 \hat{H}_u. \qquad (1.55)
\end{aligned}$$

From Eq. (1.55), the stop can decay into a tau lepton and a bottom quark by violating the R-parity as follows:

$$\tilde{t}_1 \to \tau^+ + b.$$

Figure 1.2 shows the Feynman diagrams for the scalar top quark R-parity violating decay. The branching ratio of this channel is 100 % in both frameworks if the stop is the LSP. If the LSP is the $\tilde{\chi}_1^0$ with the next lightest supersymmetric particle (NLSP) being the stop, the stop can decay into $c\tilde{\chi}_1^0$ with the R-parity conservation. However, if R-parity breaking parameter λ'_{333} is large for TRPV or $|\epsilon_3|$ and $|v_3|$ are well below a GeV for BRPV, it is possible that the decay mode of the stop is dominant in the BRPV even when the LSP is $\tilde{\chi}_1^0$ [8].

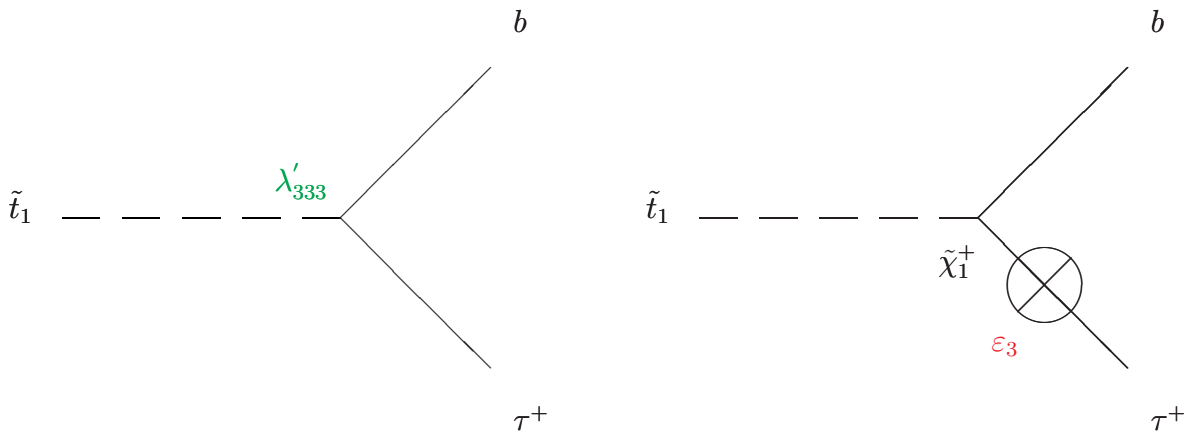

Figure 1.2: The Feynman diagrams for scalar top quark R-parity λ'_{333} (left) and ϵ_3 (right) coupling violating decay

In the case that the LSP is the lightest neutralino $\tilde{\chi}_1^0$, the LSP can decay into top quark, bottom quark and τ lepton ($\tilde{\chi}_1^0 \rightarrow b\bar{t}\tau^-$ (or $\bar{b}t\tau^+$)) or two bottom quarks and τ neutrino ($\tilde{\chi}_1^0 \rightarrow b\bar{b}\nu_\tau$ (or $b\bar{b}\bar{\nu}_\tau$)) by the TRPV parameter λ_{333}. However the decay process including top quark needs to be heavy mass which is greater than the sum of mass of the top quark, bottom quark and τ lepton ($\sim$ 180 GeV/c^2). This heavy LSP is difficult to detect at the Tevatron potentially since the production cross section is small. Even if the LSP mass in other decay process is lighter than the above decay, this process is difficult to study since the background is large from the QCD processes. Next, even if the LSP is changed into the τ neutrino by the BRPV parameter ϵ_3, we can't distinguish from the LPS and τ neutrino. From these reasons, the other process except the scalar top quark process are difficult to detect at the Tevatron.

1.4 Physics Motivation

The SUSY is an important role for new physics beyond the Standard Model. The scalar top quark could be potentially to detect at the Tevatron, and becomes a good candidate of the SUSY. The decay mode for $\tilde{t}_1 \rightarrow \tau^+ + b$ is a remarkable for the signature of the R-parity violation where the strength of the R-parity violating coupling term is

finite. In our case, as the R-parity violating coupling term is significantly smaller than the gauge coupling, the supersymmetric particles are produced in pairs. Even if the supersymmetric particles are produced by the R-parity violating coupling term, these processes are dominantly single production and it is difficult to detect them due to large background. Therefore, we search for an evidence of the direct production of stop pairs followed by $\tilde{t}_1$ decay into a tau lepton and a bottom quark. From two τ lepton and two b-quark from the stop quark pair production and R-parity violating decay, we consider the final topology of an electron (e) from $\tau \rightarrow e\nu_e\nu_\tau$, a hadronically decaying tau (τ_h) lepton and two or more jets. Figure 1.3 shows the Feynman diagrams for scalar top quark pair-production by R-parity violating decay in the case of λ'_{333} coupling, for examples.

The lower limit of the stop mass in this signature was reported to be 93 GeV/c^2 by the LEP experiment [12]. This result is based on λ'_{33k} in the TRPV. Nevertheless, we might expect to be able to obtain more stringent mass limit of stop. Conclusively, this analysis is very important for understanding or searching new physics beyond the Standard Model.

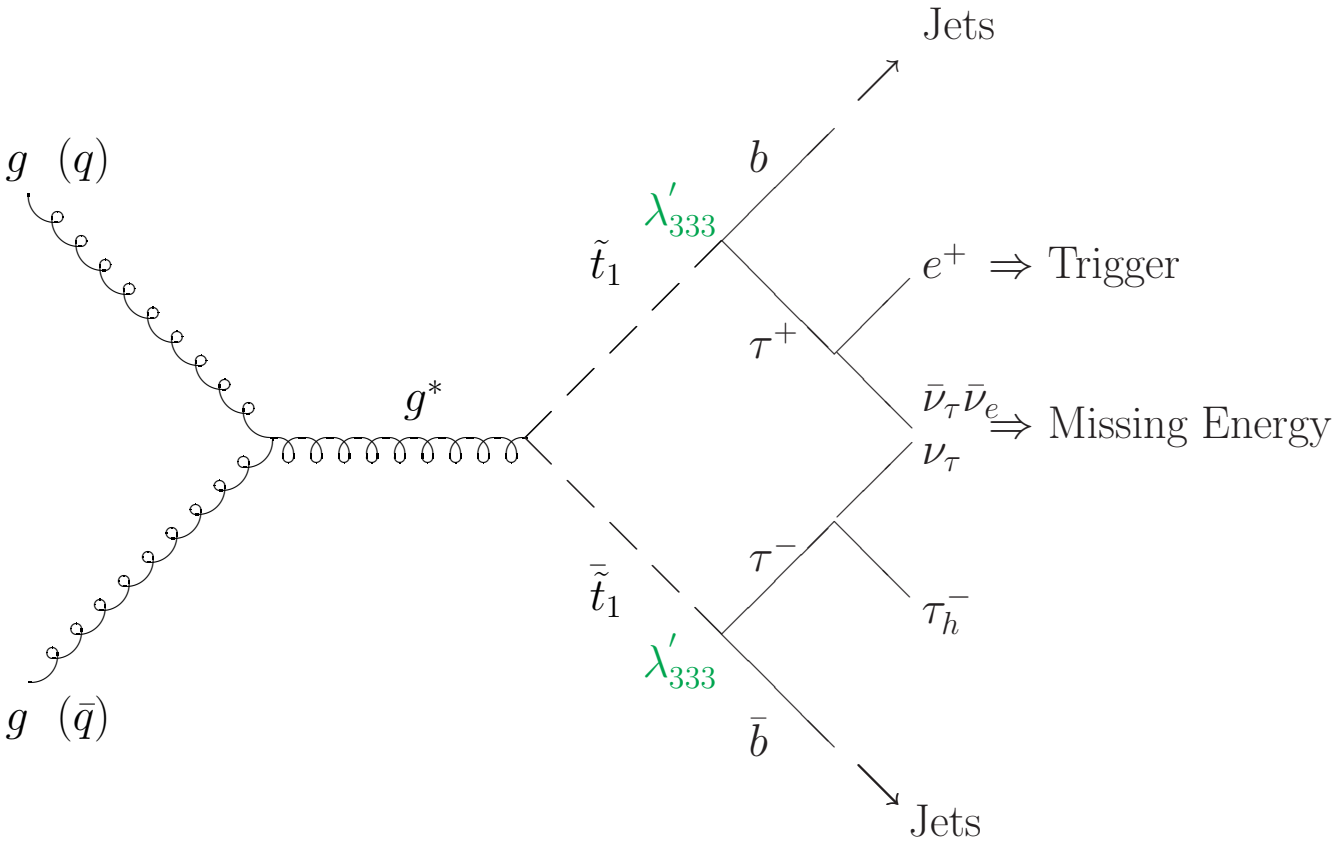

Figure 1.3: The Feynman diagrams for scalar top quark pair-production by R-parity λ'_{333} coupling violating decay

Chapter 2

Experimental Apparatus

This experiment was performed at the Fermi National Accelerator Laboratory (Fermilab). The data were collected with the Collider Detector at Fermilab (CDF) with the accelerator Tevatron, a superconducting proton-antiproton synchrotron and storage ring with a 1 km radius. In this chapter, the experimental apparatuses are described.

2.1 The Tevatron

The Tevatron is a superconducting accelerator which collides the proton (p) and the antiproton ($\bar{p}$) beams at a center of mass energy of 1.8 TeV. Figure 2.1 shows the schematic view of the accelerator. There are five stages for the acceleration process in the Tevatron.

The proton beam is created in the preaccelerator called Clockoff-Walton accelerator. Here an electron is added into each hydrogen atom (H_2) to create a negative ion (H^{-1}). Next, the negative ions are accelerated to an energy of 750 keV and passed to the Linac.

The Linac is a 150 meters long Alvarez drift-tube accelerator, where the negative ions are accelerated to 200 MeV. Following this acceleration, the negative ions drift 46 meters down to a transport line to a radio frequency debuncher, which minimizes the momentum spread of ions, before they are injected into the Booster.

The Booster is a 77.5 meters radius fast-cycling synchrotron. In the Booster, the negative ions pass through a carbon foil designed to remove the electrons from the

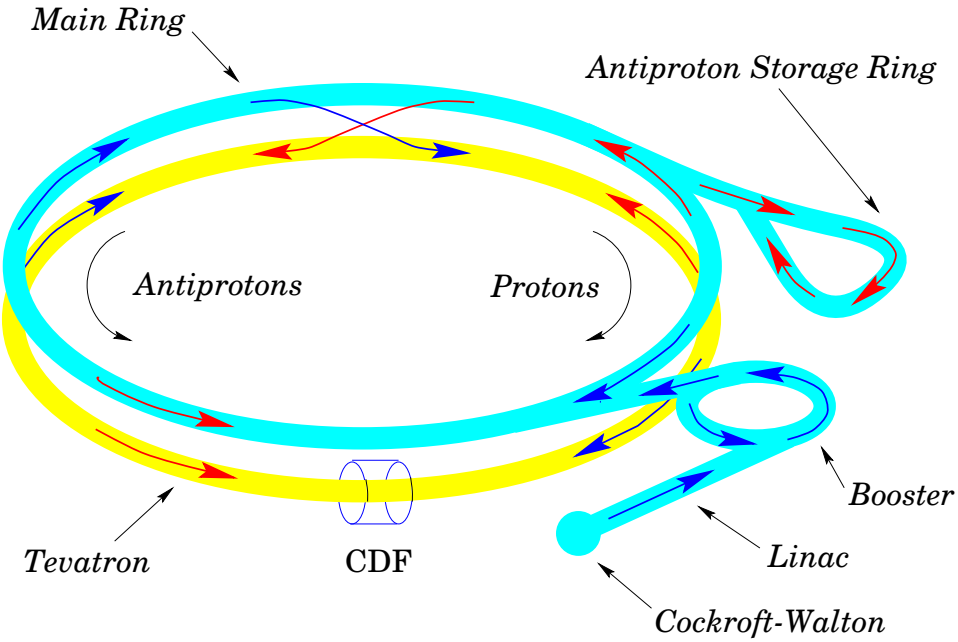

Figure 2.1: The schematic view of the Tevatron.

negative ion. From this procedure, bare protons are captured by the Booster, while the negative ions and H atoms are directed to the beam dump. The new bunch of proton is merged with any beam that is already in the Booster. The Booster fills in six turns with 3×10^{12} protons. Once filled, the carbon foil is removed from the proton path and radio frequency cavities are turned on to accelerate the proton to 8 GeV. The Booster cycle repeats twelve times in rapid succession, loading twelve proton bunched into the Main Ring.

The Main Ring is an another, larger synchrotron with a radius of 1 km. It is located in the same tunnel as the Tevatron, and uses conventional magnets to steer the proton beams. It contains a single radio frequency cavity which further accelerates the proton to 150 GeV prior to injection into the Tevatron. For colliding beam operations, the Main Ring is also used to generate 120 GeV protons for antiproton production.

Antiprotons are created by a portion of the proton beam which has been accelerated to 120 GeV in the Main Ring and sent to the antiproton sources. This proton beam is focused on a tungsten target, producing $p\bar{p}$ pairs. Using a magnetic field, antiprotons are separated from the protons, then focused using a lithium magnet lens and finally sent into the Debuncher. Here the energy spread of the beam then is reduced by

debunching and stochastical cooling. The monochromatic beam then is transfered into the accumulator, where stored until an amount of antiproton is sufficient for the desired luminosity. They are subsequently transfered to the Booster, the Main Ring and finally the Tevatron.

The Main Ring injects the proton and the antiproton beams into the Tevatron. The Tevatron is also a fast-cycling synchrotron, but with superconducting magnets to steer the beams. The Tevatron accelerates the beam to 900 GeV each, namely collides at 1.8 TeV in center-of-mass. In collider modes, six proton and six antiproton bunches revolve in the opposite directions in the Tevatron and collide in two regions with beam crossing every 3.5 μs.

The number of collisions (N) occurring in the Tevatron is giving by

$$N = \sigma \times \int L dt \tag{2.1}$$

where σ is the interaction cross section (in cm^2), L and t are the instantaneous luminosity measured in cm^{-2} s^{-1} and time (in s), respectively.

The Tevatron has had several collision runs so far. The first collision were in 1985, followed by low luminosity run in 1987 and 1988-1989. The two main runs were Run IA (1992-1993) and Run IB (1994-1996).

During Run IA, a proton bunched consisted typically of 12×10^{10} protons, while an antiproton bunched consisted of 3.1×10^{10} antiprotons. For Run IB, the number of the protons and antiprotons per bunch were increased to 22.5×10^{10} and 6.5×10^{10}, respectively.

2.2 The Overview of the CDF Detector

The collision points of the Tavatron are located at two detector: one is the Collider Detector at Fermilab (CDF) and the other is D0 detector. The data used for this analysis is taken with the CDF detector. The CDF detector is a general purpose detector and has been described in detail elsewhere [14]. Figure 2.2 shows the schematic view of one quadrant of the CDF detector. To identify the produced particles, the detector consists

of a tracking system inside a 1.4 T magnetic field, fine-grained calorimeters and muon chambers.

The CDF detector is a solenoidal detector with a forward-backward symmetry, the cylindrical coordinate system centered on the interaction point. The z axis is defined to be the beam axis with the direction of proton motion defining the positive z. A coordinate system where θ and ϕ are the polar and azimuthal angles with respect to the z axis, respectively.

To observe the $p\bar{p}$ collisions, it is not convenient to use the polar angle θ since the interactions are boosted with the respect to the laboratory rest frame. Therefore, events are described using the rapidity y instead of θ. The rapidity is defined as

$$y = \frac{1}{2} \ln \frac{E + p_L}{E - p_L} \tag{2.2}$$

where E and p_L are the total energy and the longitudinal momentum of the particle, respectively. The rapidity is invariant under the Lorenz transforms along the z axis. At the high energy, the rapidity is approximated to be the pseudorapidity η. The pseudorapidity η is defined as

$$\eta = -\ln[\tan(\frac{\theta}{2})]. \tag{2.3}$$

The pseudorapidity is handled more easily than the rapidity since the pseudorapidity depends on only θ.

In $p\bar{p}$ collisions, we can't exactly know the collision energy between the partons, since we don't know their momentum fraction of each collision. Therefore, we use quantities of momentum and energy of the particles transverse to the beam, since the the partons have little transverse energy. The transverse momentum and energy of a particle (p_T and E_T) is denoted as

$$p_T = p \sin\theta. \tag{2.4}$$

$$E_T = E \sin\theta. \tag{2.5}$$

respectively. The missing transverse energy $\not\!\!E_T$ is a magnitude of

$$\vec{\not\!\!E}_T \equiv -\sum E_T^i \, \hat{n}_i. \tag{2.6}$$

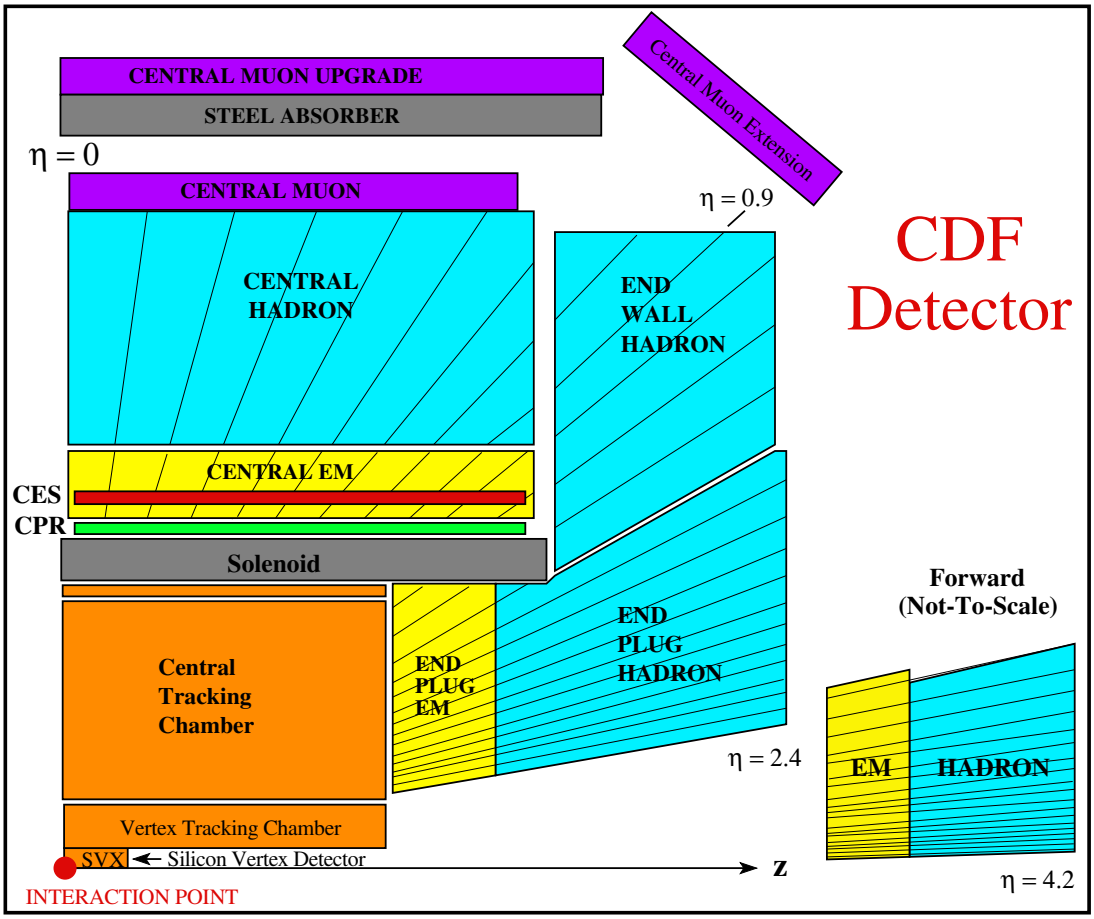

Figure 2.2: The schematic view of one quadrant of the CDF detector during RUN I, 1992 - 1996.

where $\hat{n}_i$ is the unit vector in the transverse plane pointing from the interaction point to the energy deposition in calorimeter cell i.

2.2.1 The Tracking System

The tracking system of CDF detector is a part of the detector close to the beamline. The tracking system is contained within the a solenoidal magnetic field of a 1.4 T. The system consists of the Silicon Vertex Detector (SVX), the Vertex Time Projection Chamber (VTX) and the Central Tracking Chamber (CTC).

The Silicon Vertex Detector

The Silicon Vertex Detector (SVX) is a component of detector closest to the beam pipe. The SVX provides the precise track reconstruction in the plane transverse to the beam and is used to identify the secondary vertex reconstructed from the decay of b hadron.

The SVX consists of two types of modules with a length of 51 cm, one on either side of the beam and centered on $z = 0$. Figure 2.3 shows a schematic view of one SVX module. Each module of the SVX consists of four concentric cylindrical layers of silicon strip detector located at the radii 2.9, 4.3, 5.7 and 7.9 cm. Each layer consists of six detectors in three groups. Each layer is composed of twelve ladders surrounding the beamline. Since the interaction points are distributed at centered $Z = 0$ with $\sigma = 30$cm, the acceptance of the SVX is reduced to 60 %.

The Vertex Time Projection Chamber

The Vertex Time Projection Chamber (VTX) sits surrounding the SVX for reconstructing the tracks in the $r - z$ plane. Figure 2.3 shows a schematic view of the VTX. The length of the VTX is 2.8 m covering a pseudorapidity of $|\eta| \geq 3.25$. The drift gas for the VTX is 1:1 mixture of argon and ethane. The VTX consists of 24 individual modules, which are divided into 2 drift regions in z direction and 8 octants in φ. The VTX is used to measure the position of the primary vertex along the z direction.

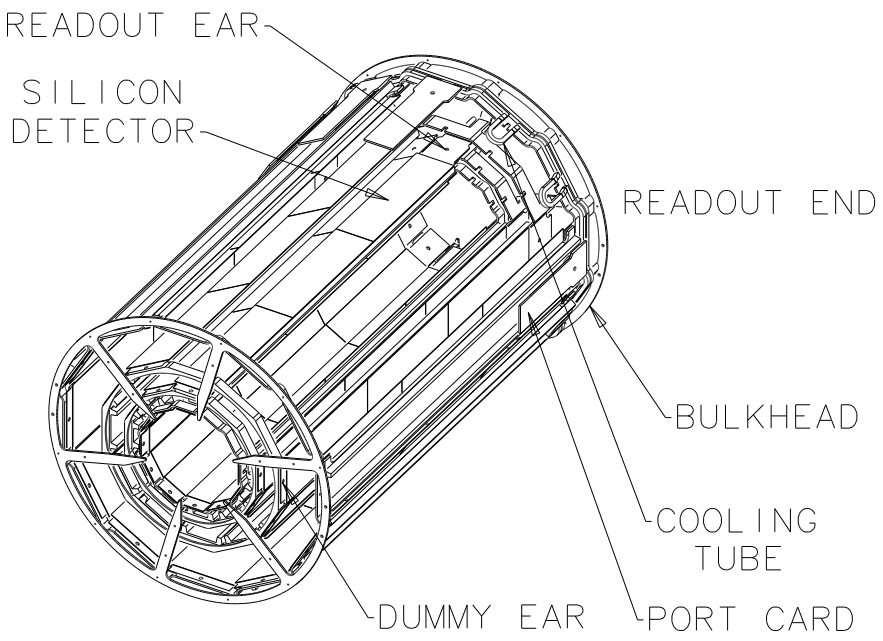

Figure 2.3: The schematic view of the one barrel of Silicon Vertex Detector.

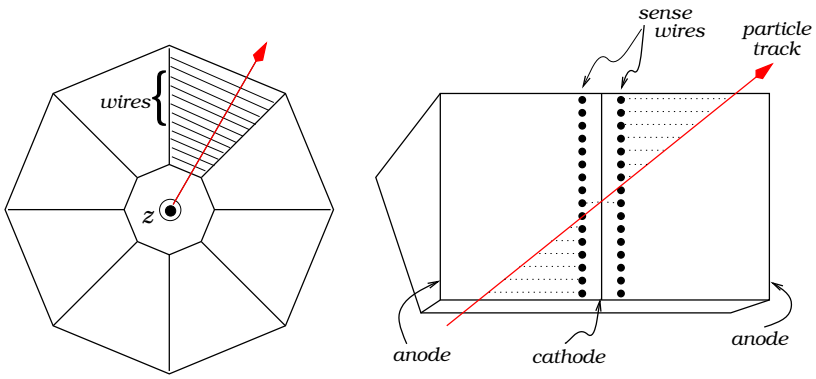

Figure 2.4: The schematic view of the VTX.

The Central Tracking Chamber

The Central Tracking Chamber (CTC) is a 3.2 m long cylindrical drift chamber covering the region $|z| < 160$ cm and $27.7 < r < 138$ cm. It covers the pseudorapidity of $|\eta| < 1.0$ at the outer layer while $|\eta| < 2.0$ at the inner layer. Figure 2.5 shows the $(x - y)$ view of the CTC end plate. The gas mixture used for the CTC is 49.6% for argon and 49.6% for ethane with an additional small amount (0.8%) of ethanol. It consists of 84 layers with 6156 gold-plated tungsten sense wires. The diameter and space of wire is 40 μm and 10 mm, respectively. The 84 layers are grouped into 9 superlayers. The five of these layer wire are grounded into five superlayers (axis superlayers) containing 12 layers each. The wires of these layer are parallel to the z direction. The remaining 24 layers are arranged into 4 superlayers (stereo superlayers) containing 6 layers each. The wires of the stereo superlayers are tilted by 3° with respect to z direction.

The CDF tracking algorithm starts by reconstructing charged tracks in the $r - \phi$ plane using the axis superlayers. The spatial resolution of the CTC is about 200 μm, which yields a two tracks resolution of about 5 mm. The momentum resolution is $\delta p_T / p_T = 0.002 \times p_T$.

2.2.2 The Calorimeter System

The CDF calorimeters are built as projective tower covering a pseudorapidity of $|\eta| < 4.2$, surrounding tracking volume, and are used to identify electrons and jets. The calorimeters are divided into three regions, central ($|\eta| < 1.1$), plug ($1.1 < |\eta| < 2.4$), and forward region ($2.2 < |\eta| < 4.2$). Each calorimeter consists of an electromagnetic and a hadronic part. Figure 2.6 shows the segmentation of the CDF calorimeters in the $\eta - \phi$ plane.

The Central Calorimeter

The central calorimeter is composed of layers of scintillators and absorber materials. It is divided into 24 wedges, each covering 15 degree in the ϕ. Each wedge consists of towers covering $\Delta\eta = 0.1$.

Electrons are identified using the central electromagnetic calorimeter (CEM). The

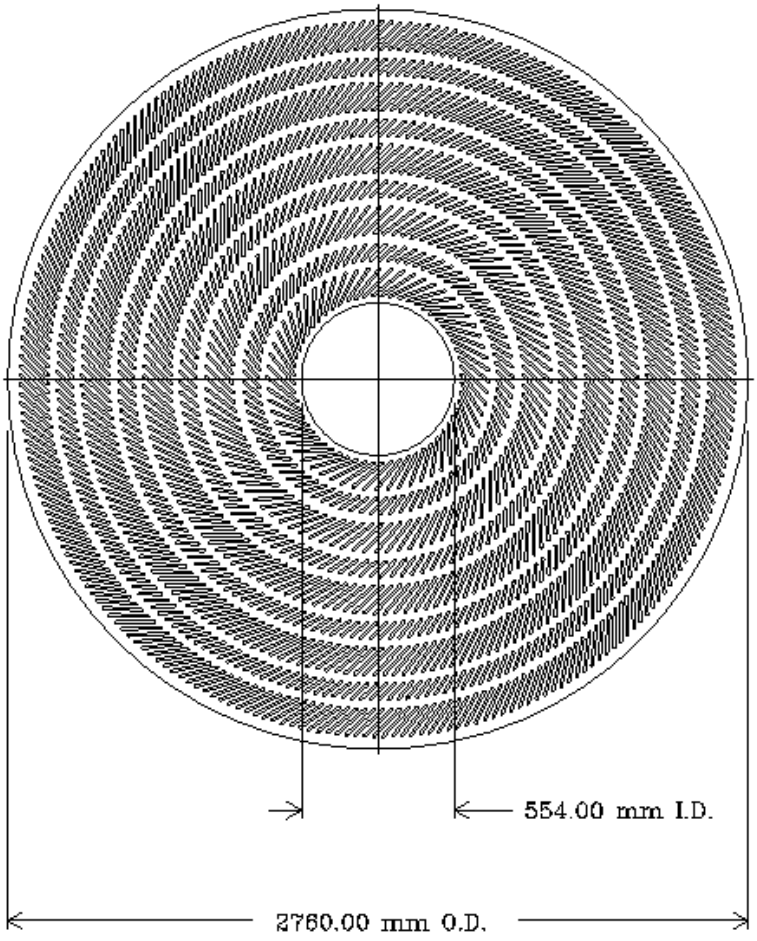

Figure 2.5: The $x - y$ view of the Central Tracking Chamber.

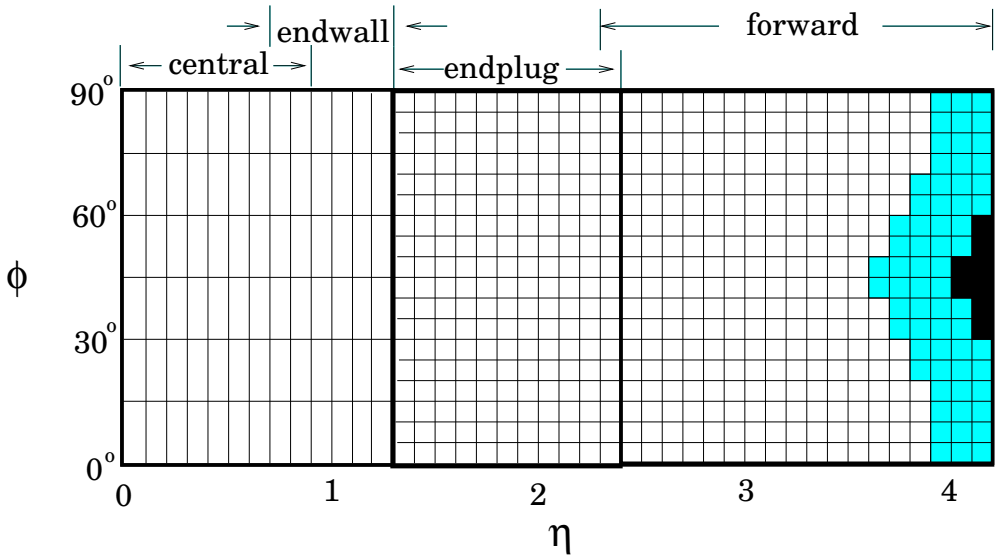

Figure 2.6: the segmentation of the CDF calorimeters in the $\eta - \phi$ plane.

CEM uses 31 layers of 3.2 mm lead sheets and 5 mm sheets of plastic scintillator. Each CEM has readout by two photomultiplier tubes, one at each end. The energy resolution is given by

$$\frac{\Delta E}{E} = \left[\left(\frac{13.5\%}{\sqrt{E_T}} \right)^2 + (2\%)^2 \right]^{\frac{1}{2}}. \tag{2.7}$$

In the CEM, there is a set of proportional strip and wire chambers (CES). The CES is used to measure the transverse shower profile of particles passing through the CEM. The spatial resolution is 2 mm.

The central hadron calorimeter (CHA) uses 32 layers of 25 mm steel plates alternated with 10 mm of plastic scintillators in the coverage of $|\eta| < 0.9$. There is an additional endwall calorimeter including a part of the CHA, covering $0.9 < |\eta| < 1.3$. The endwall calorimeter (CHA) uses 15 layers of 10 mm steel plates alternated with 10 mm of plastic scintillators. The CHA energy resolution is

$$\frac{\Delta E}{E} = \left[\left(\frac{75\%}{\sqrt{E_T}} \right)^2 + (3\%)^2 \right]^{\frac{1}{2}}. \tag{2.8}$$

The Plug Calorimeter

The plug calorimeters are composed of the same absorber materials as the central calorimeter, while drift chambers are replaced by the plastic scintillators. The segmentation is 0.1 in the η and 5° in ϕ.

The gas mixture of the drift chamber is argon and ethane in the electromagnetic and the hadronic calorimeter (PEM and PHA). The resolution of energy is $28\%/\sqrt{E}$ and $130\%/\sqrt{E}$ for PEM and PHA, respectively.

2.2.3 The Muon System

Muons are identified by tracks in the muon chambers surrounding the calorimeters. The central CDF muon chambers are separated into three parts, CMU, CPU and CMX. Figure 2.7 shows the segmentation of the central CDF muon chambers in the $\eta - \phi$ plane.

The CMU and CMP

The central muon chamber (CMU) is located behind the central calorimeter, covering $\eta < 0.6$. The CMU consists of four layers of drift chambers. Each wedge is composed of three 4.2° modules, segmented in wedge of 12.6°. The gas mixture for the chambers is argon and ethane with the additional of ethanol. The muon's hit position is measured using the charged division and the drift chamber time-to-distance relationship for z and ϕ, respectively. The spatial resolutions for z and ϕ are 1.2 mm and 250 μm, respectively. There is a possibility for punch-through of the high energetic jet to be identified as muons. To reduce such a misidentification, the central muon upgrade (CMP) is located behind the CMU. The CMP is composed of four layers of the drift chambers. These are separated from the CMU by 0.6 m steel. The detector coverage of the CMU and CMP is about 84% and 63%. An area covering a both CMU and CMP is approximately 53%.

The CMX

A third muon detector subcomponent is the central muon extension (CMX) in the region $0.6 < |\eta| < 1.0$. The CMX consists of four free-standing conical arches on either side

of the central regions. Each arch contain four layers of drift chambers between the scintillator counters for a trigger. The CMX covers about 71% of the solid angle in $0.6 < |\eta| < 1.0$ due to the obstacles.

2.3 The Data Taking

We are interested in high Q^2 events in the hadron collisions. However these events are a small fraction of the total and hidden in a large background of other events. Therefore, selection criteria are applied to the raw data. The data passed selection criteria are stored to the tapes. These selection criteria are included in a set of hardware and software filter called triggers.

The Trigger System

The CDF employs a three level triggers system. Each level has various paths to obtain interesting physics processes.

The first trigger level, called as Level 1, is based on the states of several detector subsystems. If there is a certain amount of energy in the central calorimeters, tracks in the CTC or hits of muon chamber, the events will be accepted and be forwarded to the next trigger level. This decision process takes less than the time of beam crossing (3.5 μ). At typical instantaneous luminosity of 1×10^{31} cm^{-2}s^{-1} at Tevatron, the Level 1 trigger rate is about 1 kHz.

The next trigger level (Level 2) is a digital hardware trigger. The difference between Level 1 and 2 is the combination of different detector subsystem for the main data selection. Furthermore, the Level 2 trigger is introduced to prescaling. A certain ratio of less important events is rejected in order to keep all the important events, while these events would be passed the Level 2. The prescaling is two mechanisms which depended on the events. The one is the stat prescale, which is set at the beginning of data taking and is not changed for the several hours that the run ends. The other is the dynamic prescale. In contrast with stat prescale, the dynamic prescale is adapted to the luminosity changes during the individual runs. Thus it is possible to take a higher

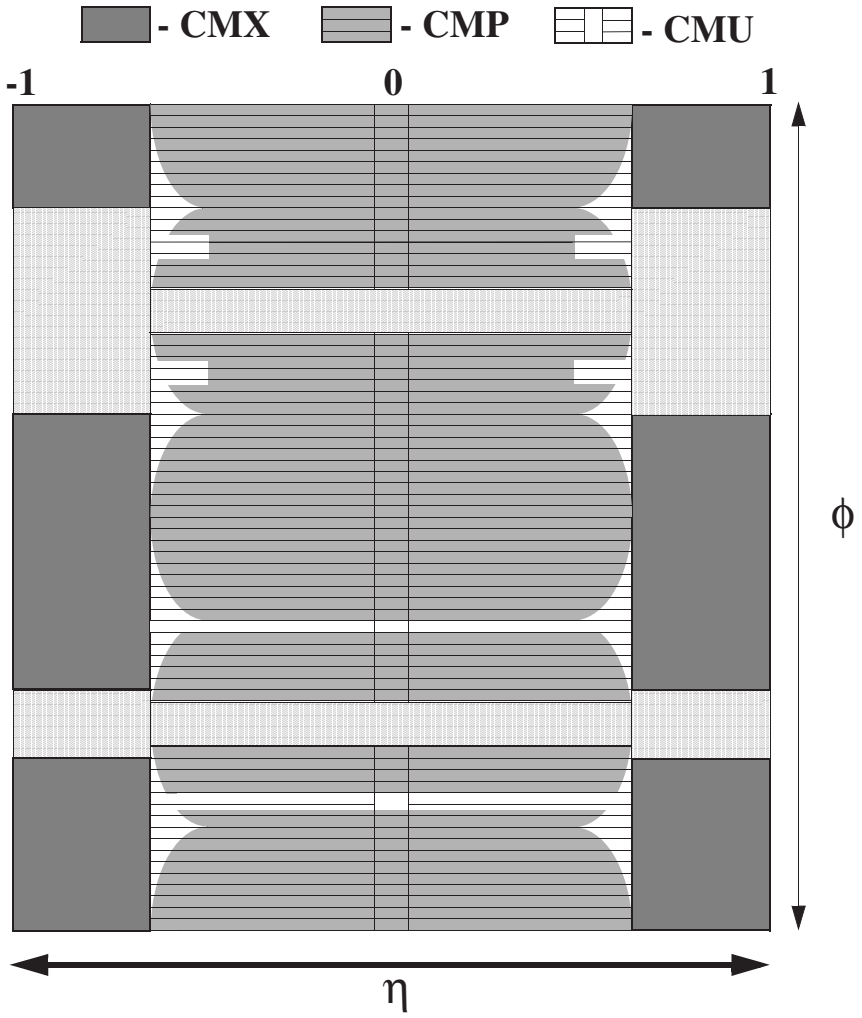

Figure 2.7: The segmentation of the central CDF muon chambers in the $\eta - \phi$ plane.

percentage of the events during a low luminosity than during a high luminosity. The typical trigger rate at Level 2 is about 12 Hz.

The last trigger, denoted by Level 3, is implemented as software triggers. These software triggers run on a farm of Silicon Graphics Servers. The computer farm runs a special version of the CDF offline code and has the complete detector informations available. This level is mainly used to reject bad events and apply the similar quantities as the offline selection cut. The output rate of this trigger level is 5-7 Hz.

Chapter 3

Data Process and Analysis

3.1 How to Determine the Cross Section for the Stop Pair Production

Discussed in Chapter 1, our interesting process is the lightest scalar top quark pair production and the the lightest scalar top quark decays into τ lepton and b-quark.

The events of our objective have the signature chosen as an electron (e) from $\tau \to e\nu_e\nu_\tau$, a hadronically decaying τ lepton (τ_h) and two jets from two b-quarks.

The production cross section of $\tilde{t}_1\bar{\tilde{t}}_1$ ($\sigma_{\tilde{t}_1\bar{\tilde{t}}_1}$) with considering the branching ratio of $\tilde{t}_1 \to \tau^+ b$ ($B(\tilde{t}_1 \to \tau^+ b)$) are written as follows:

$$\sigma_{\tilde{t}_1\bar{\tilde{t}}_1} \cdot B(\tilde{t}_1 \to \tau^+ b)^2 = \frac{N^{can}_{\tilde{t}_1\bar{\tilde{t}}_1} - N^{BG}_{\tilde{t}_1\bar{\tilde{t}}_1}}{A_{\tilde{t}_1\bar{\tilde{t}}_1} B_{e\tau_h} \int \mathcal{L}\, dt} \tag{3.1}$$

where $N^{can}_{\tilde{t}_1\bar{\tilde{t}}_1}$ and $N^{BG}_{\tilde{t}_1\bar{\tilde{t}}_1}$ are the number of candidates from the data and expected backgrounds for $\tilde{t}_1\bar{\tilde{t}}_1$ production, respectively. The $B_{e\tau_h}$ is the branching ratio which one tau decays into the electron channel and the other into the hadronic channel. The $B_{e\tau_h}$ is calculated as follows:

$$\begin{aligned} B_{e\tau_h} &= 2 \times B(\tau \to e\nu\bar{\nu}) \cdot B(\tau \to \tau_h \nu) \\ &\simeq 2 \times 0.18 \times 0.64 = 0.23\ . \end{aligned} \tag{3.2}$$

And the $\int \mathcal{L}\, dt$ refers to the integrated luminosity. The $A_{\tilde{t}_1\bar{\tilde{t}}_1}$ is the acceptance for $\tilde{t}_1\bar{\tilde{t}}_1 \to \tau\tau b\bar{b}$ events. Although the acceptance is calculated by the MonteCalro (MC) sim-

ulation, we know that there are some differences between the data and the MC because our detector simulation overestimates performance a little and does not incorporated luminosity and aging effects. Therefore, we need to consider a correction factors of an identification and an isolation cuts for electron and τ_h assigned as f_e and f_{τ_h} concerning to the acceptance for $\tilde{t}_1\bar{\tilde{t}}_1$ events, respectively. By using the above correction factors, the $A_{\tilde{t}_1\bar{\tilde{t}}_1}$ can be written as follows:

$$A_{\tilde{t}_1\bar{\tilde{t}}_1} = A^{MC}_{\tilde{t}_1\bar{\tilde{t}}_1} \cdot \epsilon^{trg}_{\tilde{t}_1\bar{\tilde{t}}_1} \times f_e \cdot f_{\tau_h} \ , \tag{3.3}$$

where $A^{MC}_{\tilde{t}_1\bar{\tilde{t}}_1}$ is the acceptance for $\tilde{t}_1\bar{\tilde{t}}_1 \to \tau\tau b\bar{b}$ by calculated by MC, and $\epsilon^{trg}_{\tilde{t}_1\bar{\tilde{t}}_1}$ is the trigger efficiency. The f_e is studied in Refs. [19] and [20]. However, f_{τ_h} has not been studied yet due to its difficulty.

We expect that same situation occurs in the $Z^0 \to \tau\tau$ which have e and τ_h events in final states similarly, therefore we need also to use the identical correction factors of e and τ_h in the acceptance for Z^0 events. Assuming the f_e and f_{τ_h} for $Z^0 \to \tau\tau$ are the same values as those for $\tilde{t}_1\bar{\tilde{t}}_1 \to \tau\tau b\bar{b}$, the production cross section of $Z^0 \to \tau\tau$ event $(\sigma_{Z^0} \cdot B(Z^0 \to \tau\tau))$ is written as follows:

$$\begin{aligned} \sigma_{Z^0} \cdot B(Z^0 \to \tau\tau) &= \frac{N^{can}_Z - N^{BG}_Z}{A_Z B_{e\tau_h} \int \mathcal{L}\, dt} \\ &= \frac{N^{can}_Z - N^{BG}_Z}{(A^{MC}_Z \cdot \epsilon^{trg}_Z \times f_e \cdot f_{\tau_h}) B_{e\tau_h} \int \mathcal{L}\, dt} \end{aligned} \tag{3.4}$$

where, N^{can}_Z and N^{BG}_Z are the number of candidates in the data and expected backgrounds, respectively. A_Z is the acceptance for $Z^0 \to \tau\tau$, while A^{MC}_Z denotes the acceptance for $Z^0 \to \tau\tau$ calculated from MC with the trigger efficiency, ϵ^{trg}_Z.

As both Eqs. (3.4) and (3.1) include $\int \mathcal{L}\, dt$, $B_{e\tau_h}$, f_e, and f_{τ_h} as their common parameters, we can cancel those common parameters by combining the two equations, and obtain the production cross section of $\tilde{t}_1\bar{\tilde{t}}_1$ as follows:

$$\begin{aligned} \sigma_{\tilde{t}_1\bar{\tilde{t}}_1} \cdot B(\tilde{t}_1 \to \tau^+ b)^2 &= \frac{N^{can}_{\tilde{t}_1\bar{\tilde{t}}_1} - N^{BG}_{\tilde{t}_1\bar{\tilde{t}}_1}}{A_{\tilde{t}_1\bar{\tilde{t}}_1} \int \mathcal{L}\, dt} \\ &= \frac{N^{can}_{\tilde{t}_1\bar{\tilde{t}}_1} - N^{BG}_{\tilde{t}_1\bar{\tilde{t}}_1}}{A^{MC}_{\tilde{t}_1\bar{\tilde{t}}_1} \cdot \varepsilon^{trg}_{\tilde{t}_1\bar{\tilde{t}}_1} \cdot \left(\dfrac{N^{can}_Z - N^{BG}_Z}{\sigma_{Z^0} \cdot B(Z^0 \to \tau\tau) \cdot A^{MC}_Z \cdot \varepsilon^{trg}_Z} \right)} \end{aligned}$$

$$= \left(\frac{N^{can}_{\tilde{t}_1\bar{\tilde{t}}_1} - N^{BG}_{\tilde{t}_1\bar{\tilde{t}}_1}}{N^{can}_{Z} - N^{BG}_{Z}}\right) \cdot \left(\frac{A^{MC}_{Z} \cdot \varepsilon^{trg}_{Z}}{A^{MC}_{\tilde{t}_1\bar{\tilde{t}}_1} \cdot \varepsilon^{trg}_{\tilde{t}_1\bar{\tilde{t}}_1}}\right) \cdot \sigma_{Z^0} \cdot B(Z^0 \to \tau\tau) \ . \quad (3.5)$$

In the normalization using $Z^0 \to \tau\tau$ events, we have two merits and one demerit. One of the merits is cancellation of several parameters mentioned above. The one more merit is reduction of systematic uncertainties of the identification and isolation of electron and τ_h. The demerit of this method is to involve large uncertainties from the statistical error from the $Z^0 \to \tau\tau$ data.

Thus, we will study the events of $Z^0 \to \tau\tau$ for the usage in the acceptance calculations, and $\tilde{t}_1\bar{\tilde{t}}_1$ signal process.

3.2 Signal Selection

3.2.1 Used Dataset Sample

This analysis is based on the low p_T electron dataset samples. The integrated luminosity for the dataset is 19.7 pb^{-1} for Run IA and 84.9 pb^{-1} for Run IB. Table 3.1 shows the Level 2 (L2) and Level (L3) triggers we explicitly require for our analysis. The L2 and L3 trigger efficiencies are given in Refs. [21] and [22] for Run IA and Refs. [23] and [24] for Run IB. The criteria requirements on L2 are "energy deposits in CEM calorimeters" and "high p_T tracks found in CTC". The E_T threshold for this single low p_T electron trigger is 8 (9) GeV for RUN IA (IB). In addition, one track is required in the CTC with $p_T > 7.5$ GeV/c that points at the calorimeter tower in ϕ. For RUN IB, the CES was added to the trigger system [25]. The electron trigger requires the presence of pulse height in the CES corresponding to an electromagnetic shower energy of 4 GeV or greater. Also, the ϕ position of the shower is available with the segmentation of $\Delta\phi = 2°$. The prescaled luminosity for the L2 trigger for Run IB is 73.6 ± 3.0 pb^{-1} [26].

3.2.2 Central Electron Selection

We require at least one well-identified electron in the central region ($|\eta_{det}| < 1$) with $p_T(e) \equiv E_T^{em} \geq 10$ GeV/c and $p_T^{trk} \geq 8$ GeV/c. Furthermore, we require $|z_0^{electron} - z_{vtx}| \leq$

Table 3.1: Electron trigger dataset for electron+τ_h sample

Trigger	Run IA	Run IB
Level 2	CEM_9_SEED_9_SH_7_CFT_9_2*	CEM_8_CFT_7_5_XCES*
Level 3	ELE1_CEM_8_6*	ELEB_CEM_8_6*
	ELE1_CEM_9*	

Table 3.2: Electron identification quality cuts

Charged track requirement	$E^{em}/p^{trk} \leq 1.8$
Strip chamber pulse height shape	$\chi^2_{strip} \leq 10.0$
Track-shower matching variables	$\lvert\Delta x\rvert \leq 1.5$ cm, $\lvert\Delta z\rvert \leq 3.0$ cm
Leakage into the hadron calorimeters	$E^{had}/E^{em} \leq 0.05$
Calorimeter transverse profile	$L_{share} \leq 0.2$
Fiducial volume	`fidele.cdf`
Conversion Removal	`convert2.cdf`

5 cm, and $|z_{vtx}| \leq 60$ cm. The position in z of the primary event vertex is measured by the VTX.

The electron identification criteria are based on the informations in which energy and momentum are measured by the central calorimeter and the CTC, respectively. The electron identification criteria are summarized in Table 3.2, which are basically the standard electron quality cuts used in the CDF analysis [27]. The detailed criteria of each term are listed below.

Charged track requirement

Electromagnetic cluster in the calorimeter can arise from neutral particles, such as $\pi^0 \rightarrow \gamma\gamma$ decay. We require the presence of charged track in the CTC for electron identification. We require the ratio of electromagnetic energy, E, of the electron cluster measured in

the calorimeter to the electron's momentum, p, measured in the CTC to lie in the range $E/p < 1.8$

Strip chamber pulse height shape

The CES chamber can be used to observe the longitudinal development of shower. An electromagnetic shower in the calorimeter is generally initiated much earlier than for a hadron. The sum over 5 strips (z view) around the track's position extrapolated to the strip chambers.

The pulse height shape in the CES is also used for electron identification. The pulse height shape is compared with the test beam data by χ^2 test. The variable χ^2_{strip} means the χ^2 of the fit of the energy deposited on each of 11 strips in z in the CES compared with the test beam shape.

Track-shower matching variable

The CTC track pointing to the electron cluster is extrapolated to the CES, and the extrapolated position is compared tith the shower position measured in the CES. The variable Δx means the separation in the $r - \phi$ view between the extrapolated track position and the CES strip cluster position. The variable Δz means the separation in the z direction‘.

Leakage into the hadron calorimeters

The ratio of the energy in the hadronic towers by the electron (E^{had}) to the energy in the electromagnetic towers by the electron (E^{em}), E^{had}/E^{em} is used to further select good electron. The electromagnetic calorimeters nearly contain electromagnetic showers, while in general deposit energy in both the hadronic and electromagnetic compartment. This quantity depends on the event situation but it is clear that isolated electrons have less hadronic energy nearby them than would electrons produced in associated hadrons.

Calorimeter transverse profile

The transverse profile (L_{share}) of a central electron allows a comparison of the lateral sharing of energy in the calorimeter towers of an electron cluster to electron shower shapes gained in test beam data. The L_{share} is defined as

$$L_{share} = 0.14 \sum_i \frac{E_i^{ad} - E_i^{prob}}{0.14^2 E + (\Delta E_i^{prob})^2} \tag{3.6}$$

where E_i^{ad} is the measured energy (in GeV) in a tower adjacent to the seed tower, E_i^{prob} is the expected energy (in GeV) in the adjacent tower, $0.14^2 E$ (in GeV) is the error on the energy measurement and ΔE_i^{prob} (in GeV) is calculated using a parameterization from the beam test data. The sum is over two towers adjust to the seed tower in the same azimuthal wedge. Since L_{share} is defined in each shower, we expect to large differences in this variable when comparing electrons and jets.

Fiducial Volume

The fiducial volume is the requirement that electron has hit a region of the detector with well-understood response. The CDF has standard routines called as `fidele.cdf` and we use it to check the good region for the electron.

Conversion Removal

The electrons from the photon conversion become backgrounds for our analysis and need to remove such a events. We use a routine called as `convert2.cdf` to identify these electrons. This routine checks the consistency of a conversion pair by combing the identified electron and the second electron candidate tracks in an event.

3.2.3 $Z^0 \to ee$ Removal

If the electron can be misidentified as one prong τ_h decay product, this means that $Z^0 \to ee$ events are potentially large background for our analysis. Therefore, in the Z^0 removal, it needs to be more stringent than for the standard dilepton analysis. So, we

Table 3.3: Cuts for $Z^0 \to ee$ removal.

Calorimeter-based removal	**Track-based removal**
$E_T^{em} > 8$ GeV	$p_T^{trk} > 10$ GeV/c
	$I^{trk}(\Delta R = 0.4) \leq 0.05$
$E^{had}/E^{em} < 0.12$	EM Fraction > 0.7
	$\lvert z_0^{trk} - z_0^{electron} \rvert \leq 8$ cm
Opposite sign charge	Opposite sign charge
76 GeV/c^2< $M(ee)^{cal}$ < 106 GeV/c^2	76 GeV/c^2< $M(ee)^{trk}$ < 106 GeV/c^2

strictly use the calorimeter informations and the track informations to remove the Z^0 events.

We remove the events as Z^0 events if the invariant mass formed by the well-identified electron and calorimeter based loose electron mentioned above is between 76 and 106 GeV/c^2.

After the calorimeter-based Z^0 removal, the electron may be still identified as a possible τ_h candidate since an electron goes up a detector crack, causing tail of electron identification selection criteria. Therefore, we use a routine as `tauzee.cdf`[17] which remove these Z^0 events based a second CTC track. The summary of the cut criteria is shown in 3.3.

3.2.4 Electron Isolation

Furthermore, the electron is required to be isolated and the condition is that the energy difference, subtracting the electron energy in the calorimeter from the E_T in a cone of $\Delta R \equiv \sqrt{(\Delta\eta)^2 + (\Delta\phi)^2} = 0.4$ around the electron, should be less than 4 GeV. The isolation in the calorimeter (ISO^{cal})is defined as

$$ISO^{cal} \equiv \sum_{\Delta R<0.4} E_T^{cal,i} - E_T^{clu,e} < 4 \text{ GeV} \tag{3.7}$$

where $E_T^{cal,i} \equiv E_T^{em,i} + E_T^{had,i}$ represents the energy deposit on the ith calorimeter tower, and $E_T^{clu,e}$ is the cluster energy deposited on the calorimeter by the electron. Similarly,

the isolation in CTC ISO^{trk} is also required as

$$ISO^{trk} \equiv \sum_{\Delta R<0.4} p_T^{trk,i} - p_T^{trk,e} < 4 \text{ GeV}/c, \tag{3.8}$$

where $p_T^{trk,i}$ represents the transverse momentum around the electron, and $p_T^{trk,e}$ is the transverse momentum of the electron.

3.2.5 Central τ_h Selection

The hadronically decaying τ lepton candidates are identified as a calorimeter clusters with $E_T > 4$ GeV in $|\eta| < 1.0$ with

$$p_T(\tau_h) \equiv p_T^{trk+\pi^0} \equiv \sum_{10^\circ cone} p_T^{trk} + E_T^{em(\pi^0)} \geq 15 \text{ GeV}/c \,.$$

where $\sum_{10^\circ cone} {p_T}^{trk}$ is the sum of the momentum in the 10° cone, and the $E_T^{em(\pi^0)}$ is the energy of any identified π^0's, as measured in the EM calorimeter. The π^0 is identified from the CES using $\pi^0 \to \gamma\gamma$. We require to satisfy the following requirements which is not identified as a e and μ. The each criteria are explained below.

Track multiplicity

Since τ lepton decays hadronically into one-prong or three-prong mainly, we require that a reconstructed τ has a track multiplicity of either one or three in a 10° cone around the tau-like jet cluster center and the total electric charge should be ± 1.

$$\text{1 or 3 tracks in } 10^\circ \text{ cone with } |\sum_i Q_i| = 1$$

Number of π^0

The τ decay basically do not involve more than two π^0's. Therefore we require to be less than three π^0 in a tau-like cluster.

$$\text{Number of } \pi^0\text{'s} < 3$$

The ratio of energy to momentum

We incorporate π^0's by defining $E_T^{clu}/p_T^{trk+\pi^0}$ as $E_T/p_T^{trk+\pi^0}$. This cut is mostly useful for removing fake three prongs and high p_T one-prongs. We apply the $E_T^{clu}/p_T^{trk+\pi^0}$ cut as follows,

$$0.5 < E_T^{clu}/p_T^{trk+\pi^0} < 2.0 \text{ (for 1-prong)}$$

or

$$0.5 < E_T^{clu}/p_T^{trk+\pi^0} < 1.5 \text{ (for 3-prong)}$$

RMS cluster width

The RMS width σ_{cl} of cluster is defined as the second moment of the E_T distribution among the towers in the cluster:

$$\sigma_{cl} = \sqrt{\sigma_\phi^2 + \sigma_\eta^2} \tag{3.9}$$

where $\sigma_\phi = \sqrt{< (\phi_i - < \phi >)^2 >}$ and $\sigma_\eta = \sqrt{< (\eta_i - < \eta >)^2 >}$.

We use the center of gravity of the energy detected by the two photomultiplier tubes for calculating ϕ_i in the each tower to get the best possible ϕ resolution from calorimeter. In the η distribution, the center of the tower is also used.

$$\sigma_{cl} < 0.11 - 0.025 \times E_T^{clu}/100 \text{ (for 1-prong)}$$

or

$$\sigma_{cl} < 0.13 - 0.034 \times E_T^{clu}/100 \text{ (for 3-prong)}$$

Mass

We reconstructed the invariant mass ($M(\tau_h)$) as τ by the tracks in the 10° cone and the π^0's associated with tau-like jet cluster.

$$M(\tau_h) \equiv M(trk, \pi^0) < 1.8 \text{ GeV}/c^2$$

Tracking isolation

We set a cut on the tracking isolation (I^{trk}) defined as the scalar sum of of all tracks in $\Delta R = 0.4$ around the cluster center but excluding those inside the 10° cone. We require that I^{trk} is less than 1 GeV/c.

$$I^{trk} < 1 \text{ GeV}/c$$

Prompt electron removal

Electron produces very narrow clusters with one track pointing and can therefore be mistaken as one-prong τ_h lepton. The tau-like cluster with high electromagnetic fraction is rejected as follows.

$$\text{1-prong with } E_T^{clu}/p_T^{trk} < 4, \text{ EM fraction} > 0.9$$
$$\text{or}$$
$$\text{clusters with EM fraction} > 0.95$$

Prompt muon removal

Muons are minimum ionizing particles and deposit a little energy in the hitted calorimeter towers that they hit. However, as the seed tower E_T requirement for a tau-like cluster is only 4 GeV, it is not unlikely that tau-like cluster is created due to muons. The tau-like clusters are rejected too, if there is a muon stub within 15° of the tau-like cluster or if the energy deposition in CEM and CHA is consistent with that of minimum ionizing particle. We reject clusters with

$$\text{(a) } E_T^{clu} < 8 \text{ GeV}, 0.05 < E^{em} < 2 \text{ GeV}, 0.5 < E^{had} < 5 \text{ GeV}$$
$$\text{or}$$
$$\text{(b) a muon stub with } |\phi_\tau - \phi_{stub}| < 15° \text{ as muon}$$

The τ_h identification quality cuts. are summarized in Table 3.4. The efficiency of τ_h identification is obtained to be 56.5 ± 1.7(stat)% [17].

3.2.6 Results After e and τ_h Selection

We select events with a central electron with $p_T(e) \geq 10$ GeV/c and a hadronically decaying τ lepton with $p_T(\tau_h) \geq 15$ GeV/c from the Run I low p_T electron trigger datasets. We obtain total of 730 $e + \tau_h$ events after our $e + \tau_h$ selection. In this sample, a total of 479 opposite-sign (OS) $e+\tau_h$ events survive after our selection, while 251 like-sign (LS) $e + \tau_h$ events are retained. It should be noted that opposite-sign (OS) $e + \tau_h$ events seem to contain $\tilde{t}_1\bar{\tilde{t}}_1$ candidate events, while like-sign $e + \tau_h$ events are dominantly QCD fake events, discussed in the next chapter.

3.3 Study of the Constituents in the Signal Sample

3.3.1 Monte Carlo Samples

In previous section, we select a signal sample including an electron and a hadronically decaying τ lepton. In this section, we study the constituents in the signal samples using the like-sign data and Monte Carlo simulation data.

Table 3.5 shows a list of the possible background sources of the $e + \tau_h$ events in our sample. In the present analysis, the number of expected opposite-sign (OS) and like-sign (LS) events expected by the combination of the electron and τ_h from the SM processes except QCD process (N_{MC}^{OS} and N_{MC}^{LS}) are estimated using Monte Carlo (MC) program. We use QFL$'$ for the CDF detector simulation with CTEQ4L parton distribution functions (PDFs) [28]. The used MC program are listed in Table 3.6. The MC samples of $\gamma/Z^0 \rightarrow \tau\tau$ events are generated by ISAJET[29] in the region of $5 \leq q_T \leq 500$ GeV/c which effectively reproduces the multiplicity and E_T distributions of jets in Z^0 boson production[30]. VECBOS [31] is used for the production and decay of vector boson associated with jets, followed fragmentation and hadronization of quark/gluon using HERWIG [32]. We choose $Q^2 = < p_T >^2$ for the QCD parameter of renormalization and fragmentation in both VECBOS and HERWIG. We normalize the VECBOS cross section by the r-factor [33]. The VECBOS samples of $W(\rightarrow \tau\nu) \geq n$ jets and $Z^0(\rightarrow \tau\tau) \geq n$ jets are generated by replacing electron with τ at the generator level. TAUOLA[34] and QQ[35]

Table 3.4: τ_h identification quality cuts

Number of tracks:	1 or 3 ($\|\sum_i Q_i\| = 1$) in 10° cone
Number of π^0's:	< 3
E/p:	$0.5 < \frac{E_T^{clu}}{p_T^{trk+\pi^0}} < 2.0$ (1-prong) $0.5 < \frac{E_T^{clu}}{p_T^{trk+\pi^0}} < 1.5$ (3-prong)
RMS cluster width:	$\sigma_{cl} < 0.11 - 0.025 \times E_T^{clu}/100$ (1-prong) $\sigma_{cl} < 0.13 - 0.034 \times E_T^{clu}/100$ (3-prong)
Mass:	$M(\tau_h) \equiv M(trk, \pi^0) < 1.8$ GeV/c^2
Tracking isolation:	$I^{trk} < 1$ GeV/c
Prompt electron removal:	Reject (a) 1-prong with $E_T^{clu}/p_T^{trk} < 4$, EM fraction > 0.9 or (b) clusters with EM fraction > 0.95
Prompt muon removal:	Reject cluster with (a) $E_T^{clu} < 8$ GeV, $0.05 < E^{em} < 2$ GeV, $0.5 < E^{had} < 5$ GeV or (b) a muon stub with $\|\phi_\tau - \phi_{stub}\| < 15°$ as muon

are used to simulate τ and b decays, respectively.

The MC study of QCD events are not carried out in the present analysis. However, the most of the QCD events in the opposite-sign $e + \tau_h$ sample are estimated by using the like-sign $e + \tau_h$ sample to be mentioned in next Subsection 3.3.2. We calculate the expected numbers from the MC samples (N_{MC})as follows:

$$\begin{aligned} N_{MC} &= [\sigma \cdot B \times \int \mathcal{L}\, dt] \times \frac{\text{\# of events passed}}{\text{\# of events generated}} \\ &\times \text{[L1 \& L2 \& L3 trigger efficiencies]} \\ &\times \text{[MC correction factor for electron ID cut]} \\ &\times \text{[MC correction factor for electron isolation cut].} \end{aligned}$$

The product of the production cross section and the branching ratio ($\sigma \cdot B$) are taken from the CDF measurements [36, 37, 38, 39] for Z^0/γ^*, $t\bar{t}$ and W^+W^- productions and the next-to-leading order (NLO) calculations for the $W^{\pm}Z^0$ and Z^0Z^0 productions [40, 41]. We assume $\sigma \cdot B(Z^0 \to ee) = \sigma \cdot B(Z^0 \to \tau\tau)$. The correction factors of the electron identification and isolation cut in the MC samples are obtained values, 97% [19] and 98% [20], respectively.

3.3.2 QCD Background

There are two major background sources of the like-sign events. One is QCD jets events (gluons, light quarks, $b\overline{b}/c\overline{c}$) and the other is $W(\to e\nu)$ + jets events. The QCD events are generated to have both fake e and fake τ_h, while $W(\to e\nu)$ + jets events have either e or τ_f fake from jets.

Here, the both fake rates from QCD events are low, nevertheless the QCD events have so large cross section that the QCD background becomes meaningfully large and it is the most difficult to estimate all of them with the MC in detail. Therefore, in order to estimate the QCD fake, we simply use like-sign data since they have no or weak charge correlation between e and τ_h fake. From this conjecture, we assume that the contained fake numbers in both opposite and like-sign e and τ_h data after excluding $W+$ jet events are same.

Table 3.5: Sources to $e + \tau_h$ events

real e + real τ_h	real e + fake τ_h	real τ_h + fake e	fake e + fake τ_h
$\gamma^*/Z^0 \to \tau\tau$	$W(\to e\nu)$ + jets	$W(\to \tau\nu)$ + jets	
	$W(\to \tau\nu \to e\nu\nu\nu)$ + jets		
$t\bar{t}$	$t\bar{t}$	$t\bar{t}$	
diboson	diboson	diboson	
QCD($b\bar{b}/c\bar{c}$)	QCD($b\bar{b}/c\bar{c}$)	QCD($b\bar{b}/c\bar{c}$)	QCD
	$\gamma^*/Z^0 \to ee$		

Table 3.6: Summary of Monte Carlo samples

Process	Monte Carlo	$\sigma \cdot B$
$Z^0(\to \tau\tau)$	ISAJET	231±12 pb [36]
$\gamma^*(\to \tau\tau)$	ISAJET	259±57 pb [37]
$Z^0(\to \tau\tau)$ + jets	VECBOS + HERWIG	$\sigma_{\text{VECBOS}} \times r$-factor[33]
$W(\to e\nu)$ + jets	VECBOS + HERWIG	$\sigma_{\text{VECBOS}} \times r$-factor[33]
$W(\to \tau\nu)$ + jets	VECBOS + HERWIG	$\sigma_{\text{VECBOS}} \times r$-factor[33]
$t\bar{t}$	ISAJET	$6.5\pm^{1.7}_{1.4}$ pb [38]
WW	ISAJET	$10.2\pm^{6.3}_{5.1} \pm 1.6$ pb [39]
WZ^0	ISAJET	2.66 pb [40]
Z^0Z^0	ISAJET	1.08 pb [41]

3.3.3 Comparison with the Signal Sample

Using the MC and like-sign data, we can calculate the expected number of the SM events in the opposite-sign e and τ_h, and describe this calculation process below.

From discussion in Subsection. 3.3.2, after removing the expected non QCD like-sign events from like-sign data, we obtain the number of QCD contribution. That is,

$$N_{QCD}^{exp} = N_{data}^{LS} - N_{nonQCD}^{LS} \tag{3.10}$$

where N_{QCD}^{exp}, N_{data}^{LS} and N_{nonQCD}^{LS} are numbers of expected QCD process, like-sign data and non QCD like-sign processes. The number of the non QCD like-sign processes can be estimated using the MC. Furthermore, we assume that the QCD processes have the same number in both opposite and like-sign e and τ_h data, as discussed in Subsection. 3.3.2. We estimate expected opposite- and like-sign numbers of background except QCD processes from MC samples (N_{MC}^{OS} and N_{MC}^{LS}). Thus, the number of expected opposite-sign data (N_{exp}^{OS}) can be calculated using the MC and like-sign data as follows

$$\begin{aligned} N_{exp}^{OS} &= N_{MC}^{OS} + N_{QCD}^{exp} && (3.11)\\ &= N_{MC}^{OS} + N_{data}^{LS} - N_{nonQCD}^{LS} && (3.12)\\ &= N_{MC}^{OS} + N_{data}^{LS} - N_{MC}^{LS}. && (3.13) \end{aligned}$$

Table 3.7 shows a summary of yields in the data and MC events. The expected number of opposite-sign events is estimated to be 447.3±16.3 using the method mentioned in the previous sections, while the number of opposite-sign events in the data is 479±22(stat). Figure 3.1 shows the distributions of transverse energy of electron ($E_T(e)$), transverse momentum of τ_h ($p_T(\tau_h)$), azimuthal angle between electron and τ_h ($\Delta\phi(e,\tau_h)$), azimuthal angle between electron and missing E_T ($\not\!\!E_T$) ($\Delta\phi(e,\not\!\!E_T)$), $\not\!\!E_T$, and invariant mass of electron and τ_h ($M(e,\tau_h)$), respect with the data and expected opposite-sign events, respectively. The kinematic variable distributions agree well with data and the background estimation.

Table 3.7: Summary of yields of $e + \tau_h$ pairs in the data and MC events after our e and τ_h selection. The uncertainty is only statistical.

Low-E_T($\geq$10 GeV) Electron Analysis			
Process	OS	LS	OS−LS
$Z^0(\rightarrow \tau\tau)$	138.5	0.7	137.8±0.8
$\gamma^*(\rightarrow \tau\tau)$	2.3	0.0	2.3±0.4
$W(\rightarrow e\nu)$	65.3	19.7	45.6±3.6
$W(\rightarrow \tau\nu)$	11.3	2.6	8.7±1.3
$t\bar{t}$	0.73	0.10	0.63±0.10
WW	1.01	0.16	0.85±0.07
WZ^0	0.20	0.10	0.10±0.01
Z^0Z^0	0.34	0.08	0.26±0.04
Total background	219.7	23.4	196.3 ± 3.9
Data (IA+IB)	479±22	251±16	228±27
Expected OS events	447.3±16.3	N.A.	N.A.

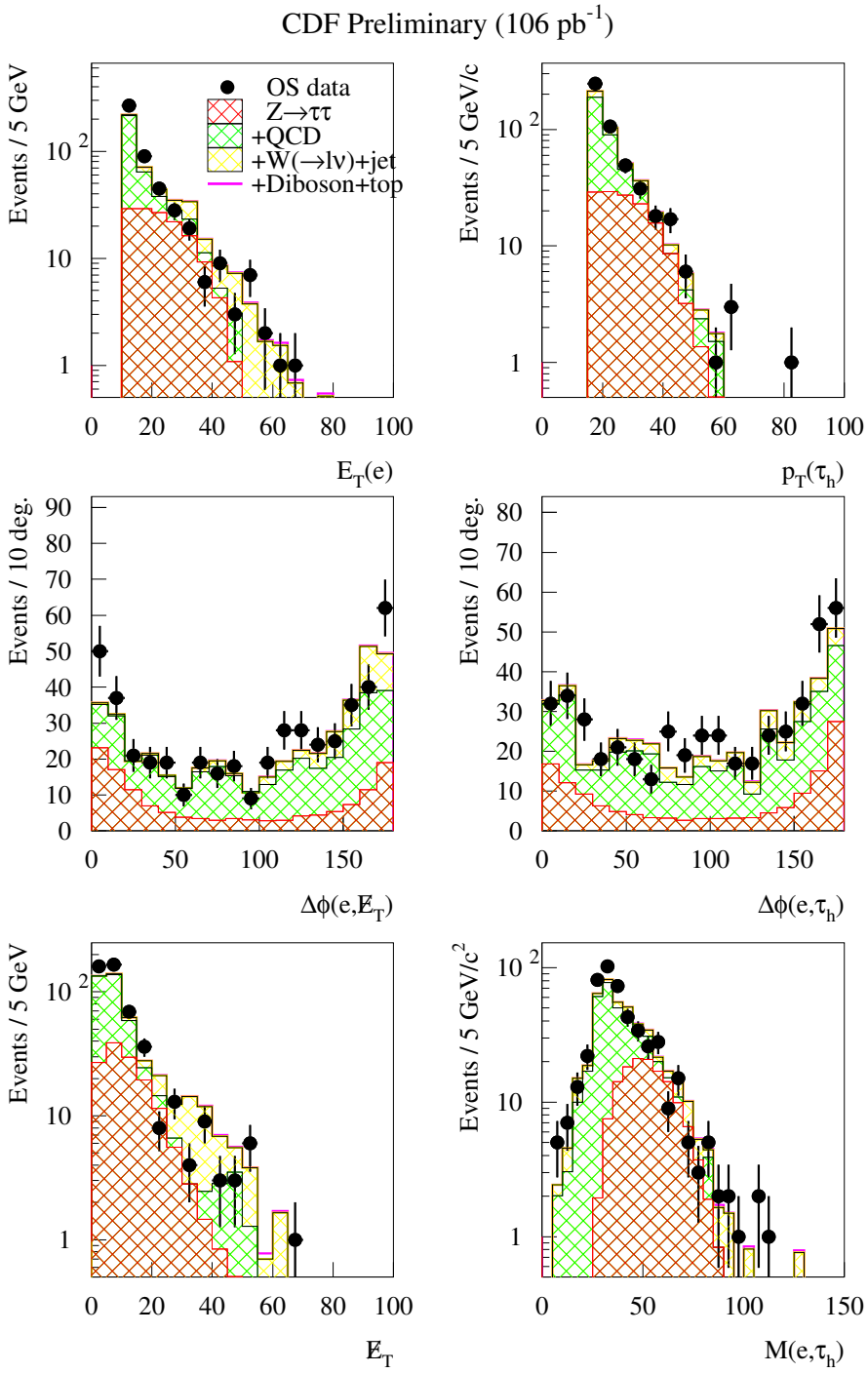

Figure 3.1: Distributions of $E_T(e)$, $p_T(\tau_h)$, $\Delta\phi(e,\tau_h)$, $\Delta\phi(e,\not\!\!E_T)$, $\not\!\!E_T$ and $M(e,\tau_h)$ for data and expectation of opposite-sign events after our e and τ_h selection.

3.4 Signal Event Section

In this section, we describe the detail of analysis about the $Z^0 \to \tau\tau$ and $\tilde{t}_1\bar{\tilde{t}}_1$ events, to obtain the final signal events.

3.4.1 $Z^0 \to \tau\tau$ Event Selection

In Section 3.3, the sources making the opposite-sign $e + \tau_h$ in our samples are $Z^0 \to \tau\tau$, W+jets and QCD processes, while the like-sign events are W+jets and QCD processes. We apply the following additional selection to our sample in order to obtain the $Z^0 \to \tau\tau$ events with high purity.

We first remove the W+jets events from both opposite- and like-sign samples in order to obtain QCD fake process from like-sign samples. We use a cut on the transverse mass of the electron and $\not\!\!E_T$, defined as

$$M_T(e, \not\!\!E_T) \equiv \sqrt{2E_T(e)\not\!\!E_T(1 - \cos\phi_{e\not\!\!E_T})} \tag{3.14}$$

where $\phi_{e\not\!\!E_T}$ is the azimuthal opening angle of the electron and the $\not\!\!E_T$. This cut is insensitive to the charge correlation. Figure 3.2 shows the distributions of $M_T(e, \not\!\!E_T)$ for the data and MC along with the distribution of the significance as a function of $M_T(e, \not\!\!E_T)$. The significance is defined as the ratio of the expected number of signal (N_{SIG}) to square root of expected number of background (N_{BG}) after the cut, $N_{SIG}/\sqrt{N_{BG}}$, where both numbers are obtained from the MC samples. From Figure 3.2, the $Z^0 \to \tau\tau$ process are dominant in low M_T region while $W(\to e\nu)$ + jets events are distributed in 40 GeV/c^2or greater. Consequently, we require the criteria as below,

$$M_T(e, \not\!\!E_T) \leq 25 \text{ GeV}/c^2. \tag{3.15}$$

After applying this $M_T(e, \not\!\!E_T)$ cut, the like-sign events is contained the QCD events dominantly. Furthermore, to reduce the QCD process, we apply a cut on the transverse momentum of the electron + $\not\!\!E_T$ system: $p_T(e, \not\!\!E_T) \equiv |\vec{E}_T(e) + \vec{\not\!\!E}_T|$. Figure 3.3 shows the distributions of $p_T(e, \not\!\!E_T)$ for the data and MC after the $M_T(e, \not\!\!E_T)$ cut along with the distribution of the significance as a function of $p_T(e, \not\!\!E_T)$, where the expected number

from QCD is obtained from the like-sign events in the data. We require the cut as

$$p_T(e, \not\!\!E_T) \geq 25 \text{ GeV}/c^2. \tag{3.16}$$

As a result of the above cuts application, we obtain 69 opposite-sign and 8 like-sign events in the data. The acceptance and trigger efficiency for $Z^0 \to \tau\tau \to e + \tau_h + X$ (A^Z_{MC} and ε^Z_{trg}) are found to be 1.48 $\pm$ 0.02 (stat) % and 74.5 %, respectively.

Until these steps, one event is not distinguished which is the stop or $Z^0 \to \tau\tau$ candidates. Since the majority of the stop events is expected to have more than two jets from two b-quarks as discussed later, we try to separate the stop from $Z^0 \to \tau\tau$ events using the number of jets as $Z^0 \to \tau\tau$ events have no jet, dominantly. Applying the jet-veto, namely only 0-jet event is selected after the above cuts. Here, the jets are identified by a fixed cone algorithm [46] and required to have the raw transverse energy $E_T^{raw} > 10$ GeV, the corrected transverse energy $E_T^{corr} > 15$ GeV and $|\eta_{det}| < 2.4$. We determine the acceptance of the $Z^0 \to \tau\tau$ events with 0-jet by using the measurement of $Z^0(\to ee) + \geq n$ jets at CDF[42]. We calculate the expected number of $Z^0 \to \tau\tau$ events as below. The ratio of 0-jet events to the total (R(0-jet)) obtained from the analysis of $Z^0(\to ee) + \geq n$ jets as follows:

$$\begin{aligned} R(\text{0-jet}) &= R(\geq 0 \text{ jet}) - R(\geq 1 \text{ jet}) \\ &= 1 - \frac{\sigma_{Z^0}(\geq 1 \text{ jet})}{\sigma_{Z^0}(\geq 0 \text{ jet})} \\ &= 0.8040 \pm 0.0065(\text{stat+sys}) \pm 0.0238(\text{Jet Def.}) \,. \end{aligned} \tag{3.17}$$

Consequently, the expected number of $Z^0 \to \tau\tau$ events with 0 jet is calculated as below:

$$\begin{aligned} N^Z_{expected} &= A^Z_{MC} \cdot f_e \cdot \varepsilon^Z_{trg} \cdot B_{e\tau_h} \cdot \sigma \cdot B(Z^0 \to \tau\tau) \cdot \int \mathcal{L}\, dt \times R(\text{0-jet}) \\ &= 47.5 \pm 0.6(\text{stat}) \end{aligned} \tag{3.18}$$

Table 3.8 shows the number of events in the data and MC for $Z^0 \to \tau\tau$ and W + jets for each cut. Table 3.9 summarizes the number of events in the data and MC for $Z^0 \to \tau\tau$ and W + jets after the 0-jet selection. The expected number of $Z^0 \to \tau\tau$ events with 0-jet is 47.2 $\pm$ 0.6(stat) $\pm$ 2.8(sys) from MC. The number of opposite-sign events subtracted by background is 45.6 $\pm$ 7.8(stat) $\pm$ 0.2(sys). The some kinematic distributions respect

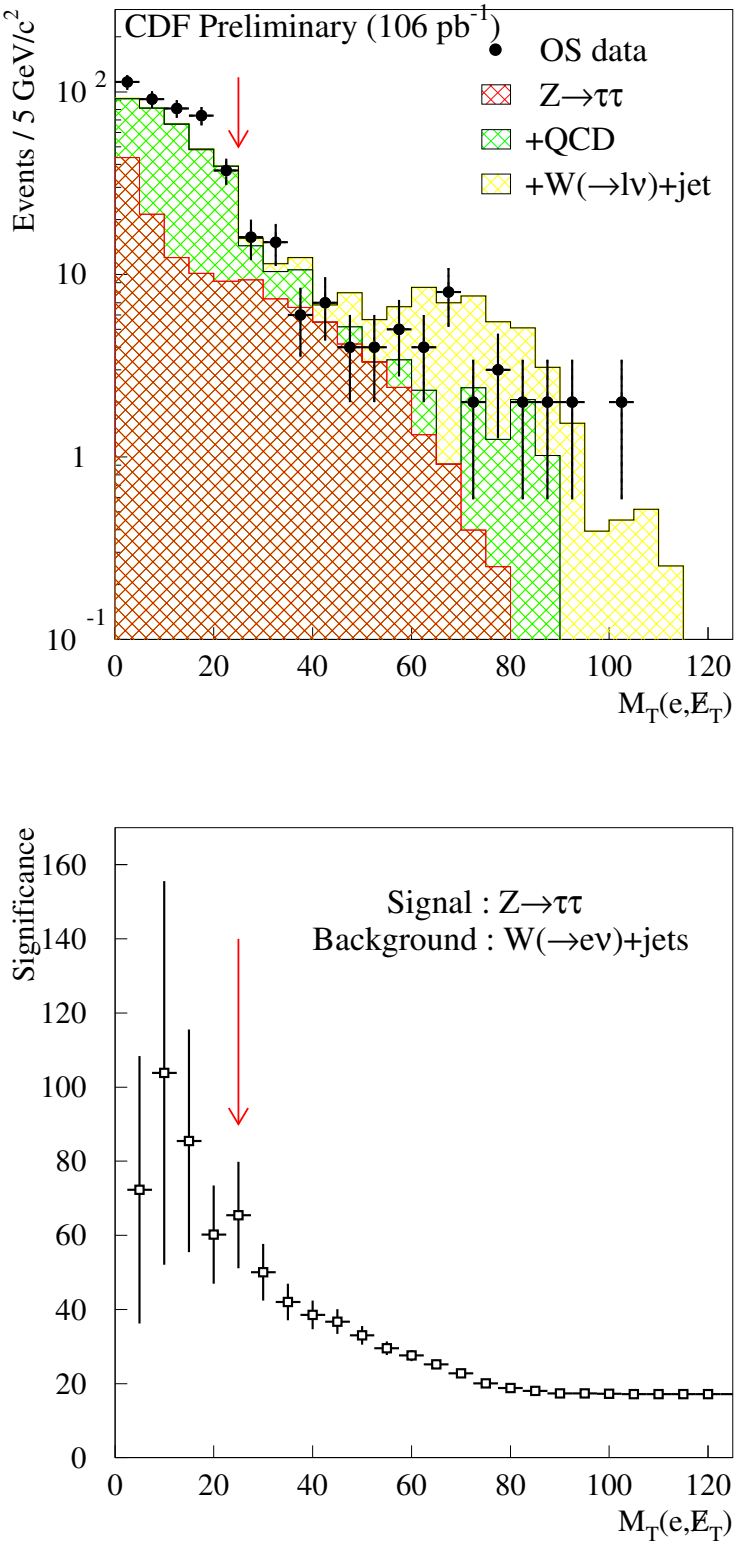

Figure 3.2: Distributions of $M_T(e, \not\!\!E_T)$ (top) and significance (bottom)

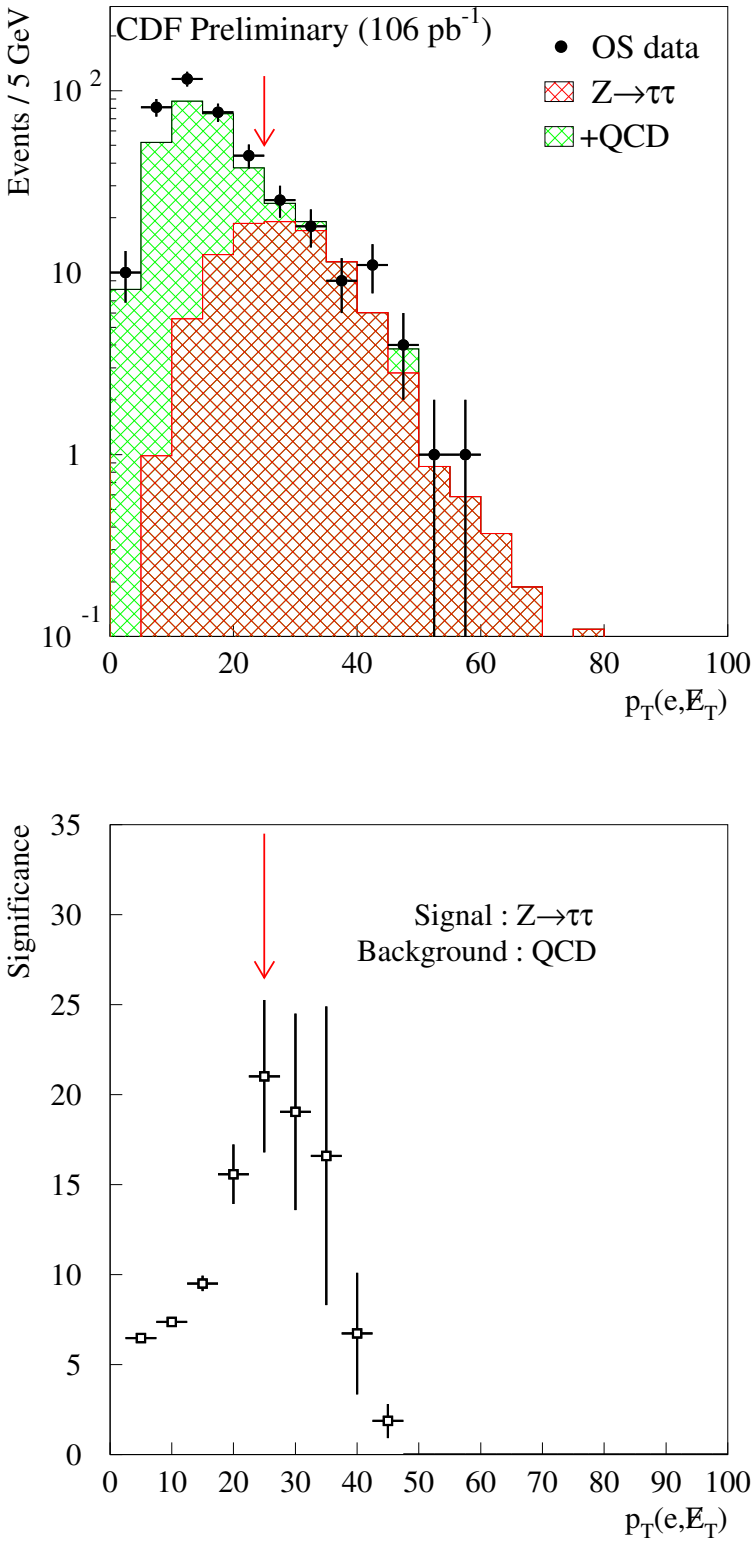

Figure 3.3: Distributions of $p_T(e, \not\!\!E_T)$ (top) and significance (bottom)

to opposite-sign data and expected background are shown in Figure 3.4. We obtain the good agreement between the MC and data after our $Z^0 \to \tau\tau$ event selection.

We also accept the events with a τ_h-like object by track multiplicity (removing the 1 and 3-prong requirements). The charge of τ_h-like object is defined to be the charge of the highest-p_T track. Figure 3.5 shows the charged track multiplicity of the hadronic tau decays and shows excellent agreement with background expectations which are dominated by real τ production and decay. We can see one and three tracks bin excess in the opposite-sign data and this effect is easily understood as the hadronically tau lepton decay.

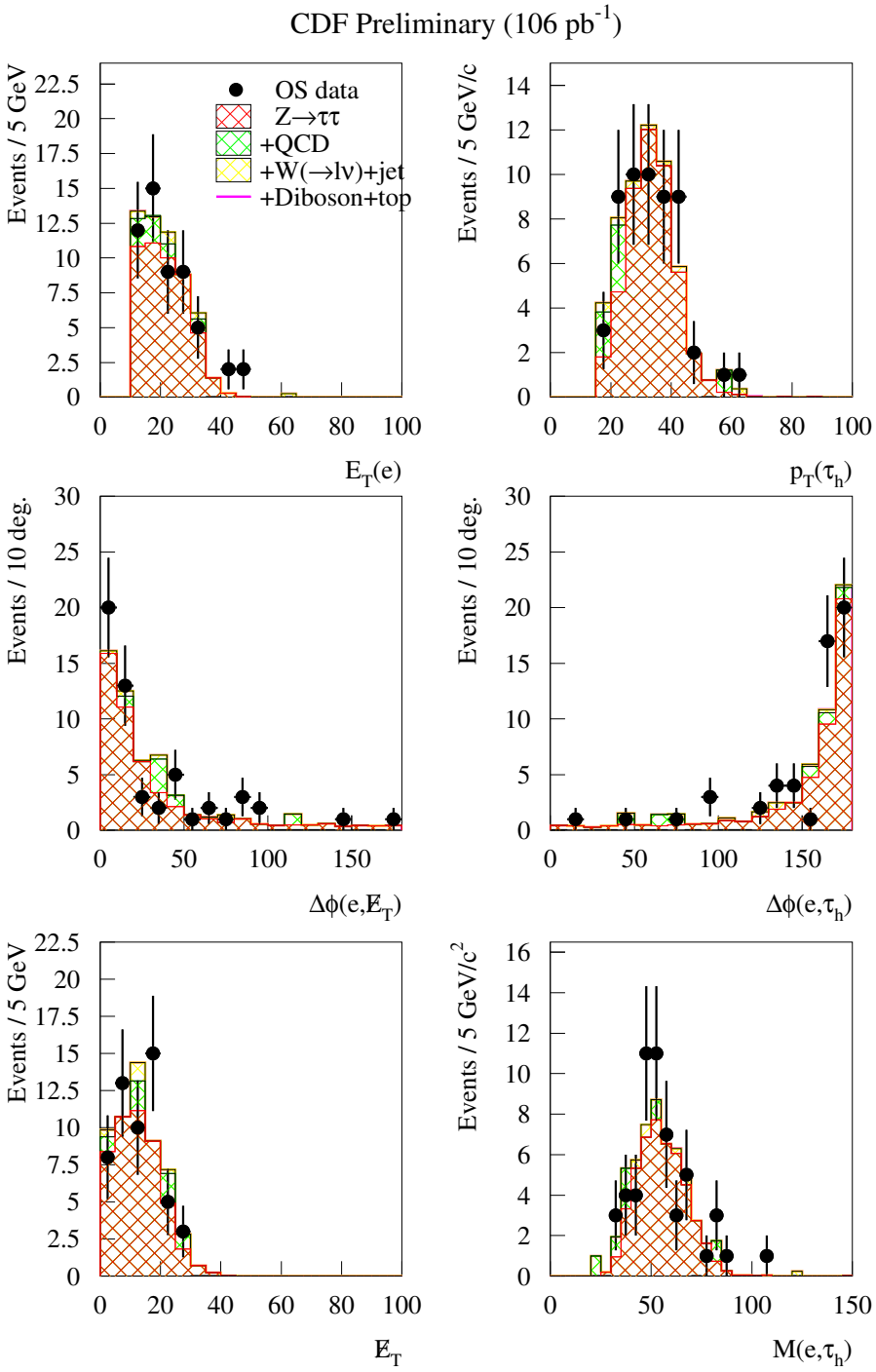

Figure 3.4: Distributions of $E_T(e)$, $p_T(\tau_h)$, $\Delta\phi(e,\tau_h)$, $\Delta\phi(e,\not\!\!E_T)$, $\not\!\!E_T$ and $M(e,\tau_h)$ for data and expectation of opposite-sign events after $Z^0 \to \tau\tau$ with 0-jet selection cuts.

Table 3.8: Number of events in data and MC samples after each cut

[$e + \tau_h$]	$Z^0(\rightarrow \tau\tau)$		$W(\rightarrow e\nu)$+jets		Data	
Cut	OS	LS	OS	LS	OS	LS
Baseline	138.5	0.7	65.3	19.7	479	251
$M_T(e, \not\!\!E_T)$ cut	96.7	0.5	2.2	0.8	396	230
$p_T(e, \not\!\!E_T)$ cut	59.0	0.4	1.0	0.3	69	8
jet-veto cut	47.5	0.3	0.8	0.3	54	6

Table 3.9: Summary of yields of $e + \tau_h$ pairs in the data and MC events after $Z^0 \rightarrow \tau\tau$ with 0-jet selection cut.

Process	OS	LS	OS − LS
$Z^0 \rightarrow \tau\tau$	47.5	0.3	47.2 ± 0.6 (stat) ± 2.8 (sys)
$\gamma \rightarrow \tau\tau$	0.4	0.0	0.4 ± 0.2 ± 0.1
$W(\rightarrow e\nu)$+jets	0.8	0.3	0.5 ± 0.4 ± 0.1
$W(\rightarrow \tau\nu)$+jets	1.5	0.0	1.5 ± 0.4 ± 0.1
Diboson,Top	0.02	0.0	0.02 ± 0.01 ± 0.01
Data	54	6	48 ± 8

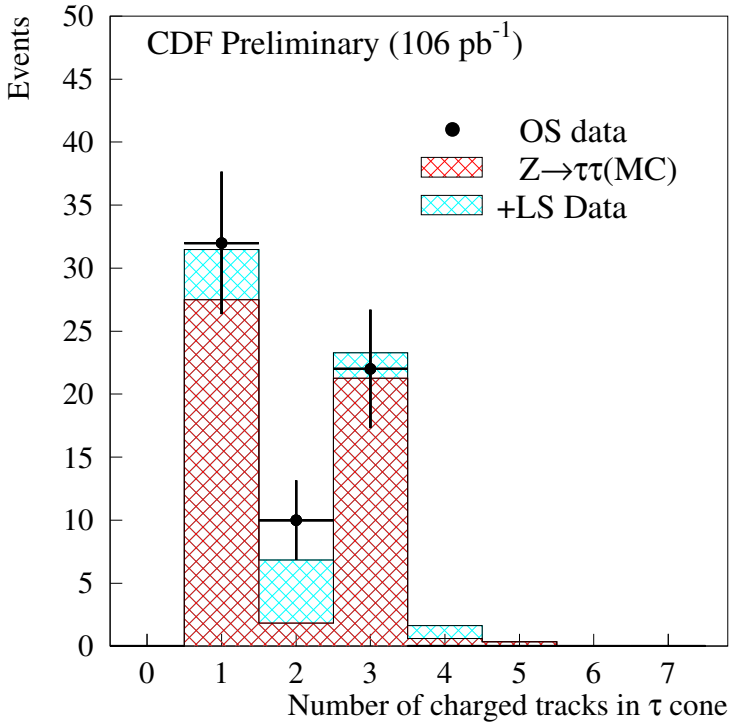

Figure 3.5: Number of charged tracks in τ cone after $Z^0 \rightarrow \tau\tau + 0$ jet selection

3.4.2 $\tilde{t}_1\bar{\tilde{t}}_1$ Event Selection

We use ISAJET v7.44 to generate $\tilde{t}_1\bar{\tilde{t}}_1$ events with the CTEQ4L parton distribution function for our analysis.

We begin with removing the W + jets events from both opposite-sign and like-sign samples using $M_T(e, \not\!\!E_T)$, which is the same definition described in Subsection 3.4.1. In this case, we set the criteria as

$$M_T(e, \not\!\!E_T) \leq 35 \text{ GeV}/c^2 \,. \tag{3.19}$$

Figure 3.6 shows the distributions of the $M_T(e, \not\!\!E_T)$ for the data and MC events along with the distribution of the significance as a function of the $M_T(e, \not\!\!E_T)$ in case of the $\tilde{t}_1$ mass being 100 GeV/c^2. And the criteria values are seemed to be very reasonable.

In the next step, we apply a cut on the scaler sum of the transverse energy of the electron, transverse momentum of τ_h and $\not\!\!E_T$: $H_T(e, \tau_h, \not\!\!E_T) = E_T(e) + p_T(\tau_h) + \not\!\!E_T$ in order to remove the QCD events which are dominant after the $M_T(e, \not\!\!E_T)$ cut. Figure 3.7 shows the distributions of $H_T(e, \tau_h, \not\!\!E_T)$ for the data and MC along with the distribution of the significance as a function of $H_T(e, \tau_h, \not\!\!E_T)$. We require the criteria reasonably as

$$H_T(e, \tau_h, \not\!\!E_T) \geq 75 \text{ GeV}/c^2 \,. \tag{3.20}$$

Figure 3.8 shows the distributions of the opposite-sign data and the background estimated with the MC and like-sign data after two cuts described above. The kinematic variable distributions agree well with data and the background estimation. The opposite-sign events dominantly survive the $Z^0 \to \tau\tau$ events after two cuts described above.

Finally, we apply a cut on the number of jets (N_{jet}). The definition of jet here is the same as the case of $Z^0 \to \tau\tau$ analysis in Subsection 3.4.1. Figure 3.9 shows the distributions of N_{jet} for the data and MC along with the distribution of significance as a function of N_{jet}. We compare the $\tilde{t}_1\bar{\tilde{t}}_1$ events with the $Z^0 \to \tau\tau$ events generated by ISAJET. We decide the N_{jet} criteria as

$$N_{jet} \geq 2 \,. \tag{3.21}$$

Table 3.10 shows the event selection efficiencies and trigger efficiencies for $\tilde{t}_1\bar{\tilde{t}}_1 \to$

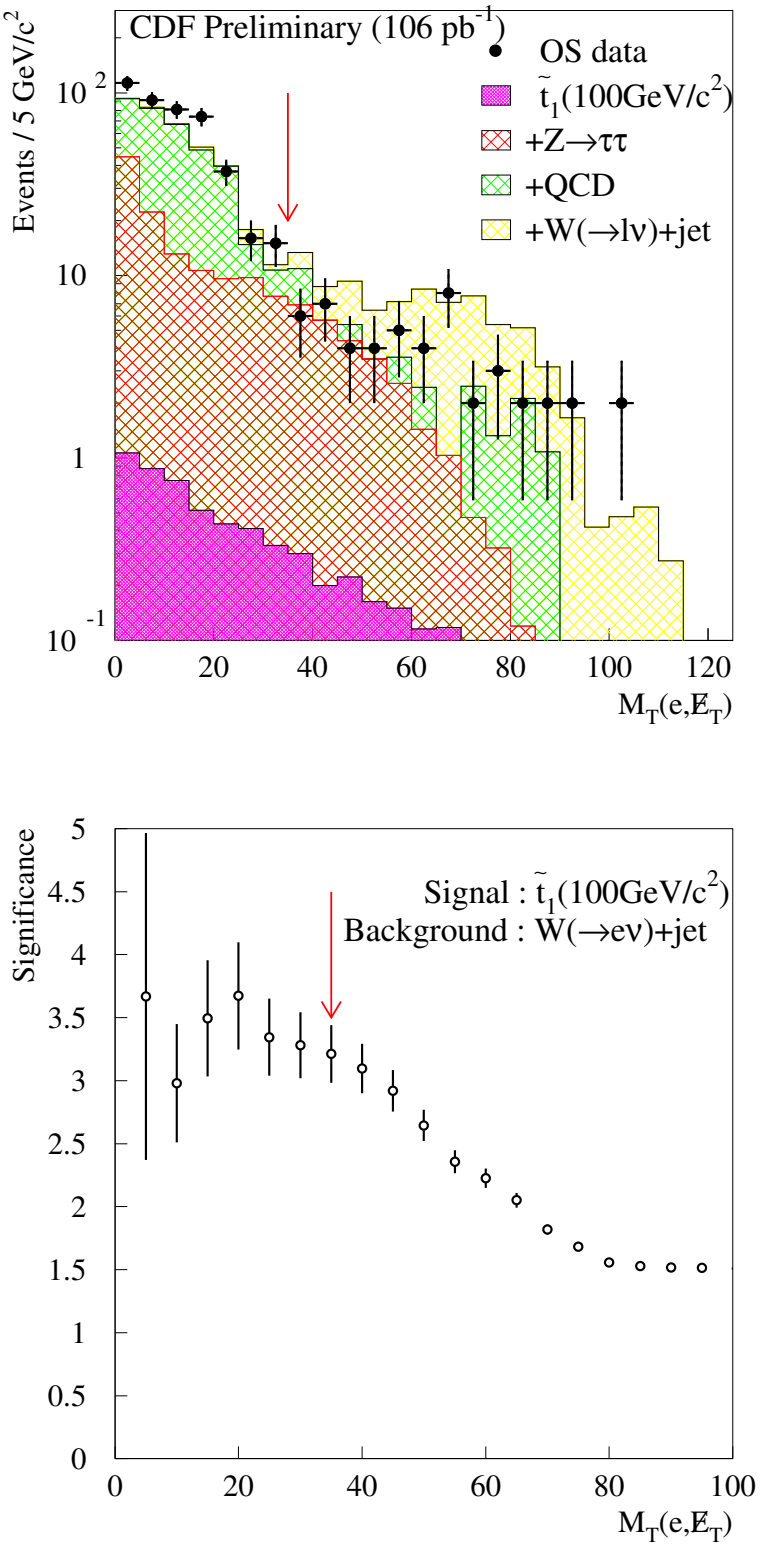

Figure 3.6: Distributions of $M_T(e, \not\!\!E_T)$ (top), and significance (bottom)

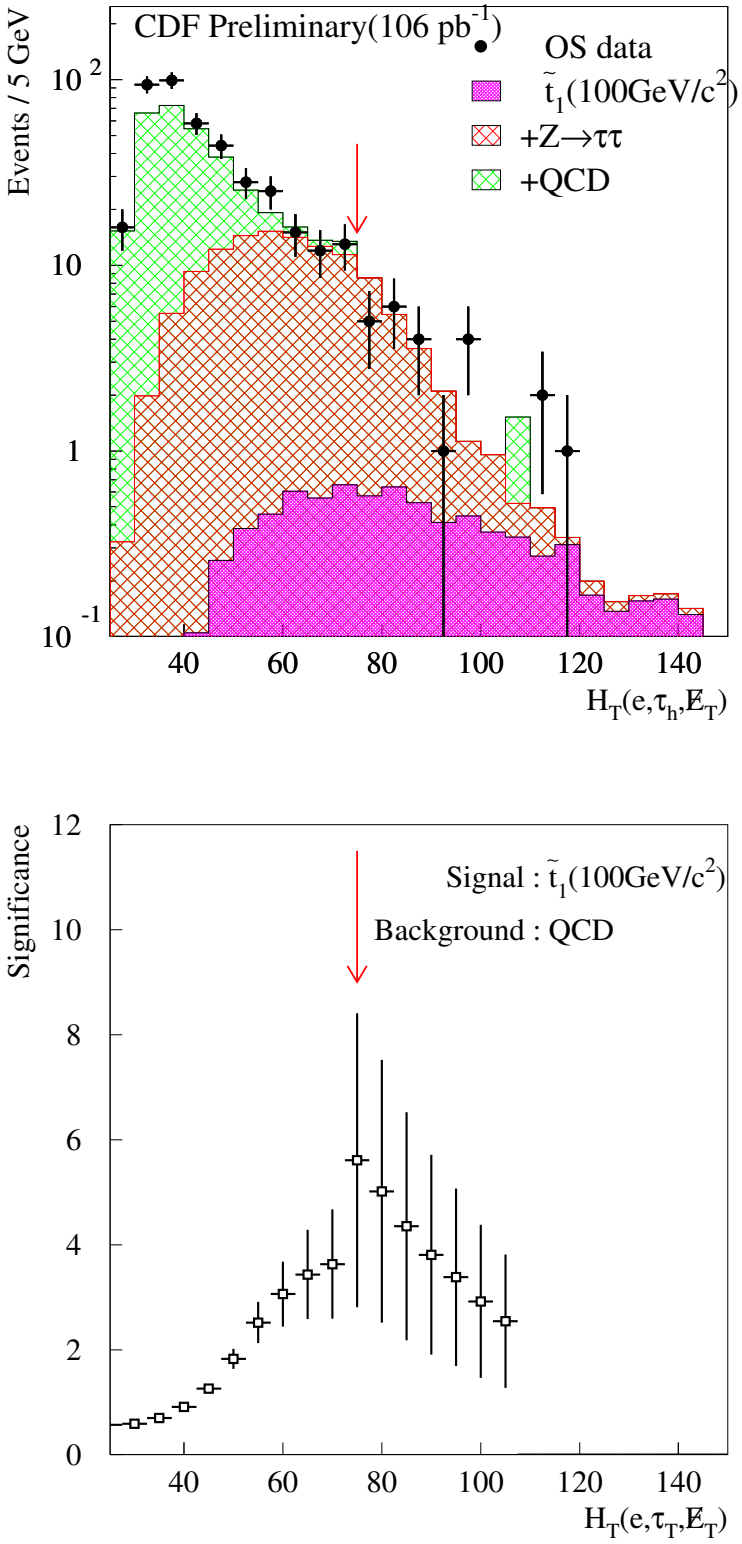

Figure 3.7: Distributions of $H_T(e, \not\!\!E_T)$ (top) and significance (bottom)

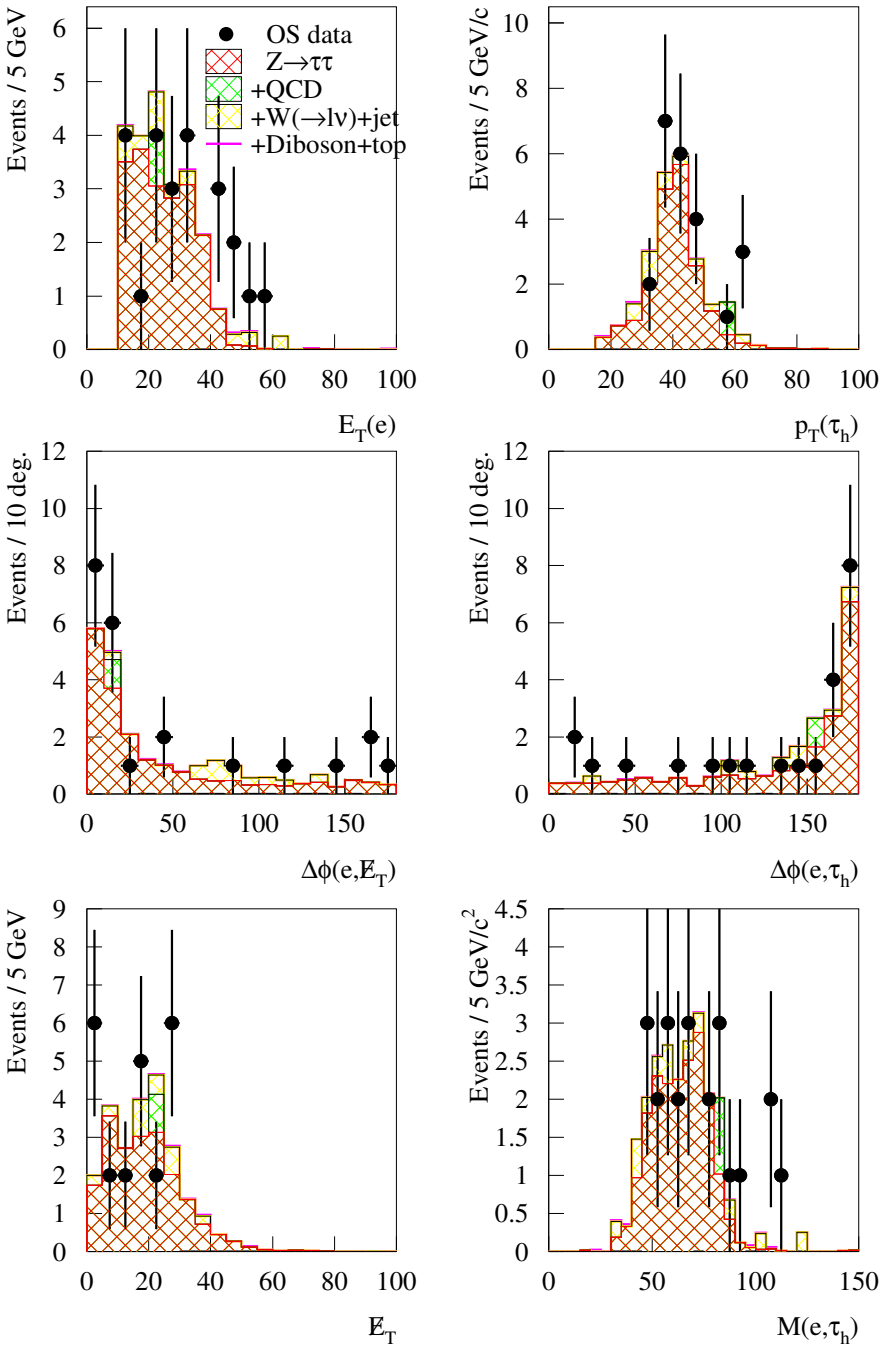

Figure 3.8: Distributions of $E_T(e)$, $p_T(\tau_h)$, $\Delta\phi(e,\tau_h)$, $\Delta\phi(e,\not\!\!E_T)$, $\not\!\!E_T$ and $M(e,\tau_h)$, for data and expectation of opposite-sign events after $\tilde{t}_1\bar{\tilde{t}}_1$ selection cuts before jet requirement.

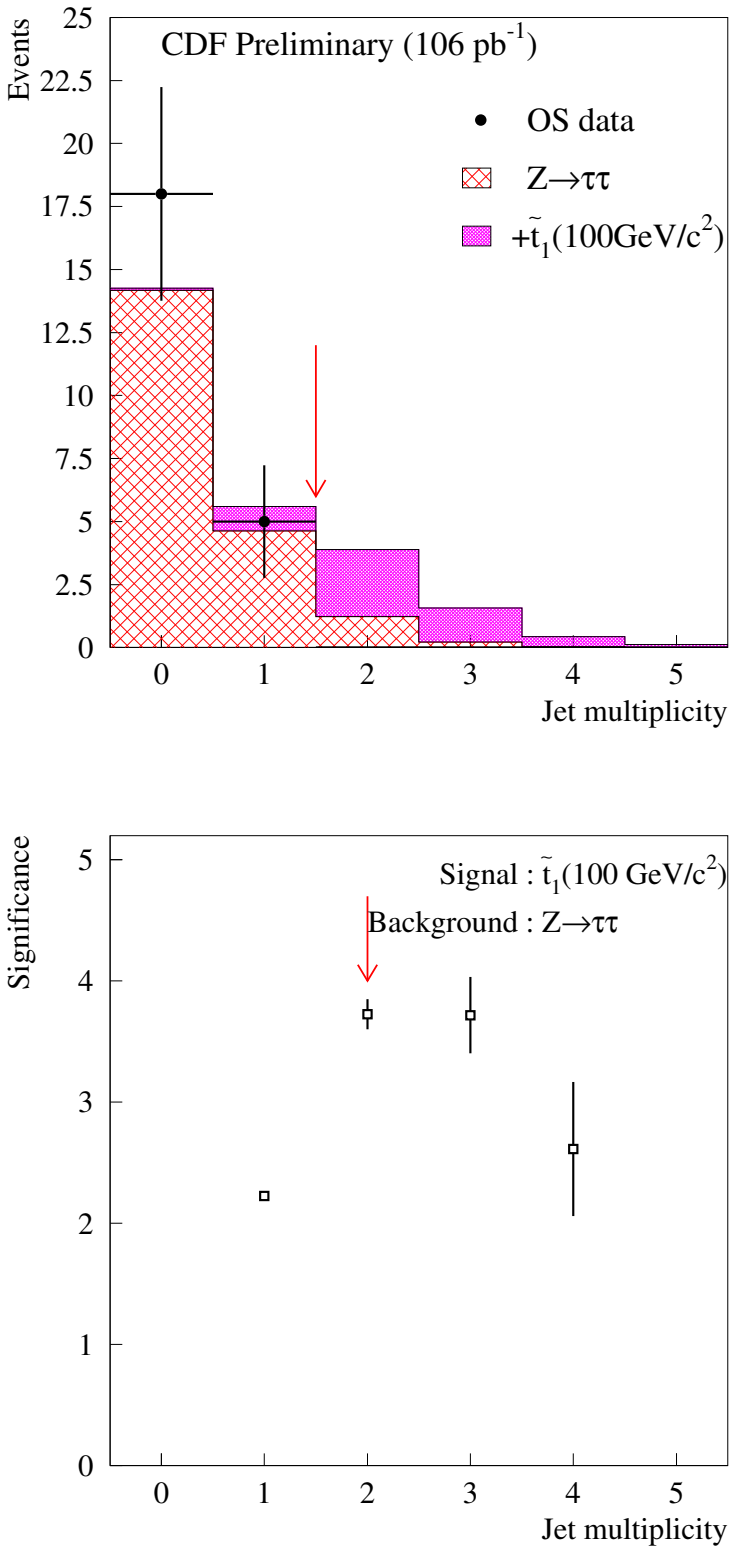

Figure 3.9: Distributions of the number of jets (top) and significance (bottom)

$\tau^+ b\tau^- \overline{b} \to e\tau_h b\overline{b} + X$ events in the $\tilde{t}_1$ mass range from 70 to 130 GeV/c^2 for each cut. Figure 3.10 shows the plot for the cut efficiency for $\tilde{t}_1\bar{\tilde{t}}_1$ events in a function of $\tilde{t}_1$ mass.

Table 3.11 shows the number of events in the data and MC for $Z^0 \to \tau\tau$ and $W(\to e\nu)$ + jets for each cut. Table 3.12 shows the number of events in the data and MC for $Z^0 \to \tau\tau$ and W + jets after the 0-jet selection. No data event is remained after the stop selection, while the number of expected backgrounds is 1.92 ± 0.11 (stat) ± 0.15 (sys). The dominant source of the expected background results from $Z^0 \to \tau\tau$ events. In Table 3.12, the expected number of $Z^0(\to \tau\tau)$ and $W(\to e\nu$ or $\tau\nu)$ + jets events is calculated with a use of VECBOS and HERWIG.

While no events is remained after the stop selection, the expected number of background is 1.92 ± 0.11 (stat) ± 0.15 (sys). For the MC tool verification, we recalculate the $Z^0 \to \tau\tau$ events using ISAJET. The number of opposite-sign, like-sign, and (opposite-sign−like-sign) events in the $Z^0 \to \tau\tau$ samples are estimated to be 1.64 ± 0.10 (stat), 0.05 ± 0.03 (stat), and 1.59 ± 0.10 (stat), respectively. Figure 3.11 shows the inclusive jets distribution in $e + \tau_h$ candidate after $Z^0 \to \tau\tau + 0$ jet selection compared background estimation. The background estimation for $Z^0 \to \tau\tau$ process is obtained by VECBOS + HERWIG shown in the top of Figure 3.11, while the background estimation for $Z^0 \to \tau\tau$ process is also obtained by ISAJET in the bottom of the figure. The width of each background in Figure 3.11 means statistical uncertainties from MC samples and like-sign data for QCD process. The estimation of $Z^0 \to \tau\tau$ using VECBOS + HERWIG is consistent very well with the case of using ISAJET usage.

Crosscheck for validation

Discussed above, no candidate events pass through the stop selection criteria, while the expected number of background from the SM is 1.92 ± 0.11 (stat) ± 0.15 (sys). For the selection procedure, we crosscheck the background by different sequence of stop selection criteria from previously used. In order to investigate the $e\tau_h + \geq 2$ jet events, we select two or more jet, later applied e and τ_h selection. The opposite- and like-sign data after $e\tau_h + \geq 2$ jet are obtained 11 and 8, respectively. Next, we apply $M_T(e, \not\!\!E_T)$ and $H_T(e, \tau_h, \not\!\!E_T)$ cuts defined above to this samples. A comparison of the opposite-sign

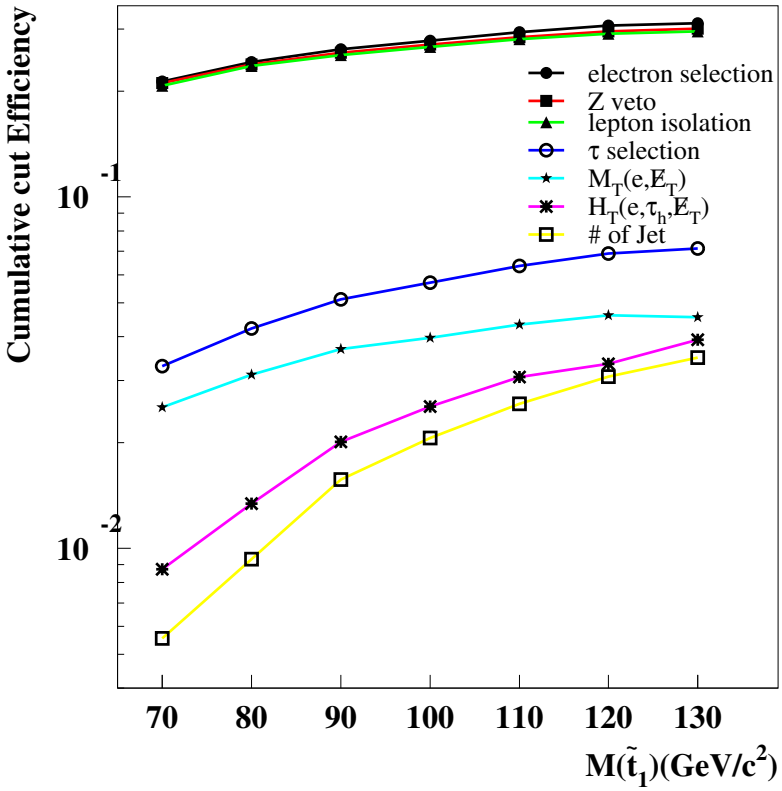

Figure 3.10: The cut efficiency for $\tilde{t}_1\bar{\tilde{t}}_1 \to \tau^+ b\tau\bar{b} \to (\ell\nu\nu b)(\tau_h\nu\bar{b})$

$e\tau_h+ \geq 2$ jet data and background estimation inside and outside the signal region is shown in Figure 3.12 along with the $M_T(e, \not\!\!E_T)$ and $H_T(e, \tau_h, \not\!\!E_T)$ cuts. The arrows show the final event selection requirements. The distribution would be changed as the dash line if the stop mass of 100 GeV/c^2 is found. The kinematic variable distributions in $e\tau_h+ \geq 2$ jet events are agreement with data and the background estimation overall. A breakdown of the backgrounds and data gained by the procedure mentioned above is given in Table3.13. By using the different selection procedure, we conclude that there could be found no discrepancy in the both procedure and the background expectation from MC is good agreement with data.

Table 3.10: Event selection efficiencies and trigger efficiencies (%) for $\tilde{t}_1\bar{\tilde{t}}_1 \to \tau^+ b\tau^- \overline{b} \to e\tau_h b\overline{b} + X$ events from 70 to 130 GeV/c^2 with each cuts.

Cut efficiency (%)							
$M(\tilde{t}_1)$ (GeV/c^2)	70	80	90	100	110	120	130
e selection	21.3	24.2	26.3	27.8	29.4	30.7	31.2
Z^0 veto	98.9	98.3	97.8	97.4	96.9	96.6	95.8
Isolation	98.2	98.3	98.1	98.4	98.4	98.2	98.4
τ_h selection	15.7	17.9	20.0	21.2	22.5	23.5	23.9
$M_T(e, \not\!\!E_T)$	77.3	74.6	72.9	70.2	68.7	67.1	64.3
$H_T(e, \tau_h, \not\!\!E_T)$	34.6	43.0	54.5	63.7	70.9	77.3	86.2
N_{jet}	63.6	69.5	78.0	81.3	84.0	86.5	88.9
Total	0.554	0.932	1.57	2.06	2.58	3.08	3.49
Trigger efficiency	77.1	77.5	77.6	78.1	78.1	78.5	78.5

Table 3.11: Number of events in data and MC samples after each cut

[$e + \tau_h$]	$Z^0(\rightarrow \tau\tau)$		$W(\rightarrow e\nu)$+jets		Data	
Cut	OS	LS	OS	LS	OS	LS
Baseline	138.5	0.7	65.3	19.7	479	251
$M_T(e, \not\!\!E_T)$ cut	113.4	0.6	6.0	2.0	427	238
$H_T(e, \tau_h, \not\!\!E_T)$ cut	19.3	0.1	2.3	0.7	23	1
N_{jet}	1.65	0.00	0.12	0.03	0	0

Table 3.12: Summary of yields of $e + \tau_h$ pairs in the data and MC events after $\tilde{t}_1\bar{\tilde{t}}_1$ selection cut.

Process	OS	LS	OS−LS
$Z^0 \rightarrow \tau\tau$	1.65	0.00	1.65 ± 0.09(stat) ± 0.14(sys)
$\gamma \rightarrow \tau\tau$	0.01	0.00	0.01 ± 0.01 ± 0.01
$W(\rightarrow e\nu)$+jets	0.12	0.03	0.09 ± 0.04 ± 0.01
$W(\rightarrow \tau\nu)$+jets	0.02	0.00	0.02 ± 0.02 ± 0.01
Diboson	0.06	0.01	0.05 ± 0.01 ± 0.02
Top	0.10	0.00	0.10 ± 0.03 ± 0.03
QCD(LS data)	N/A	0	0
Total	1.96	0.04	1.92 ± 0.11 ± 0.15

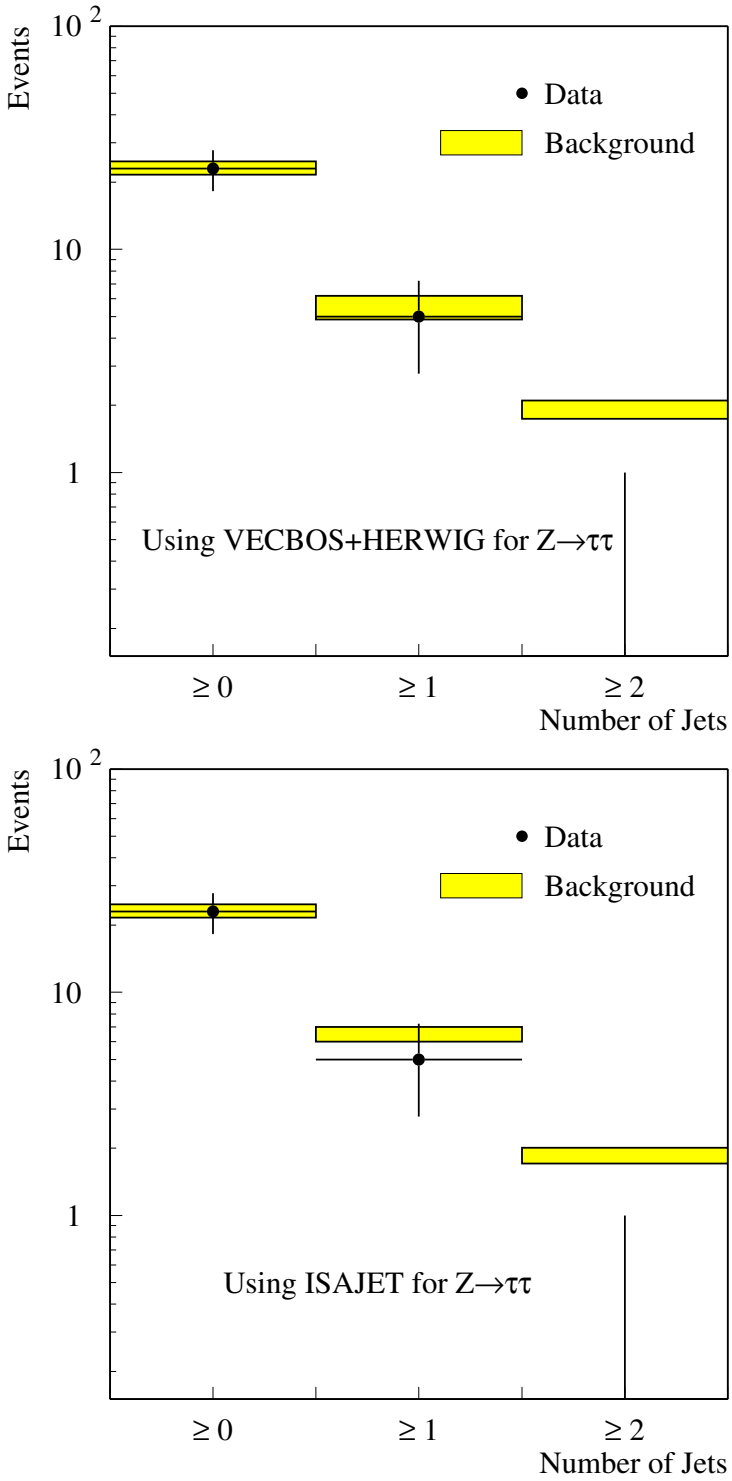

Figure 3.11: Inclusive jet distribution in $e + \tau_h$ event after $\tilde{t}_1\bar{\tilde{t}}_1$ selection cuts before jet requirement.

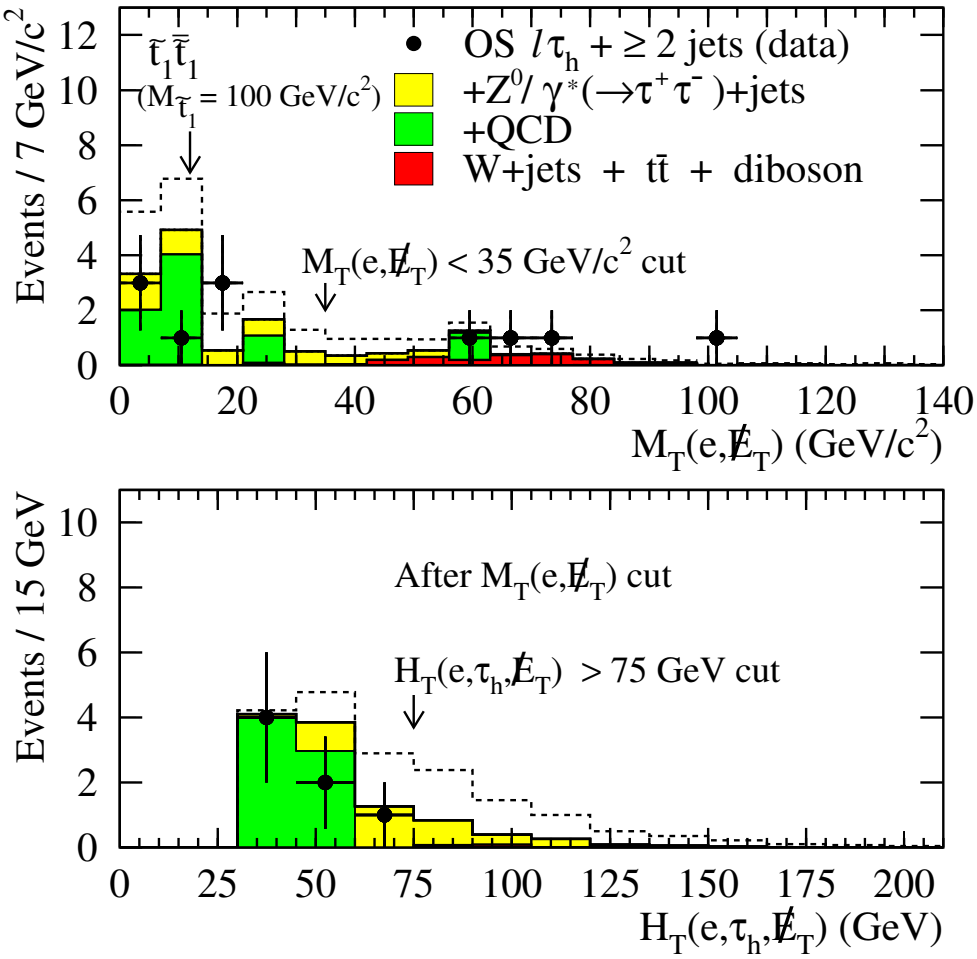

Figure 3.12: The data selection criteria for the opposite-sign $e\tau_h+ \geq 2$ jets sample

Cut criteria		$e\tau_h$ selection	≥ 2 jet	$M_T(e, \not\!\!E_T)$	$H_T(e, \tau_h, \not\!\!E_T)$
Z^0/γ^*+jets	OS	$140.1 \pm 0.9 \pm 7.2$	$4.9 \pm 0.1 \pm 0.4$	$4.0 \pm 0.1 \pm 0.3$	$1.7 \pm 0.1 \pm 0.2$
	LS	$0.7 \pm 0.1 \pm 0.1$	$0.0 \pm 0.0 \pm 0.0$	$0.0 \pm 0.0 \pm 0.0$	$0.0 \pm 0.0 \pm 0.0$
W+jet	OS	$76.6 \pm 3.4 \pm 4.4$	$2.7 \pm 0.2 \pm 0.2$	$0.3 \pm 0.1 \pm 0.1$	$0.1 \pm 0.1 \pm 0.1$
	LS	$22.3 \pm 1.9 \pm 1.4$	$1.2 \pm 0.3 \pm 0.1$	$0.3 \pm 0.1 \pm 0.1$	$0.0 \pm 0.0 \pm 0.0$
Diboson	OS	$1.55 \pm 0.07 \pm 0.65$	$0.22 \pm 0.02 \pm 0.09$	$0.11 \pm 0.01 \pm 0.05$	$0.06 \pm 0.01 \pm 0.02$
	LS	$0.34 \pm 0.04 \pm 0.13$	$0.12 \pm 0.02 \pm 0.05$	$0.05 \pm 0.01 \pm 0.02$	$0.01 \pm 0.01 \pm 0.01$
Top	OS	$0.73 \pm 0.09 \pm 0.19$	$0.60 \pm 0.07 \pm 0.16$	$0.10 \pm 0.03 \pm 0.03$	$0.10 \pm 0.03 \pm 0.03$
	LS	$0.10 \pm 0.04 \pm 0.13$	$0.09 \pm 0.03 \pm 0.02$	$0.00 \pm 0.00 \pm 0.00$	$0.00 \pm 0.00 \pm 0.00$
QCD	N/A	251	8	7	0
OS expectation		$447.3 \pm 16.3 \pm 8.6$	$15.0 \pm 2.9 \pm 0.5$	$11.2 \pm 2.6 \pm 0.3$	$1.9 \pm 0.1 \pm 0.2$
OS Data		479	11	7	0

Table 3.13: A breakdown of the backgrounds and data as a function of event reduction requirement

.

Chapter 4

Systematic Uncertainties

We experimentally measure the scalar top-quark pair production cross section ($\sigma_{\tilde{t}_1\bar{\tilde{t}}_1}$) and the branching ratio (B($\tilde{t}_1 \to \tau^+ b$)) as follows:

$$\begin{aligned} \sigma_{\tilde{t}_1\bar{\tilde{t}}_1} \cdot B(\tilde{t}_1 \to \tau^+ b)^2 &= \frac{N^{can}_{\tilde{t}_1\bar{\tilde{t}}_1} - N^{BG}_{\tilde{t}_1\bar{\tilde{t}}_1}}{A_{\tilde{t}_1\bar{\tilde{t}}_1} \int \mathcal{L}\, dt} \\ &= \left(\frac{N^{can}_{\tilde{t}_1\bar{\tilde{t}}_1} - N^{BG}_{\tilde{t}_1\bar{\tilde{t}}_1}}{N^{can}_Z - N^{BG}_Z}\right) \left(\frac{A^{MC}_Z \cdot \varepsilon^{trg}_Z}{A^{MC}_{\tilde{t}_1\bar{\tilde{t}}_1} \cdot \varepsilon^{trg}_{\tilde{t}_1\bar{\tilde{t}}_1}}\right) \cdot \sigma_{Z^0} \cdot B(Z^0 \to \tau\tau) \cdot R(\text{0-jet}) \end{aligned} \tag{4.1}$$

The systematic uncertainty on the expected number of stop events comes from the statistical uncertainties in the number of the $Z^0 \to \tau\tau$ events ($N^{can}_Z - N^{BG}_Z$), the event acceptance from the $Z^0 \to \tau\tau$ (A^{MC}_Z) and the $\tilde{t}_1\bar{\tilde{t}}_1$ events ($A^{MC}_{\tilde{t}_1\bar{\tilde{t}}_1}$) and the trigger efficiency ratio ($R_{trig} \equiv \epsilon_Z/\epsilon_{stop}$) as well as the uncertainty of the the CDF measurement of $\sigma_{Z^0} \cdot B(Z^0 \to \tau\tau)$ and R(0-jet). The evaluations of the systematic uncertainties are described below.

4.1 Canceled and Reduced Terms of Systematic Uncertainties

4.1.1 Canceled Term of Systematic Uncertainties

Mentioned in Section 3.1, some parameters are canceled by normalizing to the $Z^0 \to \tau\tau$ events. They are the luminosity, the z-vertex efficiency, and the τ decay branching ratio. Therefore, the systematic uncertainty from these terms does not affected in our analysis. It should be noted that the uncertainty arising from the luminosity is included in the uncertainties of the Z^0 production cross section described later. Next, the systematic uncertainties of identification and isolation cut from electron and τ_h are reduced.

4.1.2 Systematic uncertainty of Trigger Efficiency

The trigger efficiency in electron detection is calculated with a use of the MC simulation events, depending on the transverse energy and momentum for electrons. The systematic uncertainty of the trigger efficiency is taken as the maximum difference in the ratio of trigger efficiency of $Z^0 \to \tau\tau$ to that of $\tilde{t}_1\bar{\tilde{t}}_1$ event ($\varepsilon^{trg}_{\tilde{t}_1\bar{\tilde{t}}_1}/\varepsilon^{trg}_{Z}$) by varying the parameterized curves by one standard deviation for the L1, L2 and L3 triggers.

4.2 Systematic Uncertainties for $Z^0(\to \tau\tau)$ Events

4.2.1 $Z^0(\to \tau\tau)$ Events Candidates Statistics

We use the statistical uncertainty of the $Z^0(\to \tau\tau)$ events candidates subtracted by the background using the data and MC, $N_Z^{can} - N_Z^{BG}$. The statistical uncertainty of the $Z^0(\to \tau\tau)$ events candidates is obtained to be 17.1 %.

4.2.2 Cross Section of $Z^0(\to \tau\tau)+ \geq n$ Jets Events

We use the cross section of $Z^0(\to \tau\tau)$, $\sigma_{Z^0} \cdot B(Z^0 \to \tau\tau)$ as that of $Z^0(\to ee)$ assuming the lepton universality. Therefore we employ the uncertainty caused by the error of the

cross section of $Z^0 \to ee$ [45]. As described in Subsection 3.4.1, we employ the jet-veto in $Z^0 \to \tau\tau$ analysis. The ratio of jet-veto events to the total R(0-jet) is obtained from the analysis of $Z^0(\to ee) + \geq n$ jets because of the similar reason described above. Therefore, we employ the systematic uncertainty of R(0-jet) from the study of $Z^0(\to ee) + \geq n$ jets [42].

4.2.3 Parton Distribution

The choice of the PDFs affects the total cross section, the relative contributions of the gg and $q\overline{q}$ subprocesses. Our standard choice of the PDFs used in all MC simulations is CTEQ4L [28]. The systematic uncertainty due to the different PDFs is estimated by comparing the acceptance of $Z^0 \to \tau\tau$ events with that for other structure functions. Here we use MRSG[43] and GRV94LO[44].

4.2.4 Statistical Uncertainty in the MC Samples

The acceptance using the MC simulation is calculated as $A^{MC} = N^{pass}/N^{gen}$, where the N^{gen} and N^{pass} are the number of generated events and satisfying all cuts, respectively. The statistical uncertainty in the acceptance ΔA^{MC} is

$$\Delta A^{MC} = \sqrt{\frac{A^{MC}(1 - A^{MC})}{N^{gen}}} \tag{4.2}$$

We estimate the statistical uncertainties of the A^{MC} by the MC.

4.3 Systematic Uncertainties for $\tilde{t}_1\bar{\tilde{t}}_1$ Events

The dominant uncertainty is caused by the variation in the $\tilde{t}_1$ acceptance from choices of the QCD renormalization scale Q^2, PDFs, amount of gluon radiation, the jet energy scale and the statistical uncertainty in the MC samples. We estimate the uncertainty from the parton distributions and the statistical uncertainties in the MC samples using the same method as that of $Z^0 \to \tau\tau$ mentioned in Section 4.2. In this section, the rest uncertainties of stop events are described as belows.

4.3.1 Gluon Radiation

We use `$ISAJET_LIBRARY/source/decjet.f` for excluding jets generated by the final gluon radiation via the parton shower fragmentation. We determine the effect due to the gluon radiation on the acceptance by taking the difference between with the final gluon radiation "on" and with the final gluon radiation "off". Furthermore, assuming the magnitude of the effect for the initial gluon radiation is same as final one, the total magnitude of the effect for the gluon radiation is calculated in quadrature from the initial and final gluon radiation.

4.3.2 Q^2 Dependence

The value for Q^2 is affected by the QCD renormalization. The nominal Q_0^2 in the two body process in ISAJET is defined as

$$Q_0^2 = \max\left(\frac{2\hat{s}\hat{t}\hat{u}}{\hat{s}^2+\hat{t}^2+\hat{u}^2}, 4M_{\tilde{t}}^2\right)$$

where $M_{\tilde{t}}$ is scalar top quark's mass. We calculate the acceptance with two Q^2 values cases of $4\,Q_0^2$ and $0.25\,Q_0^2$. The uncertainty is taken as the maximum acceptance difference between the two case values obtained just above and the nominal one.

4.3.3 Jet Energy Scale

Uncertainties in the calorimeter energy scale propagate to the uncertainties in the acceptance. We vary absolute and relative energy scale by 5% using JTC96X option to determine the effect on the acceptance. We take this uncertainty as the maximum difference of acceptance from the nominal acceptance.

4.4 Summary of Systematic Uncertainties

Table 4.1 shows the systematic uncertainty for the ratio of trigger efficiency of $Z^0 \to \tau\tau$ to that of $\tilde{t}_1\bar{\tilde{t}}_1$ events. Table 4.2 and 4.3 show the systematic uncertainties for $Z^0 \to \tau\tau$ and $\tilde{t}_1\bar{\tilde{t}}_1$ events, respectively. The dominant systematic uncertainties in our analysis

is the statistical uncertainties from the $Z^0 \rightarrow \tau\tau$ candidates (17.1%), and the other uncertainties are less than 10%. The combined systematic uncertainty is calculated by adding all uncertainties in quadrature. Table 4.4 shows the total systematic uncertainties from 70 to 130 GeV of the scalar top quark mass.

Table 4.1: Systematic uncertainties for trigger efficiency from 70 to 130 GeV/c^2 .

Systematic uncertainties for trigger efficiency (%)							
$m_{\tilde{t}_1}$ (GeV/c^2)	70	80	90	100	110	120	130
Trigger efficiency	1.2	1.1	0.7	0.6	0.6	0.4	0.4

Table 4.2: Systematic uncertainties from $Z^0 \to \tau\tau$ events.

Uncertainties from $Z^0 \to \tau\tau$ (%)	
Data Stat.	17.1
Parton Distribution	4.1
MC stat.	1.4
$\sigma_{Z^0} \cdot B(Z^0 \to \tau\tau)$	5.2
R(0-jet)	3.1
Total	18.7

Table 4.3: Systematic uncertainties for the $\tilde{t}_1\bar{\tilde{t}}_1 \to b\tau^+\overline{b}\tau^- \to e\tau_h b\overline{b} + X$ events from 70 to 130 GeV/c^2 .

Systematic uncertainties for $\tilde{t}_1\bar{\tilde{t}}_1$ events							(%)
$M(\tilde{t}_1)$ (GeV/c^2)	70	80	90	100	110	120	130
Gluon Radiation	4.8	5.1	5.1	4.2	3.4	3.4	3.5
Q^2 dependence	8.2	5.2	4.8	4.2	3.4	3.3	2.7
Parton Distribution	4.6	4.7	4.5	3.9	2.5	1.7	2.0
Jet Energy Scale	3.2	3.9	2.8	1.7	1.4	1.2	1.2
MC stat.	4.7	2.9	2.4	2.0	1.9	1.6	1.7
Total	12.0	9.9	9.1	7.6	5.9	5.4	5.3

Table 4.4: Total systematic uncertainties for from 70 to 130 GeV/c^2 .

Total systematic uncertainties							(%)
$m_{\tilde{t}_1}$ (GeV/c^2)	70	80	90	100	110	120	130
Trigger efficiency	22.3	21.2	20.8	20.2	19.6	19.5	19.4

Chapter 5

Results and Disscusion

We obtain zero events after our stop selection cuts in RUN I data, while the number of expected SM events was 1.92 ± 0.18 (stat+sys) We can't see the excess of stop events compared with the background expectation. In this chapter, we describe how to calculate the upper limit of signal events number, the result of a cross section and a mass limits at the 95 % confidence level (C.L.).

5.1 Calculation of the Limit

In new particle searches, we usually use two methods of the calculation of the upper limit of signal events [47]. One is based on a frequentist method and the other is a bayesian one. In our analysis, we employ a frequentist method, so we describe only a frequentist methods, below.

Given the integer number of observed event (n_0) and the number of expected events (μ), the Poisson probability for observing n_0 is written as

$$P(n_0;\mu) = \frac{\mu^{n_0} e^{-\mu}}{n_0!} \tag{5.1}$$

In new particle searches, we have to determine the μ. The upper limit N on the number of expected events is defined as a value μ by some probability ϵ is defined whether to observed n_0 events or fewer events. The confidence level (C.L.) of the upper limit is

then simply $1-\epsilon$, where ϵ is the sum over the Poisson probabilities:

$$\epsilon = \sum_{n=0}^{n_0} P(n;\mu) \tag{5.2}$$

In practice, to obtain N, we vary μ until finding the value of ϵ corresponding to the desired C.L.. Therefore, N is the resulting value of μ.

If one expects an average of μ_B background events among the n_0 observed, and if one knows μ_B precisely, then the method can be extended to calculating a Poisson upper limit N on the number of signal events appeared in the observation. The value of N represents that value of μ_S, the mean number of signal expected, for which the probability is $1-\epsilon$ that in a random experiment one would observe more than n_0 events and have $n_B \leq n_0$, where n_B is the number of background events appeared in the sample. This can be calculated as above by adjusting N as the relation

$$\epsilon = \frac{\sum_{n=0}^{n_0} P(n;\mu_B+N)}{\sum_{n=0}^{n_0} P(n;\mu_B)} \tag{5.3}$$

is satisfied. According to the PDG [48], this results is conservative upper limit in that for some true μ_S, the probability of obtaining $N > \mu_S$ exceeds in average $1-\epsilon$. This statement means no more than that if the true μ_S exceeds N, then there is a probability smaller than ϵ which one would observe more than n_0 events and have $n_B \leq n_0$. Also, if one obtains a value of n_0 significantly lower than μ_B, it is more conservative to assume $n_0 \approx n_B$ to obtain N.

Suppose that one knows the value of μ_B to within an overall (statistical and systematic) Gaussian uncertainties of σ_B, and the overall acceptance A with an overall uncertainty of σ_A. In this case the relative uncertainty on μ_S is σ_A/A. One can define the Poisson upper limit N on μ_S as before: that value of the true μ_S for which one would observe more than n_0 events and have $n_B \leq n_0$. In this case, however, one seeks that value of N such that

$$\epsilon = \frac{\sum_{n=0}^{n_0} \frac{1}{\sqrt{2\pi\sigma_N^2}} \int_0^\infty \int_0^\infty e^{-\frac{(\mu_B-\mu_B')^2}{2\sigma_B^2}} e^{-\frac{(\mu_S-\mu_S')^2}{2\sigma_S^2}} P(n;\mu_B'+\mu_S') d\mu_B' d\mu_S'}{\sum_{n=0}^{n_0} \int_0^\infty P(n;\mu_B) e^{-\frac{(\mu_B-\mu_B')^2}{2\sigma_B^2}} d\mu_B'} \tag{5.4}$$

where we take $\sigma_N = N\sigma_A/A$. In this way, one assumes *a priori* a Gaussian distribution of the true values of μ_S and μ_B about the values of obtained in subsidiary studies, with width given by the uncertainties obtained in those studies.

5.2 The Limit for Cross Section for Stop Pair Production

We calculate the number of stop event at the 95% C.L. ($N^{95\%CL}_{\tilde{t}_1\bar{\tilde{t}}_1}$) using Eq. (5.4). For calculating $N^{95\%CL}_{\tilde{t}_1\bar{\tilde{t}}_1}$, we use zero event for observed events after stop selection, 1.92 $\pm$ 0.11(stat) $\pm$ 0.15(sys) for the number of background and the systematic uncertainties listed in Table 4.1, 4.2 and 4.3. Finally, we obtained the 95% C.L. upper limits on the cross section for $\tilde{t}_1\bar{\tilde{t}}_1 \rightarrow \tau^+ b\tau^- \overline{b}$ events from $p\bar{p}$ collisions at $\sqrt{s}$ = 1.8 TeV using $N^{95\%CL}_{\tilde{t}_1\bar{\tilde{t}}_1}$. The formula for calculating the 95% C.L. upper limits on the cross section for $\tilde{t}_1\bar{\tilde{t}}_1 \rightarrow \tau^+ b\tau^- \overline{b}$ events are written as

$$\begin{aligned}
\sigma_{\tilde{t}_1\bar{\tilde{t}}_1} \cdot B(\tilde{t}_1 \rightarrow \tau^+ b)^2 &= \frac{N^{95\%C.L.}_{\tilde{t}_1\bar{\tilde{t}}_1}}{A_{\tilde{t}_1\bar{\tilde{t}}_1} \int \mathcal{L}\, dt} \\
&= \left(\frac{N^{95\%C.L.}_{\tilde{t}_1\bar{\tilde{t}}_1}}{N_Z^{can} - N_Z^{BG}} \right) \left(\frac{A_Z^{MC} \cdot \varepsilon_Z^{trg}}{A^{MC}_{\tilde{t}_1\bar{\tilde{t}}_1} \cdot \varepsilon^{trg}_{\tilde{t}_1\bar{\tilde{t}}_1}} \right) \cdot \sigma_{Z^0} \cdot B(Z^0 \rightarrow \tau\tau) \cdot R(\text{0-jet})
\end{aligned} \tag{5.5}$$

The results are shown in Table 5.1 and Figure 5.1 for the stop masses from 70 to 130 GeV/c^2. We have set a 95% C.L. lower limit of the stop mass to be 111 GeV/c^2 for $B(\tilde{t}_1 \rightarrow \tau^+ b) = 100\%$ by comparing with the NLO theoretical calculation via PROSPINO [9] with CTEQ4M.

5.3 Discussion

While we assume the branching ratio of $\tilde{t}_1 \rightarrow \tau^+ b$ is 100% in above issue, we can calculate the the branching ratio limit $B^{95\%CL}(\tilde{t}_1 \rightarrow \tau^+ b)$ using Eq. 5.5. The $B^{95\%CL}(\tilde{t}_1 \rightarrow \tau^+ b)$

can be calculated as follows

$$B^{95\%CL}(\tilde{t}_1 \to \tau^+ b) = \sqrt{\frac{\sigma^{95\%CL}_{\tilde{t}_1\bar{\tilde{t}}_1}}{\sigma^{th}_{\tilde{t}_1\bar{\tilde{t}}_1}}} \tag{5.6}$$

where $\sigma^{95\%CL}_{\tilde{t}_1\bar{\tilde{t}}_1}$ and $\sigma^{th}_{\tilde{t}_1\bar{\tilde{t}}_1}$ are the $\tilde{t}_1\bar{\tilde{t}}_1$ cross section at 95% C.L. limit from RUN I data and from theory, respectively. Table 5.2 shows the branching ratio limit $B^{95\%CL}(\tilde{t}_1 \to \tau^+ b)$.

No events passed after our stop selection cuts in RUN I data, while the number of expected SM events was 1.92 ± 0.18 (stat+sys). The number of observation is less than the background, and this probability of the $N_{can} = 1$ events is 14.7% assuming Possion probability. To make sure, we evaluate 95% C.L. upper limits on the cross section assuming the number of observed events in the data (N_{can}) were one or two. We assume all others, such as the events acceptance and its systematic uncertainty, to be unchanged. The probabilities of the N_{can} events, $P(N_{can}; \mu = 1.92)$, are 14.7% 28.1% and 27.0% for N_{can} = zero, one and two events, respectively. The results are shown in Table 5.3 and Figure 5.2. Assuming N_{can} to be one or two events, a 95% lower limits of stop mass are 103 GeV/c^2 and 95 GeV/c^2 respectively. From this discussion, we can exclude the much higher mass region than that by the LEP experiment if we would obtain one event after stop selection.

Since our analysis does not distinguish the quark flavors in jet reconstruction, the results are equally valid for any λ'_{33k} coupling, for which k is 1, 2 or 3 corresponding to $\tilde{t}_1 \to \tau^+ d$, $\tilde{t}_1 \to \tau^+ s$, or $\tilde{t}_1 \to \tau^+ b$, respectively. Therefore, we obtain the stringent higher mass limit than the current upper limit 95 GeV/c^2 by the LEP experiments.

Table 5.1: Table of the cross section upper limit for $\tilde{t}_1\bar{\tilde{t}}_1 \to b\tau^+\bar{b}\tau^- \to e\tau_h b\bar{b} + X$ events from 70 to 130 GeV/c^2

$\tilde{t}_1$ mass	$A^{MC}_{\tilde{t}_1\bar{\tilde{t}}_1}$ (%)	$\varepsilon^{trg}_{\tilde{t}_1\bar{\tilde{t}}_1}$ (%)	Total Uncertainty (%)	$N^{95\%CL}_{\tilde{t}_1\bar{\tilde{t}}_1}$	$\sigma^{95\%CL}_{\tilde{t}_1\bar{\tilde{t}}_1}$ (pb)
70	0.554	77.1	22.3	3.26	34.3
80	0.932	77.5	21.2	3.23	20.1
90	1.57	77.6	20.8	3.22	11.8
100	2.06	78.1	20.2	3.21	8.96
110	2.58	78.1	19.6	3.19	7.11
120	3.08	78.5	19.5	3.19	5.93
130	3.49	78.5	19.4	3.19	5.23

Table 5.2: Summary of upper limits of the branching ratio $B^{95\%CL}(\tilde{t}_1 \to \tau^+ b)$ for $\tilde{t}_1\bar{\tilde{t}}_1 \to b\tau^+\bar{b}\tau^- \to e\tau_h b\bar{b} + X$ events from 70 to 130 GeV/c^2

$\tilde{t}_1$ mass (GeV/c^2)	$\sigma^{th}_{\tilde{t}_1\bar{\tilde{t}}_1}$ (pb)	$\sigma^{95\%CL}_{\tilde{t}_1\bar{\tilde{t}}_1}$ (pb)	$B^{95\%CL}(\tilde{t}_1 \to \tau^+ b)$ (%)
70	86.5	39.4	63
80	42.8	20.1	69
90	22.5	11.8	72
100	12.6	8.96	84
110	7.33	7.11	97
120	4.45	5.93	100
130	2.80	5.23	100

Table 5.3: Summary of the cross section upper limit for $\tilde{t}_1\bar{\tilde{t}}_1 \rightarrow b\tau^+\overline{b}\tau^- \rightarrow e\tau_h b\overline{b} + X$ events from 70 to 130 GeV/c^2 in the case of the observed events number = 0, 1, 2

	$\sigma^{95\%CL}_{\tilde{t}_1\bar{\tilde{t}}_1}$ (pb)		
$\tilde{t}_1$ mass	$N_{can} = 0$	$N_{can} = 1$	$N_{can} = 2$
70	39.4	50.7	64.9
80	20.1	25.9	33.1
90	11.8	15.3	19.5
100	8.96	11.5	14.7
110	7.11	9.16	11.7
120	5.93	7.62	9.73
130	5.23	6.72	8.59

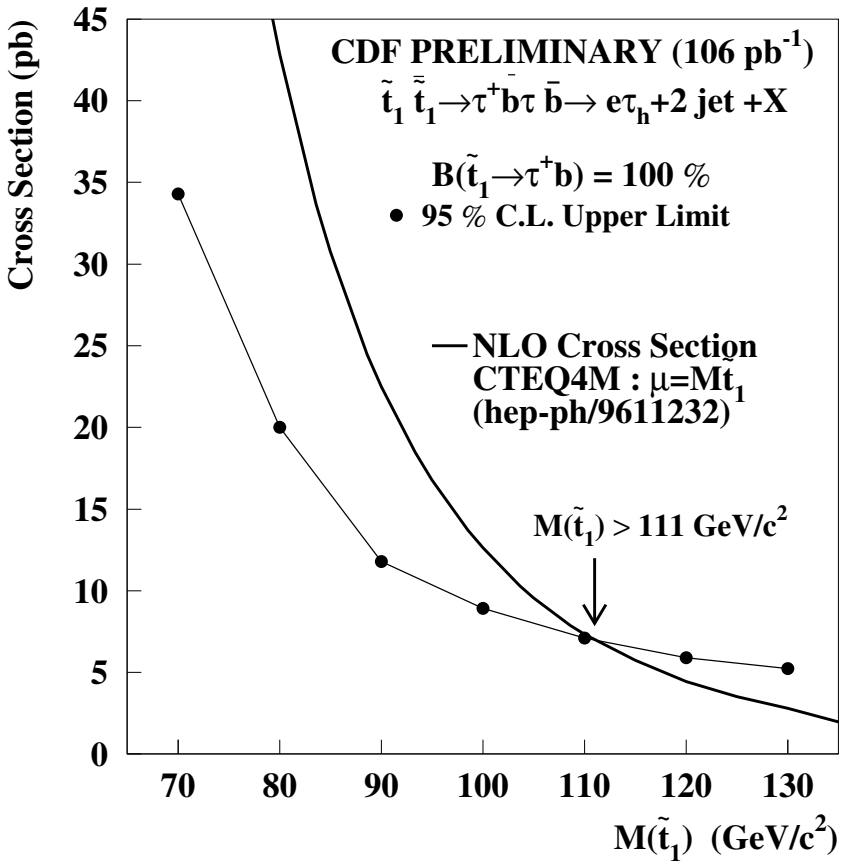

Figure 5.1: 95% confidence level on upper limit for cross section for $\tilde{t}_1\bar{\tilde{t}}_1 \to \tau^+ b\tau^- \overline{b}$ along with the theoretical calculation

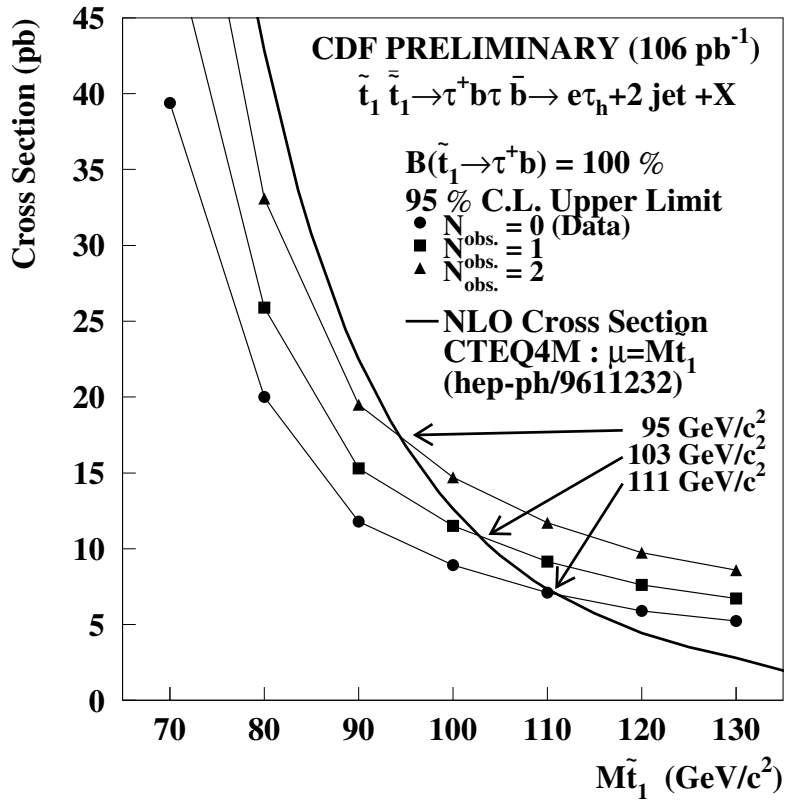

Figure 5.2: 95% confidence level on upper limit for cross section for $\tilde{t}_1\bar{\tilde{t}}_1 \to \tau^+ b\tau^- \overline{b}$ along with the theoretical calculation in the case of the observed events number = 0, 1, 2

Chapter 6

Conclusion

6.1 Conclusion

In conclusion, we have searched for the scalar top quark pair production ($\tilde{t}_1\bar{\tilde{t}}_1$) using 106 pb^{-1} data in $p\overline{p}$ collisions at $\sqrt{s} = 1.8$ TeV. The scalar top quark we are interested in could be potentially detected at the Tevatron, and becomes a good candidate of the supersymmetry. We have examined the $e + \tau_h + \geq$ 2-jet final state within a $\not{R}_p$ SUSY framework in which each $\tilde{t}_1$ decays to a τ lepton and a b quark via non-zero λ_{333} or ϵ_3 couplings. No $\tilde{t}_1\bar{\tilde{t}}_1$ event candidates is obtained, but we can set a 95% C.L. lower mass limit on the $\tilde{t}_1$ at 111 GeV/c^2 for $B(\tilde{t}_1 \to \tau^+ b) = 1$ and also a upper limit of the branching ratio by using the NLO theoretical calculation via PROSPINO [9] with CTEQ4M.

Bibliography

[1] S. L. Glashow, Nucl. Phys. **22**, 579 (1961); S. Weinberg, Phys. Rev. Lett. **19**, 1264 (1967); A. Salam, Elementary Particles Theory: Relativistic Groups and Analyticity (Nobel Symposium No. 8), edited by N. Svartholm (Almqvist and Wiksell, Stockholm, 1968), p. 367.

[2] E Witten, , Nucl. Phys. **B188**, 513 (1981); R.K. Kaul, Phys. Lett. **109B**, 19 (1982).

[3] D. V. Volkov and V. P. Akulov, Phys. Rev. Lett. **46B**, 109 (1973); J. Wess and B. Zumino, Nucl. Phys. **B70**, 39 (1974).

[4] For example Manuel Drees, "An Introduction to Supersymmetry", hep-ph/9611409; Keith A Olive, Stephen P. Martin, "A SUPERSYMMETRY PRIMER", hep-ph/97-0356; "Introduction to Supersymmetry: Astrophysical and Phenomenological Constraints", hep-ph/9911307.

[5] For reviews of the MSSM, see H. P. Nilles, Phys. Rep. **110**, 1 (1984); H. E. Haber and G. L. Kane, Phys. Rep. **117**, 75 (1985).

[6] H. Dreiner, "Introduction to Explicit R-parity Violation, hep-ph/9707435, Published in "Perspectives on supersymmetry: 462-479, " by G.L. Kane, World Scientific.

[7] Marco Aurelio Días, "The Minimal Supersymmetric Standard Model with a Bilinear R-Parity Violating Term," hep-ph/9711435 (1997), Proceedings of International Workshop On Quantum Effects In The Minimal Supersymmetric Standard Model.

[8] A. Bartl *et al.*, Phys. Lett. **B384**, 151 (1996); F. de Campos *et al.*, "R-parity Violating Decays of the Top-Quark and the Top-Squark at the Tevatron," hep-

ph/9903245 (1999), Published in the proceedings of Physics at Run II: Workshop on Supersymmetry / Higgs: Summary Meeting, Batavia, IL, 19-21 Nov 1998; W. Porod, D. Restrepo, and J.W.F. Valle, "Light Stop: MSSM Versus R-parity Violation," hep-ph/0001033 (2000).

[9] W. Beenakker *et al.*, "PROSPINO : A Program for the Production of Supersymmetric Particles in Next-to-Leading Order QCD" hep-ph/9611232 (1996).

[10] CDF Collaboration, T. Affolder *et al.*, Phys. Rev. Lett. **84**, 5273 (2000).

[11] CDF Collaboration, T. Affolder *et al.*, Phys. Rev. Lett. **84**, 5704 (2000).

[12] ALEPH collaboration, "Search for R-parity Violating Decays of Supersymmetric Particles in e^+e^- Collisions at Centre-of-Mass Energies from 189 GeV to 202 GeV," hep-ex/0011008 (2000), Submitted to Eur.Phys.J.C .

[13] CDF Collaboration, F. Abe *et al.*, Phys. Rev. Lett. **78**, 20-6 (1997).

[14] CDF Collaboration, F. Abe *et al.*, Nucl. Instrum. Methods Phys. Res. Sect. A **271**, 387 (1988); Phys. Rev. D **50**, 2966 (1994).

[15] M. Gallinaro and H. Grassmann, "Observation of $Z^0 \to \tau\tau$," CDF Note 2490 (1994).

[16] T. Baumann and J. Troconiz, "Third Generation Leptoquark Search with 110 pb^{-1}," CDF Note 3840 (1996).

[17] M. Gallinaro *et al.*, "Observation of Top Dileptons with Hadronically Decaying τ Leptons," CDF Note 3461 (1996).
See /cdf/offln/cdftest/development/top/taufnd.cdf for details of the τ ID cuts.

[18] M. Hohlmann *et al.*, "A Description of the Tau-Tagging Routine TAUFND," CDF Note 2953 (1995).

[19] J.P. Done *et al.*, "Study of Run-1B Lepton Identification Efficiencies for SUSY Searches," CDF Note 4218 (1997).

[20] J.P. Done *et al.*, "Study of Run-1B Lepton Isolation Efficiencies for SUSY Searches," CDF Note 4291 (1997).

[21] K. Byrum *et al.*, "The Level-2 Trigger Efficiency for 9 GeV Electrons in Run IA - Part II," CDF Note 3665 (1998).

[22] T. Kamon *et al.*, "Study of the Inclusive Lepton Trigger Efficiency for the Run IA SUSY Trilepton Analysis," CDF Note 2596 (1998).

[23] W. Taylor *et al.*, "Run 1B Level 2 CEM_8_CFT_7_5 and XCES Electron Trigger Efficiencies," CDF Note 4691 (1998).

[24] N.L. Bruner, "Level 3 Trigger Efficiencies for the Low p_T Inclusive Lepton Data Sets MULB and ECLB," CDF Note 4700 (1998).

[25] K. Byrum *et al.*, Nucl. Instrum. Methods Phys. Res. Sect. A **364**, 144 (1995);

[26] K. Byrum, "Luminosity for Run IB Inclusive Electron Binary Dataset," CDF Note 5001 (1999).

[27] Top Group, "Sample Selection for Run 1B Top Search," CDF Note 2966 (1995).

[28] H. L. Lai, J. Huston, S. Kuhlmann, F. Olness, J. Owens, D. Soper, W. K. Tung, and H. Weerts, "Improved parton distributions from global analysis of recent deep inelastic scattering and inclusive jet data", Phys. Rev. D **D55**, 1280 (1997).

[29] H. Baer, F.E. Paige, S.D. Protopopescu, and X. Tata, hep-ph/0001086. We use version 7.44.

[30] J.P. Done *et al.*, "ISAJET Monte Carlo Validation," CDF Note 4903 (1999).

[31] F.A. Berends, W.T. Giele, H. Kuijf, and B. Tausk, Nucl. Phys. B **357**, 32 (1991); W.T. Giele, E.W. Glover, and D.A. Kosower, Nucl. Phys. B **403**, 633 (1993).

[32] G. Marchesini and B. R. Webber, Nucl. Phys. B **310**, 461 (1988); G. Marchesini *et al.*, Comput. Phys. Commun. **67**, 465 (1992).

[33] D. Cronin-Hennerssy *et al.*, "Measurement of the $W^{\pm} \rightarrow e^{\pm}+$ n Jet Cross Section in 1.8 TeV $p\bar{p}$ Collisions," CDF Note 3070 (1996).

[34] C. Loomis, "Using TAUOLA, A Decay Library for Polarized τ Leptons," CDF Note 2796 (1994).

[35] J.D. Lewis and P. Avery, "CLEOMC: The CDF Interface to the CLEO Monte Carlo (QQ)," CDF Note 2724 (1994).

[36] CDF Collaboration, F. Abe *et al.*, Phys. Rev. D **76**, 3070 (1996).

[37] CDF Collaboration, F. Abe *et al.*, Phys. Rev. D **49**, 1 (1994).

[38] Top Group, "The New CDF Run 1 Combined t-tbar Production Cross Section," CDF Note 5043 (1999).

[39] CDF Collaboration, F. Abe *et al.*, Phys. Rev. Lett. **78**, 4536 (1997).

[40] J. Ohnemus, Phys. Rev. D **44**, 3477 (1991).

[41] J. Ohnemus and J. Owens, Phys. Rev. D **43**, 3626 (1991).

[42] D. Cronin-Hennerssy *et al.*, "Measurement of the $Z \rightarrow e^{+}e^{-}+$ n Jet Cross Section in 1.8 TeV $p\bar{p}$ Collisions, " CDF Note 3360 (1996).

[43] M. Glück, E. Reya, and A. Vogt, Z. Phys. C **69**, 433 (1995).

[44] A. D. Martin, R. G. Roberts, W. J. Stirling, Phys. Lett. B **387**, 419 (1996).

[45] CDF collaboration, F. Abe *et al.*, Phys. Rev. Lett. **76**, 3070 (1996).

[46] CDF Collaboration, F. Abe *et al.*, Phys. Rev. D **45**, 1448 (1992).

[47] G. Zech, Nucl. Instrum. Methods Phys. Res. Sect. A **277**, 608 (1989); T. Huber *et al.*, Phys. Rev. D **41**, 2709 (1990).

[48] C. Caso *et al.*, "Review of Particle Physics", Particle Data Group, Eur. Phys. J. **C3**, 781 (1998)

[49] John Conway *et al.*, "Upper Limits on Poisson Processes Incorporating Uncertainties in Acceptance and Background," CDF Note 4476 (1996).